PALEOINTENSITY DETERMINATIONS ON BASALTS FROM THE EMPEROR SEAMOUNTS AND TESTING THE PROPERTIES OF FORC DIAGRAMS USING MICROMAGNETIC MODELLING AND MEASUREMENTS

by

Claire Carvallo

A thesis submitted in conformity with the requirements
for the degree of Doctor of Philosophy
Graduate Department of Physics
University of Toronto

¡ Forward in all directions!

Paleointensity determinations on basalts from the Emperor Seamounts and testing properties of FORC diagrams using micromagnetic modelling and measurements

Doctor of Philosophy, 2004, Claire Carvallo

Department of Physics, University of Toronto

Abstract

The intensity of the geomagnetic field recorded in rocks from the Emperor Seamounts was measured. Paleolatitudes determined from thermal demagnetization in the Thellier experiments support the hypothesis of a moving Hawaiian hotspot. Because of thermal alteration and the presence of titanomaghemite, the Thellier success rate was only 5%. The virtual axial dipole moment at 56 Ma was $(7.2 \pm 0.2)\times10^{22}$ Am^2, about 60% higher than the average value for the 300-0.3 Ma time period, although still within the error bounds of this average.

First-order reversal curve (FORC) diagrams give the coercivity and interaction field distributions of magnetic minerals and could be used to pre-select samples for paleointensity experiments. Micromagnetic modelling shows that non-interacting particles are manifested by a symmetrical single peak. When particles interact, splitting of the central peak on the interaction field (H_u) axis might explain the vertical spread observed on FORC diagrams.

I measured FORC diagrams on elongated SD particles at temperatures ranging from 20 K to 853 K. The median field of the profile through the FORC peak along the coercivity field (H_c) axis varies in proportion to the bulk coercive force. The half-width of a profile through the FORC peak parallel to the H_u axis is similar to independent measures of local interaction fields H_i. These properties support the interpretation of the FORC variables H_c and H_u as being equivalent to microcoercivity H_c and interaction field H_i, respectively, and validate the FORC method.

In nature, magnetic minerals usually occur as mixtures. The linear additivity of FORC diagrams was investigated, in order to study the possibility of separating magnetic mixtures into their components. Micromagnetic models of mixtures of magnetite and hematite and mixtures of magnetite with bimodal grain size distributions, as well as experimental

measurements, yield linearly additive FORC diagrams.

I compared FORC and Preisach diagrams measured on a range of natural and synthetic samples. I find a good agreement between both diagrams in the main features. Contours that are very close to the H_u axis are not imaged on a Preisach diagram. As a first approximation, FORC and Preisach diagrams are equivalent. However, the level of detail offered by FORC diagrams makes them more attractive to use than Preisach diagrams.

Acknowledgements

Many people have helped me throughout these four years of graduate studies. First, I am very grateful to my supervisor, David Dunlop, for having accepted me as a graduate student. I thank him for his enthousiastic guidance and constant support, for giving me a lot of opportunities to go to conferences, and for patiently reading through the various versions of this thesis and any proposal, report or paper I wrote during these four years. I also thank Özden Özdemir for many helpful discussions and for letting me use some of her samples, and Yongjae Yu for having been such a great lab partner during the two years we shared the lab, for always answering my questions and never refusing a discussion. I feel very lucky to have been able to do my PhD in the Toronto rock magnetism group.

Adrian Muxworthy's stay as a post-doctoral fellow in the rock magnetism group was very important for the main direction of my thesis. Adrian introduced me to FORC diagrams and some aspects of micromagnetic magnetism that were new for me. During his stay, he spent countless hours helping me put together the micromagnetic model of FORC diagrams, discussing it with me, and answering any questions I had. Even after he left, Adrian was always ready to help me. I felt grateful to him many times during the course of my PhD for incredible patience and constant encouragement. I acknowledge the use of Tom Wright's FFT micromagnetic code, and I thank Wyn Williams for his help with the technical aspects of the code.

My work on the Emperor seamounts would never have been possible if John Tarduno had not offered me the opportunity to sail on ODP Leg 197 as a shipboard scientist. Besides giving me the chance to participate in a project which sought to answer one of the most exciting questions of plate tectonics, the cruise will always stay in my memory as a highlight of my scientific life. While at sea, discussions with Johannes Stoll, Pat Thompson, Jill Gudding, Florence Einaudi, Arno Buysch and many other scientists and crew members helped me to keep some mental sanity. I acknowledge the generous support of ODP Canada, which also enabled me to go to Hawaii for the post-cruise meeting. While in Hawaii, Dave and Zane offered me the possibility of seeing the active lava flow, and this was also a highlight of my scientific life. I am grateful to Rory Cottrell for her help with cutting my samples.

Chris Pike offered me a lot of advice for my work on FORC diagrams. I thank him for letting me use the "FORCAnalysis" software and being so helpful and patient with my questions. I also thank Andrew Roberts for interesting discussions on FORC diagrams, and Kenneth Verosub for having invited me to the 1st International Workshop on Magnetism, Hysteresis, and the FORC Method, which was held in Davis in April 2003.

I thank the Institut for Rock Magnetism for two Visiting Fellowships in September 2002 and October 2003. Mike Jackson, Jim Marvin and Peat Solheid helped a lot as I familiarized myself with the wonderful equipment. Thanks to Pierre Camps for the Poker Jim sample. Thanks to Jacob Hanley for helping with the thin sections and SEM analysis, to Lin Milne for letting me use the furnace, and to Wagih Ghobriel and Jim "Hamish" Luckett for helping me to enjoy my teaching experience as a TA. Thanks to Josh Feinberg for many discussions about FORC diagrams, and for his support.

I thank my PhD committee members Derek York, Jerry Mitrovica and Dick Bailey for following my work throughout these four years. Thanks also to Ted Evans and Bernd Milkereit for serving on my final examination committee.

I am very grateful to Jon Mound for many helpful discussions on various aspects of my thesis (in particular true polar wander, which is very difficult to measure), for sharing his experience as an ex-grad student and for always being helpful with any problems I had. I also thank my dear officemate Jill Pearse, and the geophysics grad students: Amy Daradich, Ele Willoughby, Rob Moucha, Roblyn Kendall, Elizabeth l'Heureux, Hernan Ugalde, and Michelle McGuire. Thanks also to Mark Tamisiea for patiently helping with computer-related questions and Katrin Schwalenberg and Nigel Edwards for introducing me to marine geophysics. I also thank Aldona, Caroline, Anna, Vicky, Tobias, Gwenaelle, Ariel, Ron and Alan for efficiently distracting me whenever needed (or not). Thanks to Loic for his inspiration. Thanks to Uncle Patrel for some good food and wine while staying at the Crazy Loquat. Thanks to Manu Chao, Sergent Garcia and JSB for keeping me company during late nights in front of the computer.

And finally, thanks especially to my dear Kalen, for helping with some computer-related problems, for always supporting me and always being here for me whenever I needed him.

Contents

List of Figures

List of Tables

Chapter 1

Introduction

1.1 General introduction

Rock magnetism is the study of remanent magnetization acquired by magnetic minerals occurring under natural conditions or synthesized in the laboratory. Rock magnetism developed initially to provide a physical understanding of the processes of magnetization recorded in rocks over geological periods of time. Therefore, reserach in rock magnetism is principally guided by the possible applications in paleomagnetism and related fields. The reliability of magnetic recording in rocks is crucial for paleomagnetism, which uses the orientation of the ancient field to reconstruct the movements of the lithospheric plates. This motion can be expressed as seafloor spreading, continental drift and plate tectonics. Understanding the workings of the core dynamo (the source of the geomagnetic field) passes through the study of paleosecular variation recorded in sediments, geomagnetic reversals and excursions, and variations of the geomagnetic field intensity. Environmental magnetism is becoming increasingly miportant nowadays. Magnetic minerals in soils, paleosols and loess record past changes in climatic conditions and rainfall through their composition and abundance, and also the timing of climatic episodes. Magnetic grains can also trace the provenance and dispersal of sediments, soils and pollutants.

In the first part of this thesis I present a detailed study of the intensity of the geomagnetic field recorded in basalts from the Emperor seamounts. The second part of the thesis deals with the development of a new method recently introduced in rock magentism for identifying

magnetic minerals and their grain size in natural assemblages.

1.1.1 Magnetic minerals relevant to this work

Magnetic minerals are described in details in O'Reilly (1984) and Dunlop & Özdemir (1997), for example. Magnetite ($Fe^{2+}Fe_2^{3+}O_4$) is the most important magnetic mineral on Earth. It is the main carrier of magnetization in igneous, sedimentary and metamorphic rocks, both in the continents and in the oceanic crust. Magnetite is a cubic mineral with spinel structure. Oxygen anions form a face-centered cubic lattice, with Fe^{2+} and Fe^{3+} cations in interstitial sites. A unit cell contains 8 cations on A sites, each surrounded by 4 O^{2-} anions at the corners of a tetrahedron, and 16 cations on B sites, each surrounded by 6 O^{2-} anions at the corners of an octahedron. The Curie temperature of magnetite is 580°C.

Below ≈120 K, there is an ordered arrangement of Fe^{2+} and Fe^{3+} ions in the octahedral sublattices and the unit cell is distorted very slightly from cubic to monoclinic symmetry. Above ≈120 K, electron hopping from Fe^{2+} to neighbouring B-site Fe^{3+}, converting the Fe^{2+} to Fe^{3+} and vice-versa, destroys the cation ordering. All <100> directions are equivalent and the lattice is perfectly cubic. The transition between these states is called the Verwey transition. The increased electron mobility then converts magnetite from an electrical insulator to a semi-conductor. The crystalline anisotropy, and all the magnetic properties that depend on it (coercive force, remanent magnetization, susceptibility) are greatly affected by the Verwey transition (Özdemir et al., 1993). In addition, at ≈135 K, the magnetocrystalline anisotropy constant K_1 becomes zero as it changes from negative to positive during cooling.

Titanomagnetites ($Fe_{3-x}Ti_xO_4$) are very common in the oceanic crust. Electrical conductivity falls rapidly with Ti^{4+} substitution and the Verwey transition is suppressed for x>0.1. Titanomagnetite has an inverse-spinel structure: Fe^{2+} cations are confined to octahedral sites, while Fe^{3+} cations populate A and B sites equally. The Curie temperature of titanomagnetite decreases linearily wih increasing x. TM60 (x=0.6) has a Curie point between 150 and 200°C.

Maghemite (γFe_2O_3) is the fully oxidized equivalent of magnetite. It is the ultimate low-temperature oxidation or weathering product of magnetite and is common both in subaerial and submarine environments. The Curie temperature of maghemite is around approximately

645°C (Özdemir & Banerjee, 1984). Cubic γ Fe_2O_3 is unstable and inverts to rhombohedral hematite (α Fe_2O_3) when heated. The degree of oxidation is measured by the oxidation parameter z.

Hematite (α Fe_2O_3) has a rhombohedral structure and is antiferromagnetic with a Néel temperature of 675°C. Below the Morin transition at -10°C, hematite is perfectly antiferromagnetic (Morin, 1950), but above the Morin transition, the sublattice magnetizations are canted by a fraction of a degree out of antiparallelism. This gives rise to a parasitic ferromagnetism with a spontaneous magnetization $\mathbf{M_s}$ in the basal plane, perpendicular to $\mathbf{M_A}$ and $\mathbf{M_B}$ (Fig. 1.1). The magnitude of M_s is about 2.5 kA/m, 200 times less than that of magnetite.

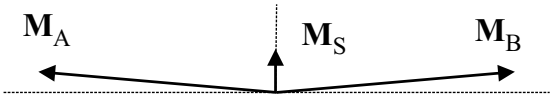

Figure 1.1: Canted antiferromagnetism: permanent deflections of the sublattice magnetizations when $\mathbf{H}$=0.

Underlying the canted antiferromagnetism is an isotropic ferromagnetism that is unaffected by the Morin transition (Dunlop, 1971). It is due to chemical or lattice moments, and is often called the defect moment. The single-domain range for hematite is much larger than for ferromagnetics, and lies between ~0.03 and 10-100 μm (Banerjee, 1971). Experimentally, the coercivity of single-domain hematite is high, because of magnetoelastic anisotropy due to internal stress.

1.1.2 Domain theory

Domain theory was developed by Landau and Lifschitz (1935). Without any experimental help they theorized that inside a ferromagnetic crystal, magnetic moments must be organized in domains inside which spins are aligned parallel to one another. Minimization of the internal energy of the crystal governs its domain structure. If the crystal is small enough the exchange energy dominates the total energy and the structure is single-domain (Fig 1.2a). If the grain size is larger the single-domain structure is no longer the state of minimum

energy. More domains can form because the demagnetizing energy becomes more important (Fig 1.2b, c). Domain walls are the transition zones within which the moments change direction between the domains. There are two types of walls: Bloch and Néel walls. In a Bloch wall, moments rotate in the plane of the wall. Néel walls occur in thin films below a certain thickness. In this case moments rotate in the plane of the film.

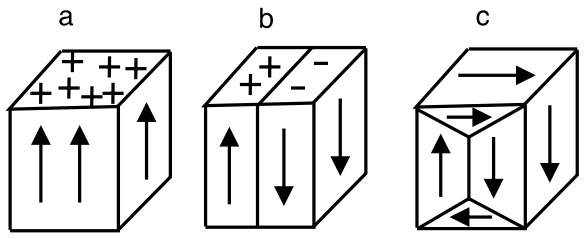

Figure 1.2: Examples of domain structures. a: single-domain structure; b: two-domain structure; c: two-domain structure with closure domains.

Below ~ 0.025 μm (Dunlop & Özdemir, 1997), magnetite is superparamagnetic (SP): its magnetization is unstable and decays to zero very soon after the removal of the magnetizing field. Magnetite is single-domain (SD) up to about 0.08 μm (Enkin & Williams, 1994). No sharp boundary exists between large SD grains and small multidomain (MD) grains. Instead, there is an interval of grain sizes exhibiting intermediate behavior. These grains are pseudo-single-domain (PSD) and are important carriers of magnetization. Their size range is from approximately 0.08 to 10 μm in magnetite.

1.1.3 Micromagnetism

Micromagnetic calculations were first introduced in rock magnetism by Brown (1963). In micromagnetic calculations, a crystal is divided into cells, usually cubic. The magnitude of the magnetization of each cell is constant, but the magnetization direction is varied independently through the angles θ_i, ϕ_i (Fig. 1.3) until a stable structure is found that minimizes the total energy. These structures are local energy minimum (LEM) states instead of global energy minimum (GEM) states. Since no constraints are applied to the system, such structures should be the same as those found in real samples. Three-dimensional models are much more computer-intensive than one- or two-dimensional models and this greatly reduces the

maximum cell resolution one can achieve. However, 3-dimensional models are much more representative of what we would expect in real samples. The model that I have used for micromagnetic calculations is the one developed by Wright et al. (1997), based on the model of Williams & Dunlop (1989). The energy minimization technique uses the conjugate-gradient (CG) method (Press et al., 1994). The code has been used and tested in many published studies (e.g., Williams & Dunlop, 1989, 1995; Williams & Wright, 1997, Wright et al., 1997)

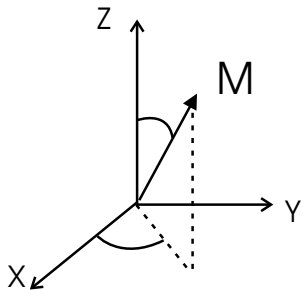

Figure 1.3: Coordinate system used in micromagnetic calculations.

The domain structure, and therefore the magnetic behaviour, of a material is controlled by a number of energy terms. The energy of a magnetic dipole $\mathbf{m}$ is the sum of the following energies:

- The exchange energy is due to the magnetic coupling of the spins $\mathbf{S_i}$ and $\mathbf{S_j}$ of nearest-neighbour atoms. Over the entire grain:

$$E_E = 2C_E \sum \mathbf{S_i}.\mathbf{S_j} \tag{1.1}$$

  where C_E is the exchange constant.

- The demagnetizing energy is due to magnetostatic dipole-dipole interaction. It expresses the interaction of the crystal magnetization with the demagnetizing field created by the induction field.

$$E_D = -\mu_0 \sum_{i=1}^{N} \mathbf{m_i}.\mathbf{H_{ind,i}} \tag{1.2}$$

  where $\mathbf{H_{ind}}$ is the field at $\mathbf{m_i}$ due to all the other dipoles in the system. This term is the most time-consuming to evaluate.

- The external field energy is created by the the field applied to the system:

$$E_H = -\mu_0 \sum_{i=1}^{N} \mathbf{m_i}.\mathbf{H_{ext}} \tag{1.3}$$

where $\mathbf{H_{ext}}$ is the external field applied to the system.

- The anisotropy energy. Because of lattice configuration, magnetic materials have directions of preferred magnetization orientation. In magnetite, the anisotropy is cubic and the anisotropy constant K_1 is negative, which means that the moments prefer to align along the diagonals of the cube. The magnetocrystalline anisotropy energy is then:

$$E_a = \sum_{i=1}^{N} K_1(\alpha^2\beta^2 + \beta^2\gamma^2 + \gamma^2\alpha^2) + K_2(\alpha^2\beta^2\gamma^2) \tag{1.4}$$

where (α, β, γ) are the direction cosines of $\mathbf{m_i}$ and K_1 and K_2 are the magnetocrystalline anisotropy constants. Since $\alpha^2+\beta^2+\gamma^2 = 1$, $\alpha^4+\beta^4+\gamma^4 = 1-2(\alpha^2\beta^2+\beta^2\gamma^2+\alpha^2\gamma^2)$. Therefore, when ignoring the higher powers, the anisotropy energy can be re-written as (Stacey & Banerjee, 1974):

$$E_a = \frac{K_1}{2} - \frac{K_1}{2} \sum_{i=1}^{N} (\alpha^4 + \beta^4 + \gamma^4) \tag{1.5}$$

For elongated crystals at room temperature, the shape anisotropy in E_D introduced by the elongation is much larger than the magnetocrystalline anisotropy energy. Therefore E_a can be ignored in this case. For micromagnetic calculations in magnetite, the anisotropy is sometimes approximated by uniaxial anisotropy. Then the easy axis is the z-axis. The uniaxial magnetocrystalline anisotropy energy is:

$$E_a = K_1 \sum_{i=1}^{N} sin^2\theta_i \tag{1.6}$$

where θ_i is the angle between the magnetization $\mathbf{m_i}$ and the easy axis.

In cases where I modelled an elongated grain, magnetocrystalline anisotropy energy was not included. If the elongation q exceeds 1.1, the shape anisotropy will dominate over the magnetocrystalline anisotropy (Dunlop & Özdemir, 1997).

Magnetostrictive energy (created by the spontaneous change in the dimensions of the crystal when it is magnetized) was also omitted because it does not have a significant effect on the domain structure for particles smaller than $\sim$4 μm (Muxworthy & Williams, 1998). The particles modelled in this study are defect-free and stress-free, so I did not include magnetoelastic energy (strain dependence of crystalline anisotropy) in the model.

The resolution of the models is determined by the size of the cell edge, which has to be smaller than half the exchange length $d_{ex} = \sqrt{\frac{2C_E}{\mu_0 M_s^2}}$, where C_E is the exchange constant (Rave et al., 1998). The room-temperature values of the magnetic constants used are: M_s= 480 kAm^{-1} (Pauthenet & Bochirol, 1951), C_E= 1.3$\times$ 10^{-11} Jm^{-1} (Heider & Williams, 1988), and K_1= –1.25$\times$ 10^4 Jm^{-3} (Fletcher & O'Reilly, 1974).

The model does not include the effect of thermal fluctuations. Simulated annealing (SA), which imitates the effect of thermal fluctuations in a random, undirected procedure (e.g. Thomson et al., 1994) increases computational time by orders of magnitude compared to the directed CG algorithm. The high resolution that is required to model arrays of particles makes it impossible to use SA in my calculations. SA and other pseudo-thermal perturbation methods generally find somewhat lower energy states than the CG method, but the differences are not large (Thomson, 1993), nor are they vital in the application in this work.

1.2 FORC diagrams

1.2.1 Motivations

The magnetic properties of natural samples are governed by the composition, the grain-size distribution and the interactions among the magnetic particles within the sample. Domain state and composition of magnetic minerals need to be accurately characterized when studying natural magnetic systems in paleomagnetic, environmental and paleoclimatic studies (Thompson & Oldfield, 1986). For instance, the reliability of magnetic recording in rocks, which is critical for paleomagnetism, depends on mineralogical parameters such as the grain size and the composition of the assemblage that carries the magnetic signal. SD particles are

the most reliable recorders of natural remanent magnetization (NRM). They also constitute the ideal material for paleomagnetism and paleofield intensity determination by the Thellier-Thellier method (Thellier & Thellier, 1959). Small PSD grains (up to $\sim$1 μm) still carry a stable remanence and behave almost ideally in Thellier-Thellier paleointensity experiments. MD grains carry the least stable remanence and are the least useful for paleointensity determinations (Levi & Merrill, 1978). Magnetostatic interactions in SD assemblies strongly reduce the intensity of TRM (Dunlop & West, 1969). Interaction among particles is another factor that leads to the failure of paleointensity experiments because the three Thellier laws of partial TRM (reciprocity, independence and additivity) are violated in the presence of an interaction field. Therefore, it is important to be able to determine both the particle size and the magnetic interaction state in a natural assemblage.

Magnetic grain size is usually determined by measuring the ratio of the saturation remanent magnetization $M_{\rm rs}$ over the saturation magnetization $M_{\rm s}$ and the ratio of the remanent coercive field $H_{\rm cr}$ over the coercive field $H_{\rm c}$. Day et al. (1977) showed that these parameters plot in different regions on a diagram of $M_{\rm rs}/M_{\rm s}$ versus $H_{\rm cr}/H_{\rm c}$ depending on the grain size. However, interpretation of these hysteresis parameters can be ambiguous (Dunlop, 2002a, b). Interactions are also difficult to detect in a bulk sample. The Henkel (1964) plot, which compares isothermal remanent magnetization (IRM) acquisition and DC demagnetization, cannot discriminate between a MD system and an interacting SD system if the mean grain interaction field is negative (Proksch & Moskowitz, 1994).

First-order reversal curve (FORC) diagrams, derived from Preisach diagrams, address most of these problems by providing separate representations of the coercivity distribution and the interaction-field distribution.

1.2.2 Preisach diagrams

The Preisach (1935) diagram has been used for many years by the magnetic recording community to represent assemblies of interacting particles. If a local interaction field H_i acts on an SD grain, the grain's hysteresis loop will be offset, producing unequal coercivities $a = H_c - H_i$ and $b = -H_c - H_i$ (Fig. 1.4a). When plotting the grain distribution function $F(a, b)$ as a function of a and b, only grains with (a, b) in the fourth quadrant will carry a

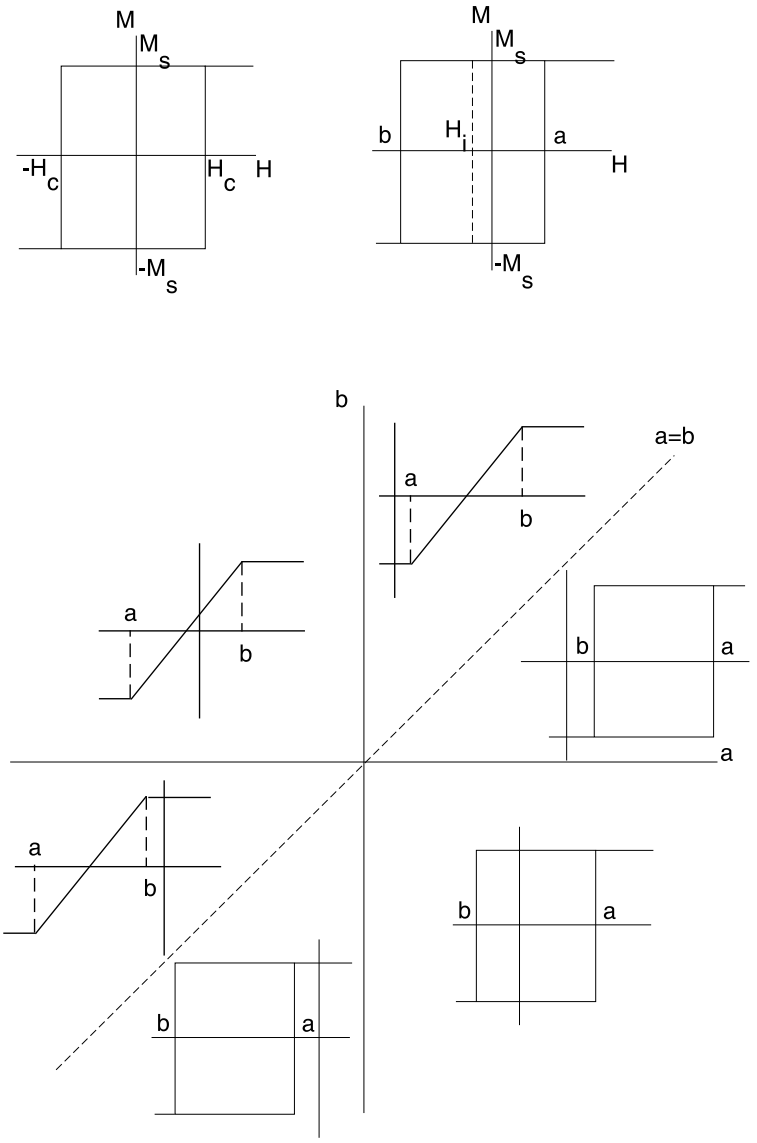

Figure 1.4: Top: elementary hysteresis loops of an SD grain with and without a constant interaction field H_i acting parallel to H_0 and the easy axis. Bottom: elementary reversible and irreversible magnetization cycles with (a, b) in different sectors of the Preisach diagram (from Dunlop et al., 1990).

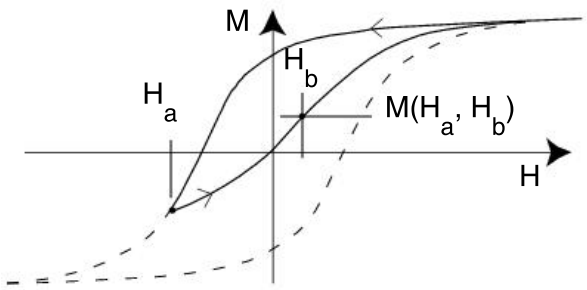

Figure 1.5: Example of the construction of the FORC diagram. From http://forc.ucdavis.edu/forc.shtml

stable remanence (Fig. 1.4b). Such a plot is a Preisach diagram. In Néel's (1954) interpretation of the Preisach diagram, the distribution $F(a, b)$ is the product of two independent distributions:

- $g(H_c)$ measured along the diagonal $a = -b$, represents the coercivity spectrum in the absence of interactions
- $f(H_i)$ measured perpendicular to $a = -b$, represents the distribution of grain interaction fields H_i

This interpretation strictly holds only for SD particles. There are many measurement protocols for Preisach diagrams. In some cases, Preisach distributions are required to be symmetrized, which might alter the distribution.

1.2.3 Definition of a FORC diagram

First-order reversal curve (FORC) diagrams have been introduced to rock magnetism by Roberts et al. (2000) as a new way of identifying minerals and domain states by measuring partial hysteresis curves. The theory underlying FORC diagrams is very similar to that of Preisach diagrams. The measurement protocol for Preisach diagrams is in some cases identical to the protocol used to measure FORC diagrams (e.g., Hejda & Zelinka, 1989). The main motivation for defining a new distribution is to avoid symmetrization which is sometimes required on Preisach diagrams: a FORC distribution is rigorously defined as a

mathematical transformation of a set of experimentally measured partial hysteresis curves. In that sense, FORC diagrams have been claimed to be less restrictive than Preisach diagrams.

The measurement of a FORC diagram begins by magnetically saturating the sample. The field is then decreased to a field $-H_a$ and increased again up to saturation through field steps H_b. This process is repeated for about 100 different values of H_a. The FORC distribution is defined by:

$$\rho(H_a, H_b) = -\frac{\partial^2 M(H_a, H_b)}{\partial H_a \partial H_b}, \tag{1.7}$$

where $M(H_a, H_b)$ is the magnetization measured at H_b (Fig. 1.5). A FORC diagram is a contour plot of $\rho(H_a, H_b)$ along axes ($H_c = \frac{H_b - H_a}{2}$, $H_u = \frac{H_b + H_a}{2}$) (Roberts et al., 2000).

The FORC distribution $\rho(H_a, H_b)$ at a point P is calculated by fitting a polynomial surface of the form $a_1 + a_2 H_a + a_3 H_a^2 + a_4 H_b + a_5 H_b^2 + a_6 H_a H_b$ on a local square grid with P at the centre (Roberts et al., 2000; Pike et al., 1999). The value $-a_6$ is $\rho(H_a, H_b)$ at P. The smoothing factor (SF) sets the size of the local square grid on which the polynomial fit of the magnetization is performed. The number of points on the grid is $(2SF+1)^2$ (Roberts et al., 2000; Pike et al., 1999). For example, an SF of 3 means that the smoothing is performed across a 7×7 array of data points. Smoothing is necessary in order to reduce the effect of measurement noise that is magnified by taking the second derivative. I used an SF between 3 and 5 in most cases. Positive regions on the FORC diagram are indicated by a light shading and negative regions by a dark shading .

Preisach distributions are measured by applying successive positive and negative fields, increasing in steps to saturation. Then the grain distribution can be worked out in squares on a grid. The double derivative that defines a FORC distribution is physically equivalent to this measurement process, on a smaller scale.

It has been shown both experimentally and theoretically that particles having different grain sizes and interaction states will plot in different areas of the FORC diagram (Roberts et al., 2000; Pike et al.,1999; Pike & Fernandez, 1999; Muxworthy & Dunlop, 2002). Non-interacting SD grains are characterized by closed contours extending along the H_c axis and with little vertical spread along the H_u axis. PSD grains show a closed-contour distribution that is more spread out along the horizontal axis, with its peak moving toward the H_u axis. For MD grains, the contours broaden along the H_u axis and ultimately form vertical

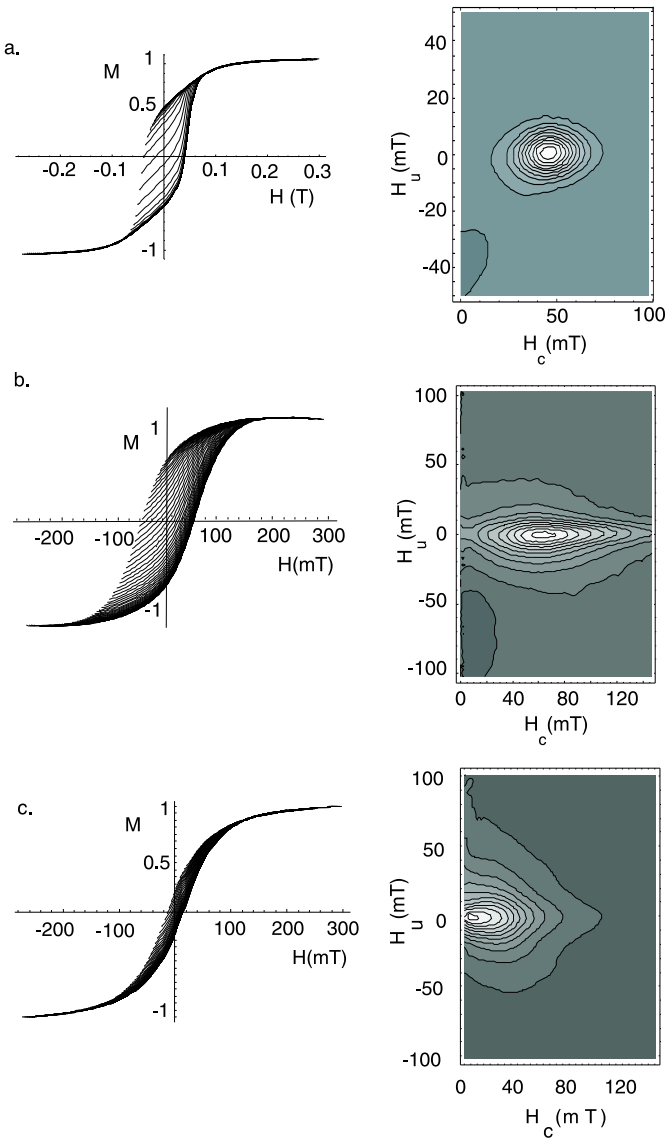

Figure 1.6: Example of FORC curves (left) and FORC diagrams for various samples. a: magnetotactic bacteria (SD); b: W4000 (SD) magnetite; c: W5000 (PSD) magnetite

contours. The presence of interactions usually produces a spreading of the distribution in the vertical direction on a FORC diagram. FORC diagrams can also be used to identify the presence of several magnetic minerals in a sample (e.g., Roberts et al., 2000). Fig. 1.6 shows some examples of FORC curves and FORC diagrams for various samples that I have measured myself.

1.3 Methods in paleomagnetism and paleointensity

1.3.1 Stepwise AF demagnetization

The role of progressive demagnetization techniques is to isolate the primary component of the magnetization acquired at the time of formation of the rock by cleaning from the sample any later magnetizations superimposed on the initial magnetization. AF demagnetization exposes a specimen to a sinusoidally varying magnetic field whose magnitude decreases smoothly with time. The field is applied in steps of increasing peak value, after each of which the residual magnetization is measured.

1.3.2 Thellier method of paleointensity determinations

Paleointensity determination compares natural remanent magnetization (M_{nr}) with magnetizations acquired in the laboratory. Assuming that the primary magnetization M_{nr} is a thermoremanent magnetization M_{tr} (magnetization acquired in cooling in the Earth's magnetic field from the Curie temperature, T_C), it is possible to compare it with M_{tr} acquired in a known laboratory field.

For a total thermoremanence acquired by a sample in an ancient field having an intensity H_a, the intensity of the remanent magnetization is:

$$M_{nr} = \alpha.H_a, \tag{1.8}$$

where α is a proportionality factor dependent on the size, shape and remanence recording quality of the magnetic grains.

The total TRM acquired by the same sample in the field H_{lab} is:

$$M_{tr} = \alpha'.H_{lab}, \tag{1.9}$$

If the remanence carriers do not experience any mineralogical changes during the experimentation and if the TRM is linear with the applied field, $\alpha = \alpha'$, and the paleofield H_a can be found from the relationship:

$$H_a = \frac{M_{nr}}{M_{tr}}.H_{lab}. \tag{1.10}$$

The method applied in this study is the Thellier double–heatings method (Thellier & Thellier, 1959) as modified by Coe (1969).

This method is based on three hypotheses concerning the properties of partial thermoremanent magnetizations (pTRMs):

- A pTRM acquired in a temperature interval (T_1, T_2) is independent of the pTRM acquired in any other non–overlapping temperature interval. Therefore the total TRM is the sum of the consecutive pTRMs (T_i, T_{i+1}).
- A pTRM is destroyed in the same temperature interval over which it has been acquired, which means that the blocking and unblocking temperatures are equal.
- The pTRM intensity is independent of the previous thermal treatments undergone by the sample.

After measuring the NRM at room temperature, the samples are heated to a first temperature T_i (here 250°C) and cooled to room temperature in zero field. The remaining NRM is carried by the grains whose blocking temperatures are between T_i and the Curie temperature. The remanence is measured and the NRM lost is calculated by vector subtraction of the previous remanence. Then the samples are heated again to the same temperature and cooled to room temperature in a known field H_{lab}. The change of remanence between the first and second heatings gives the partial thermoremanent magnetization (pTRM) acquired. Both this pTRM and the NRM lost are due to grains with blocking temperatures between room temperature and T_i, an interpretation first proposed by Néel (1949) for SD grains.

The double heatings are repeated in steps to higher and higher temperatures. The results are plotted as a graph of NRM remaining after the first of the two steps to T_i, versus pTRM gained in the second step to T_i. Ideally, if the remanence carriers are SD or small PSD grains, the graph, often called an Arai plot (Nagata et al., 1963), should be linear with a slope $-H_a/H_{lab}$. Viscous remagnetization (the remanent magnetization acquired over a long time in an external magnetic field) usually affects the lowest blocking-temperature fraction; this is easily recognized by non-linearity of the Arai plot at low temperatures. On the other hand, possible chemical transformations usually occur at high temperatures and result in non-linearity of the Arai plot at high temperatures.

Mineralogical changes are detected by using pTRM checks: the samples are heated in a field to a previously used lower temperature. If the new pTRM is the same as the pTRM obtained during the previous heating to the same temperature, one can conclude that the sample didn't experience any mineralogical transformation, except possibly ones that generate higher blocking temperatures. If the pTRM has changed, the new pTRM does not characterize the original mineral but rather its transformation product.

1.4 The Emperor Seamounts: Paleolatitudes and test of the motion of the Hawaiian hotspot

A significant part of this thesis deals with the measurement of paleofield intensity recorded in basalts from the Emperor Seamounts. The samples used were drilled during ODP Leg 197, whose primary goal was to test for motion of the Hawaiian plume relative to the mantle using paleomagnetic techniques.

This section presents the paleomagnetism preliminary results obtained on-board during ODP Leg 197 ("Motion of Hawaiian Hotspot") by the shipboard paleomagnetists. The results are published in Tarduno, J.A., Duncan, R.A., Scholl, D.W., et al. , 2002. Proc. ODP, Init. Repts., 197 [CD-ROM], available from: Ocean Drilling Program, Texas A&M University, College Station TX 77845-9547, USA.

1.4.1 Motivation

Measurements of plate motions in geodynamics depend on the reference frame used to express the displacement. In 1963, J. Tuzo Wilson proposed that linear chains of volcanic islands that do not occur on plate margins are created by "mantle hotspots" located in regions of the mantle where convective velocities are small (Wilson, 1963). These hotspots continue to feed a volcanic vent while the plate moves over it, creating a chain of progressively younger volcanoes. The "hotspot reference frame" has often been used as a convenient frame of reference to measure absolute plate motions (Morgan, 1971) and also to infer true polar wander, assuming that the sources of the hotspots remain fixed with respect to the mantle.

This assumption is now a source of controversy. If the motion of one plate over a hotspot is known and this hotspot is assumed to be fixed with respect to a hotspot under a second plate, one can use reconstructions of the past relative positions of the two plates to predict the position of the hotspot under the second plate (one component of motion usually remaining unknown) and compare it with its real track on the plate. Using this method based on global plate reconstructions, Molnar and Stock (1987) showed that there is a 10 to 20 mm/year differential motion between the Hawaiian and the Icelandic hotspots. Paleomagnetic data provide an independent way of testing hotspot motion. Data from ODP Legs 143 and 144 indicated significant motion at speeds typical of lithospheric plates (30 mm/yr) during the mid-Cretaceous between the Pacific and Atlantic hotspot groups (Tarduno & Gee, 1995).

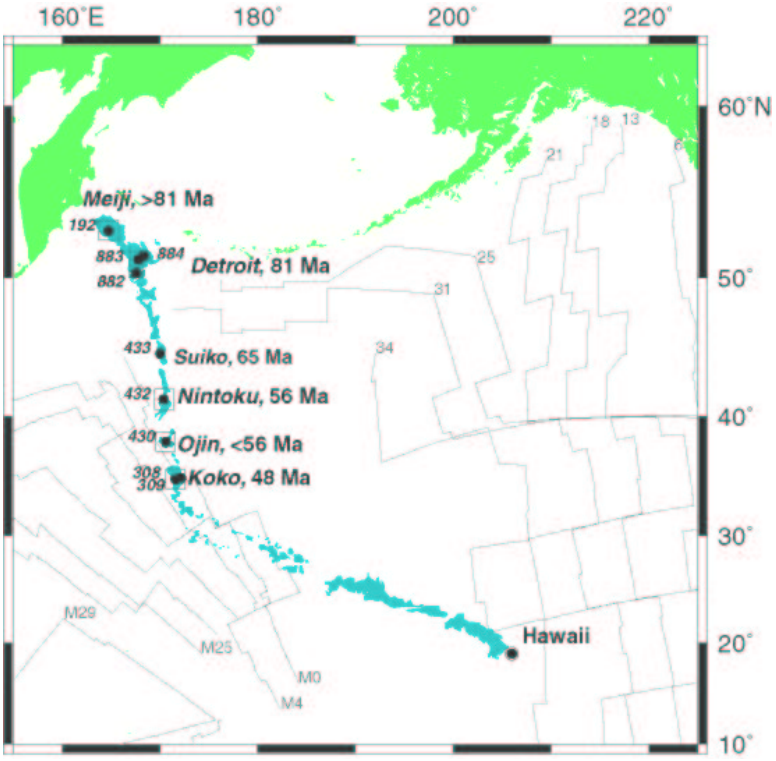

Figure 1.7: Geographical situation of the Emperor seamounts

In the context of a fixed-hotspot assumption, the bend between the Emperor and Hawaiian hotspot tracks (Fig. 1.7) was interpreted as a 60° change in the direction of motion of the Pacific plate relative to the deep mantle occurring ~43 Ma ago.

Alternatively, the bend might record primarily differences in motion of the Hawaiian

hotspot relative to the mantle. This view has been recently supported by a number of arguments:

• There is no evidence of a major tectonic event at the time of the bend that should have accompanied or even caused any abrupt change in the plate motion direction (Norton, 1995). Instead, the bend might record the time when the hotspot became fixed to the mantle. If so, prior to 43 Ma the hotspot was moving southward as it created the Emperor chain.

• Spreading rate data from the marine magnetic anomaly record of the North Pacific do not show any obvious change at 43 Ma, the age corresponding to the bend (Atwater, 1989).

• Finally, new mantle flow modeling using a viscosity structure based on geoid and seismic tomography constraints also predicts motion of hotspot groups (Steinberger & O'Connell, 1998). For the Emperor chain, the predicted motion is as large as 10-15 mm/yr.

The hypothesis of hotspot motion can be tested independently using paleomagnetic data. If the secular variation is properly averaged out, if the hotspot has remained fixed with respect to Earth's spin axis, if the geocentric axial dipole hypothesis holds, and if the rotation axis does not move with respect to the mantle (no true polar wander, TPW), the paleolatitudes of extinct volcanoes comprising the Emperor chain should match the present-day latitude of Hawaii.

Data obtained from Detroit seamount on the Emperor chain drilled during Leg 145 suggested a paleolatitude of 36.2^{o} ($+6.9^{o}$/-7.2^{o}) (Tarduno & Cottrell, 1997), clearly discordant with the present-day latitude of 19^{o} of Hawaii. The other reliable paleoinclination value from the Emperor seamounts is for Suiko seamont (Kono, 1980a) and shows an $8^{o}\pm3^{o}$ difference between the paleolatitude measured on Suiko seamount and the present-day latitude of Hawaii (19^{o}).

In order to increase the database of paleolatitudes on Emperor seamounts, one needs to recover samples from several other sites on different seamounts. The paleomagnetic objectives of the Leg were to obtain cores from lava flows suitable for paleolatitude and radiometric age determinations by drilling five or six basement sites on Detroit, Ojin and Nintoku Seamounts. ODP Leg 197 took place from July 2nd to August 28th, 2001.

1.4.2 Shipboard paleodirectional measurements

The paleomagnetic measurements on board the JOIDES Resolution were conducted by Rory Cottrell, Masayuki Torii and myself. Shipboard paleomagnetic investigations were limited by the instruments available in the well-equipped shipboard laboratory. The principal objective of the preliminary measurements carried out at sea were to derive paleolatitude estimates for the sites drilled. We also tried to address the question of the reliability of these measurements by performing rock magnetic measurements such as bulk susceptibility and Koenigsberger ratio. We used one-inch minicore samples taken from the working core halves.

The only experiments we could do onboard to characterize the magnetic domain state were Lowrie-Fuller tests (Lowrie & Fuller, 1971) and isothermal remanent magnetization acquisition and coercivity of remanence measurements. The Lowrie-Fuller test is based on the experimental observation that in large MD grains, strong-field TRM requires larger destructive fields than weak-field TRM to reach the same normalized remanence level. In practice the strong-field TRM is usually represented by a laboratory saturation IRM (SIRM) and the weak-field TRM by an anhysteretic remanent magnetization (ARM). Given an unknown magnetic mineralogy, the test can be considered only as qualitative because changes in magnetic coercivity related to different magnetic minerals can mimic changes in magnetic grain size.

SIRM's were imparted in the +x direction using an IM-10 Impulse Magnetizer until the saturation remanence M_{rs} was reached. Then they were DC demagnetized by giving them IRM's in the -x direction. The remanence decreases to zero at a field equal to the coercivity of remanence H_{cr} and culminates in -M_{rs}, the negative saturation remanence. These tests and measurements were very time-consuming, so only a few samples were measured (typically one per lava flow), to give an idea of grain size and also to help future selection of samples destined for paleointensity experiments.

Alternating-field demagnetization was performed to isolate characteristic remanent magnetization (ChRM) components and identify magnetic overprints. The ChRM directions were then determined using principal component analysis (PCA) (Kirschvink, 1980). ChRM inclinations derived from samples of each lava flow were averaged according to the method

of McFadden and Reid (1982). The time scale between flow eruptions plays an important role in obtaining reliable paleolatitude data. If most flows erupted in a short time, the paleolatitude estimate derived by giving equal weight to each flow unit would be biased. To alleviate this problem the inclination averages obtained for each flow were checked for serial correlation using geological constraints (visual core descriptions, for instance) as well as thin section observations and geochemical analysis. The directional angular dispersion estimated from the inclination groups was then transformed into geomagnetic pole space (Cox, 1970). The estimates of angular dispersion were compared to global data syntheses (McFadden et al., 1991) to check whether we sampled enough time for a given basement flow unit to average out secular variation. Finally we calculated mean paleolatitudes and 95% confidence intervals.

Alternating-field demagnetization and remanence measurement were carried out using mainly a pass-through 2-G Enterprises DC-Superconducting Quantum Interference Device (SQUID) rock magnetometer (Model 760R). Samples were demagnetized with an in-line demagnetizer (2-G Model 2G600) in fields up to 80 mT. This device allowed us to demagnetize four samples at a time in about 30 minutes (with about 8 field steps). We occasionally used a Model D-2000 DTech Inc. AF demagnetizer (maximum peak field 200 mT) and a Molspin Minispin spinner magnetometer for AF demagnetization. Low-field magnetic susceptibility was measured using a Geofysika Brno Kappabridge KLY-2 magnetic susceptibility meter.

Depending on recovery, we tried to select at least four samples per section, but our priority was to save the best material for shorebased thermal demagnetizations and paleointensity experiments.

1.4.3 Site 1203 (Detroit Seamount)

Detroit seamount was chosen to sample the oldest (Late Cretaceous) part of the Emperor Seamount chain located in international waters. Previous paleomagnetic and radiochronological analysis on material from this seamount indicated a paleolatitude of 36.2^o (+6.9^o/-7.2^o) (Tarduno & Cottrell, 1997). at 81 Ma (Keller et al., 1995). These data suggest considerable motion of the hotspot. However only 87 meters of basement were drilled, which was not enough to average the secular variation adequately, resulting in a large error bar on the

paleolatitude. This is why site 1203 ((51.0°N, 167.4°E) on Detroit Seamount was chosen to obtain a longer magnetic record.

Basement was reached at 462 mbsf (meters below sea floor). The volcanic section was about 457 meters long. The basement section consists of 18 basalt lava flow units (216 meters of recovered core, with a good recovery rate of 56.5%), 12 volcaniclastic interbeds with occasional biogenic sediments and 1 recrystallized silty chalk interbed. According to shipboard thin section observations, the opaque mineralogy of the basalts is dominated by titanomagnetite, with secondary pyrite present in some sections. Trellis-type ilmenite from oxyexolution and maghemite/titanomaghemite lamellae were also present in some samples.

Two hundred and fifty-eight discrete samples were taken from cores of volcanic basement for rock magnetism measurements and AF demagnetization. Preliminary measurements of bulk magnetic susceptibilities, median destructive fields (MDF) and Koenigsberger ratios indicate that most of the recovered basalts are capable of preserving primary magnetizations and thus are good candidates for paleolatitude determinations. Most samples show a simple demagnetization pattern consisting of a viscous overprint erased after demagnetization to 10-15 mT and a stable single component identified as the ChRM. For the basalt samples, 199 out of 202 yielded characteristic remanent magnetizations, and for the volcaniclastic samples, 34 out of 56 . The rejected samples either did not give a stable component after demagnetization to 80 mT or the demagnetization data did not trend towards the origin of the orthogonal vector plots.

Sixteen out of the 18 lava flows recovered were sampled. All samples had normal polarity. Assuming that the directions are adequately represented by AF demagnetization, that secular variation is averaged by the section, and that very short time intervals between lava flows do not cause a bias in the mean, we can give the same weight to each flow: the mean inclination is then 48° (+7°/-11°). This corresponds to a mean paleolatitude of 29°(+6° / -8°). The distribution of paleolatitudes derived from these values is offset by about 10° from the latitude expected if Detroit seamount had been formed by a fixed hotspot at the latitude of Hawaii. These values are also within error bounds of the paleolatitude of 36° (95% confidence interval of ±7°) derived from the basalts recovered at ODP Site 884 on the eastern flank of Detroit seamount (Tarduno & Cottrell, 1997).

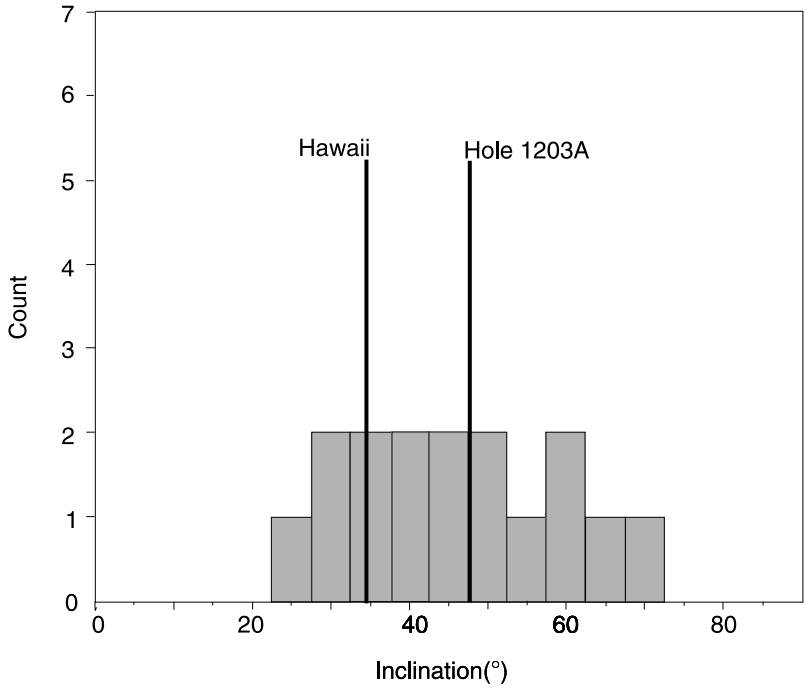

Figure 1.8: Histogram of inclination values from PCA of basalt flows recovered at Site 1203. From Tarduno et al. (2002)

1.4.4 Site 1204 (Detroit Seamount)

Site 1204 was targeted to be close to site 884 drilled by ODP Leg 145 in the summit region of the seamount. Basalt samples from the two holes drilled at this site gave paleomagnetic results consistent with the results from Site 884, but did not average the geomagnetic paleosecular variation adequately.

Two holes were drilled at site 1204: 1204A at 51°11.68'N, 167° 46.36'E and 1204B at 51° 11.64'N, 167° 46.42'E. Physical volcanology analysis suggests that the lava flows originated from subaerial vents and that the lava was emplaced in a near shore environment. Nannofossil assemblages present in sediments immediately overlying basement indicate an age of 71-76 Ma.

Basaltic rocks at this site can be classified into two types according to visual core descriptions, rock magnetic properties and thin-section observations. Most samples are light brown, their NRM is occasionally resistant to demagnetization up to 80 mT, and sometimes they do not show any directional stability during AF demagnetization. Thin section observation

reveals that the primary titanomagnetite grains have been partially to completely altered to titanomaghemite. Vesicles seem to be filled with iron-oxyhydroxides including goethite. We can infer that these samples were subjected to low-temperature oxidation. The presence of goethite could explain the fact that AF demagnetization seems inadequate to isolate a primary component of magnetization. The other type of mineral identified is green-gray and characterized by low MDFs and coercivity of remanence. Reflected light microscopy indicates the presence of unaltered titanomagnetite in relatively large grains as well as secondary pyrite. We can infer that some of the primary fine-grained titanomagnetite has been dissolved under reducing conditions. The magnetic properties might then be dominated by the multidomain titanomagnetite that survived oxidation.

About 70% of the minicore samples AF demagnetized at this site (Holes 1204A and 1204B) showed simple demagnetization patterns. For the remaining 30%, we could not isolate any ChRM component: in some cases a high-coercivity component was resistant to the 80 mT maximum field, in other cases the demagnetization behaviour showed a complex directional pattern. For Hole 1204A, only nine samples yielded a reliable paleolatitude estimate of 36.0° (inclination unit average: 55.5° with a 95% confidence interval of ±7.5°). However paleosecular variation is probably not averaged for this hole. Using 6 independent paleomagnetic units for Hole 1204B, the mean inclination is found to be 58.9° (+5.8°/-6.4°), corresponding to a paleolatitude of 39.7°N (+7.4°/-6.3°). All samples have normal polarity.

The results obtained at this site must be taken with caution. The directional data need to be confirmed by thermal demagnetization because of the alteration of the basalt section and the presence of goethite. Also the geomagnetic secular variation has not been adequately averaged at this site. However these preliminary results (36° and 40°) are consistent with the previous paleolatitude estimate of 36° ± 7° obtained from Site 884 basalts that did average secular variation.

1.4.5 Site 1205 (Nintoku seamount)

Nintoku seamount is in the middle of the Emperor Seamount chain. The seamount is an elongated edifice, aligned north-northwest along the Emperor trend. Site 1205 (41.2°N, 170.2°E) is located 100 m southwest of DSDP Site 432, where previous drilling had recovered termi-

nally oxyexsolved TM60 with good remanent magnetic properties (Kono, 1980b). However paleolatitude was not determined because the lava flow sampling was insufficient to average the paleosecular variation. The reported radiometric age for alkali basalt flows from Site 432 is 55-56 Ma (Dalrymple et al., 1980).

Drilling at Hole 1205A penetrated 283 m in the volcanic basement and recovered parts of at least 25 different lava flow units. Nannofossils in the sediments immediately overlying the basement constrains the age of the youngest volcanic rocks to be older than 53.6-54.7 Ma. From visual core descriptions, the presence of oxidized flow tops and soil horizons together with the lack of pillow structure indicate that the flows were erupted subaerially.

A total of 152 basalt minicores were sampled from the 25 lava flows recovered. Bulk magnetic susceptibilities measured on the minicores used for AF demagnetization were between 0.6×10^{-3} and 84.4×10^{-3} SI (mean= 27.5×10^{-3} SI). Koenigsberger ratios range from 0.7 to 80 (mean= 8.8). MDF's range from 3.1 mT to 63.3 mT (mean= 21.6 mT).

Most of the Lowrie-Fuller tests and coercivity of remanence measurements, carried out generally on at least one sample per lava flow, show consistent results: samples having SD-like Lowrie-Fuller tests also have relatively high coercive forces and vice-versa. However some samples give results that are less clear. Sometimes, the NRM demagnetization has SD-like behaviour whereas the ARM and SIRM demagnetizations are MD-like. This could be explained by the presence of near superparamagnetic (SP) viscous grains: SP grains have very short relaxation times compared to stable SD grains and carry an unstable magnetization in the presence of a magnetizing field. The rapid decay of ARM and SIRM curves might then represent the unstable acquisition of magnetization in near-SP grains.

Almost all the samples showed simple AF demagnetization behaviour with one stable component identified after demagnetization to 25 mT. About half the samples were not demagnetized to less of 10% of the NRM intensity after treatment to 80 mT, because of the presence of some high-coercivity minerals. However their remanence directions define a clear trend towards the origin of the vector plot. All samples were of reverse polarity. Some of the lava flows that are separated by flow tops rather than soil may actually have been emplaced during short periods of time with respect to the characteristic secular variation time scale. Therefore we regrouped some of these lava flows as one paleomagnetic inclination unit. In

the end, we sampled 22 paleomagnetic inclination units (from the 25 lava flow units). We obtained a mean inclination of -45.7° (+10.5°/-6.3°), corresponding to a paleolatitude of 27.1° (+10.8°/-5.2°). The relatively large inclination dispersion may be due to the fact that in some cases AF demagnetization was not the best method to demagnetize high-coercivity material.

The data obtained at Suiko Seamount (DSDP Site 433) on 65 Ma year-old lava flows suggest a paleolatitude of 27.0±4.8 ° (Kono, 1980a). This result averages the secular variation, and is in very good agreement with our result, in the sense that it is inconsistent with a fixed-hotspot hypothesis. Thermal demagnetizations are needed in order to confirm our paleolatitude value. Nevertheless this value is significantly different from the present-day latitude of Hawaii.

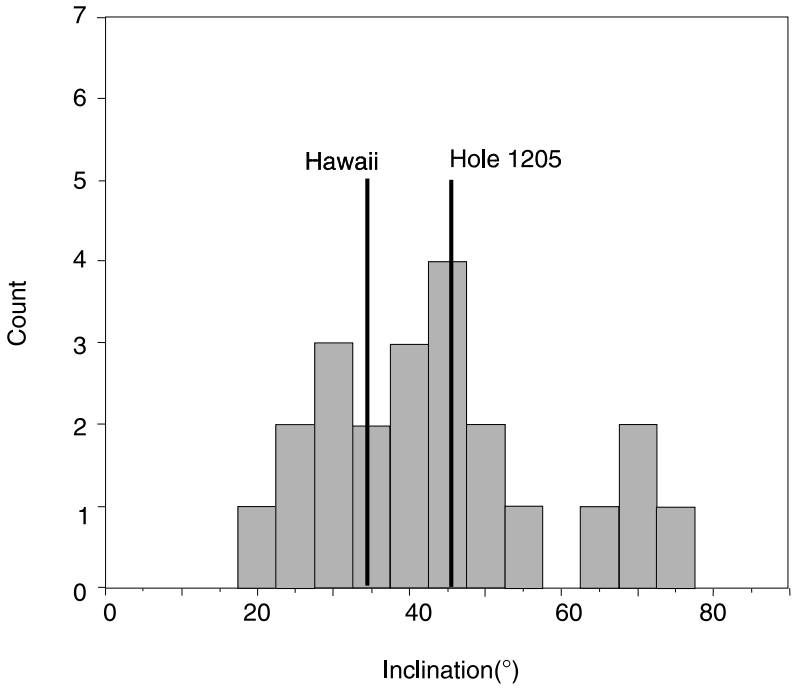

Figure 1.9: Histogram of inclination values from PCA of basalt flows recovered at Site 1205. From Tarduno et al. (2002)

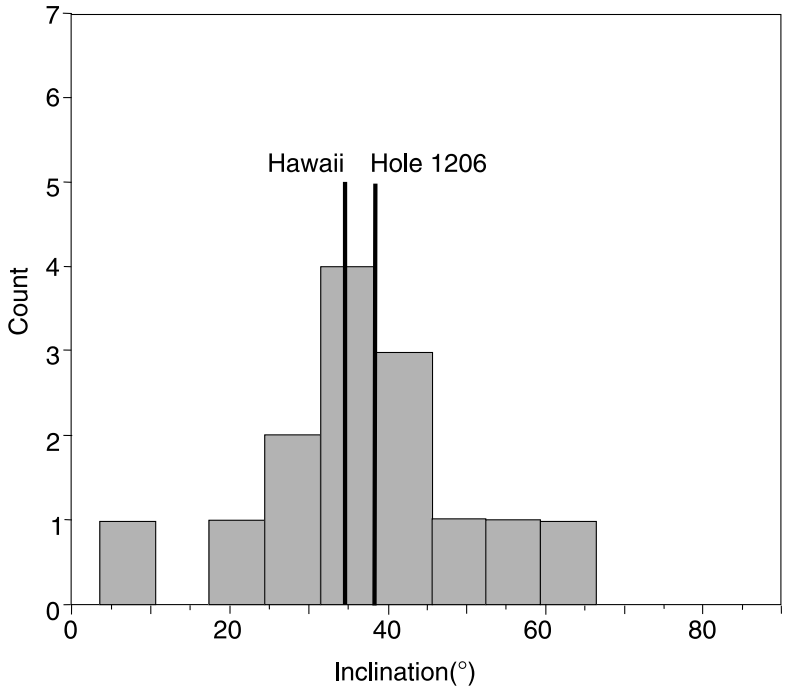

Figure 1.10: Histogram of inclination values from PCA of basalt flows recovered at Site 1206. From Tarduno et al. (2002)

1.4.6 Site 1206 (Koko seamount)

Koko seamount lies at the southern end of the Emperor Seamounts chain, about 200 km from the bend between Emperor and Hawaiian chain. Koko Seamount was identified as a guyot (Davies et al., 1972). The surface of the seamount remained above sea level long enough to be almost completely flattened by subaerial erosion and wave action. Site 1206 (35.0°N, 172.1°E) was located close to DSDP Site 308 in 1540 m of water. Drilling at Site 1206 encountered basement at 57 mbsf and drilled 278 m of a sequence of lava flows, hyaloclastites, volaniclastic sandstone and limestone. The recovery was 52%. The age inferred from nannofossil assemblages in the sediments immediately overlying the basement is 43.5–49.5 Ma. The basement was divided into 22 lithological units, including 15 lava flow units.

We studied 72 basalt samples from this hole. Bulk magnetic susceptibilities vary from 2×10^{-3} SI to 39×10^{-3} SI (mean value 14×10^{-3} SI). Koenigsberger ratios range from 1.8 to 72.0, with a mean value of 13.0. Some samples having high MDF were selected for Lowrie-Fuller tests and coercivity of remanence measurements. In all cases, the MDFs of ARM and

SIRM are smaller than the MDFs of NRM. However mixtures of magnetic grains having different grain sizes are sometimes observed: in these cases ARMs and SIRMs decrease rapidly and the coercivity of remanence is low. In some other cases, SD grains are present as indicated by sigmoid shapes of ARM and SIRM demagnetization curves and high values of coercive force. Some examples of more complex behaviour seem to indicate the presence of high-coercivity minerals such as goethite in some parts of the hole.

Both normal and reverse polarities were observed. Normal-polarity samples often had more than one magnetic component according to the curved vector diagrams at low fields. Three polarity intervals were recorded at Hole 1206. The mean inclination is -38.5°(+8.4°/-10.9°), corresponding to a paleolatitude of 21.7°(+6.4°/-7.0°).

1.4.7 Shorebased measurements

Shorebased measurements consisted of $^{40}Ar/^{39}Ar$ dating and thermal demagnetizations. Results are summarized in Table 1.1. For site 1204 (Detroit seamount), $^{40}Ar/^{39}Ar$ heating spectra from five samples failed to show plateaux in the step-heating ages.

Table 1.1: Summary of ages and paleolatitudes given by shorebased $^{40}Ar/^{39}Ar$ measurements and AF and thermal demagnetizations (Tarduno et al., 2003).

Site	Age (Ma)	λ(°) (AF)	λ(°) (thermal)
Hole 1203 (Detroit)	75.82±0.62	29.0° (+6.3°/-7.8°)	29.6° (+6.6°/-8.3°)
Hole 1204B (Detroit)		39.7° (+7.4°/-6.3°)	41.0° (+6.4°/-5.2°)
Hole 1205 (Nintoku)	55.50±0.25	27.1° (+10.8°/-5.2°)	26.0° (+13.0°/-7.4°)
Hole 1206 (Koko)	49.15±0.21	21.7° (+6.4°/-7.0°)	21.5° (+5.2°/-6.0°)

1.4.8 Implications for the motion of the hotspot plume

Results from both AF and thermal demagnetization show that the inclination groups form a progressive sequence of decreasing paleolatitudes with time, inconsistent with the fixed hotspot hypothesis (Fig. 1.11). Average rates between 20 and 70 mm/year can be inferred

from the inclination data. Most of the motion occurred before the time of the Hawaii-Emperor bend, as further confirmed by the paleolatitude of Koko Seamount only 2.5° north of the fixed-hotspot hypothesis. This is why the paleolatitude variation starts at about 40 Ma on Fig. 1.11).

A geodynamic model of the interaction of the plume with a large-scale mantle flow is consistent with the paleomagnetic results (Tarduno et al., 2003). Using the age of the initiation of the Hawaiian hotspot as a free parameter, computations using either a moving- or a fixed-plume model with a plume source at the top of the low-viscosity layer at the base of the mantle yield a hotspot motion of 5 to 10° towards the southeast during the past 100 Myr.

A number of paleomagnetic studies done on various basaltic flows support these results. Recent paleolatitude measurements on two sites from the Kerguelen Plateau (43.6°S (+4.2°/-5.7°)) are in disagreement with the present-day latitude of the Kerguelen hotspot (49.0°S), and suggest that the Kerguelen hotspot has moved 3-10° towards the south since its first appearance approximately 120 Ma ago (Antretter et al., 2002). In the same study, a numerical model of plume conduit motion in a large-scale mantle flow shows that TPW alone cannot explain this difference in latitude. Paleolatitudes measured on the early Cretaceous Ontong Java Plateau basalts are 20° north of the paleogeographic location calculated from Pacific hotspot tracks assuming the hotspots have remained fixed (Riisager et al., 2003). Again, this discrepancy cannot be explained by true polar wander estimates derived from other lithospheric plates.

The hotspot motion defined by the new Emperor seamounts paleomagnetic data has implications for a wide variety of issues which are based on the fixed-hotspot hypothesis. TPW curves are established using a fixed hotspot hypothesis. Since this hypothesis has been proved not to be valid at all times, TPW paths must be modified to take account of hotspot motion. In any case, these new data show that care must be taken before differences between hotspot and paleomagnetic data are interpreted to reflect the rotation of the entire solid Earth. Changes in the morphology of the geomagnetic field with time that have relied on a fixed hotspot frame must also be viewed with caution. The results from the Emperor chain show that changes in plate motion at the time of the bend were much smaller than previously

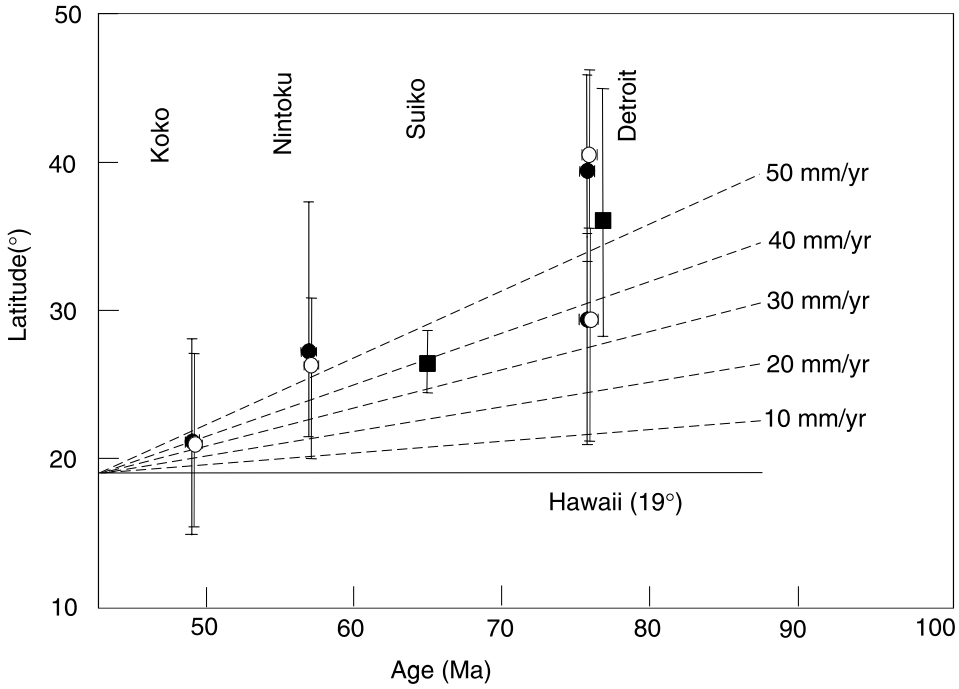

Figure 1.11: Summary of the paleolatitudes measured during Leg 197 (open circles: thermal demagnetization results; closed circles: AF demagnetization) and comparison with the two other available values (squares: Tarduno and Cottrell, 1997; Kono, 1980a). After Tarduno et al. (2003)

thought. These observations question the assumption that major plates can undergo rapid changes in their motions.

Chapter 2

Paleointensity determinations, paleodirections and magnetic properties of basalts from the Emperor seamounts.

Most of Chapter 2 has been published as: Claire Carvallo, David J. Dunlop, Özden Özdemir, Paleointensity determinations, paleodirections and magnetic properties of basalts from the Emperor Seamounts, *Geophys. J. Int.*, **156**, 29-38, 2004, and as: Claire Carvallo, David J. Dunlop, Özden Özdemir, Corresction to: Paleointensity determinations, paleodirections and magnetic properties of basalts from the Emperor Seamounts, in press.

2.1 Introduction

A knowledge of the long-term variation of paleofield intensity is essential for a complete description of the geomagnetic field. The most reliable method of determining paleointensity is the Thellier-Thellier method (Thellier & Thellier, 1959) because it reproduces the process of TRM acquisition by heating a sample in a laboratory field. However numerous selection criteria have to be satisfied in order to ensure reliable paleointensities. The paleointensity database for the Late Cretaceous- Early Tertiary period consists mainly of data obtained

by the Shaw method (Shaw, 1974) or by the Thellier-Thellier method but with restricted use of selection criteria assessing the reliability of the results . The virtual axial dipole moments (VADMs) measured are in general low, but show a considerable dispersion. Thus it is important to acquire more paleointensity data in this time range, making sure that all the selection criteria are obeyed.

In submarine basalts, the most abundant primary magnetic mineral is titanomagnetite, $Fe_{3-x}Ti_xO_4$, with x≈0.6, usually containing Al and Mg impurities. Rock magnetic properties of sea-floor basalts have been extensively studied (for example, Smith and Banerjee, 1986). The oxidation of titanomagnetite at low temperatures (less than 250°C) produces titanomaghemite. The original TRM is then replaced by a chemical remanent magnetization (CRM) of reduced intensity, but the direction of the TRM is preserved. This process is common in submarine basalts. As a result, there have been few studies of paleointensity using submarine basalts and because of maghemitization these have probably yielded paleointensity values that are too low (Carmichael, 1977; Dunlop & Hale, 1976). However, Grommé et al. (1979) obtained reasonable paleointensities both on fresh (unoxidized) samples, and on somewhat oxidized ($z \approx 0.2$) titanomagnetites. Kono (1980c) carried out paleointensity measurements on basalts from the Emperor seamounts Ojin, Nintoku and Suiko; almost all of his samples showed evidence of high-temperature oxidation of titanomagnetite but little or no low-temperature oxidation, and yielded reliable paleointensity results.

In this chapter I present paleodirectional and paleointensity determinations carried out using the Thellier-Thellier method on submarine basalts drilled on the Emperor seamounts during ODP Leg 197. I also report rock magnetic properties that help to assess the reliability of these determinations.

2.2 Sampling

I selected sixty-seven samples for a first set of paleointensity experiments: from Detroit seamount, fifteen samples from three different lava flows (5 samples per flow) from Hole 1203A, and five from Hole 1204B, all from the same lava flow; thirty-two samples from six lava flows from Nintoku seamount, and fifteen samples from three different lava flows from

Koko seamount. Location of the seamounts is shown in Fig. 1.7. AF demagnetization of TRM, isothermal remanent magnetization (IRM) and anhysteretic remanent magnetization (ARM), as well as thin section observations, were used to select the flows that seemed to be the most favorable for paleointensity determinations (Tarduno et al., 2002).

After carrying out Thellier experiments on this first set, I obtained twenty-six more samples from the lava flows that gave the most promising results: sixteen from Nintoku and ten from Koko. All of the samples were oriented according to ODP conventions: the z-axis of the sample is downhole, parallel to the z-axis of the drill core and the x-axis is the line perpendicular to the split face (YZ plane) and directed into the working half of the drill core. Five samples were cut as cubes with arbitrary orientation, because they were too small to cut a whole minicore.

The sample identification follows ODP conventions. A complete identification number for a sample consists of the following information: leg, site, hole, core number, core type, section number, and interval in centimeters measured from the top of the section. For example, a sample identification of "197, 1205A, 18R2, 16-18cm" indicates a sample taken from the interval between 16 and 18 cm below the top of section 2, core 18 of Hole 1205A during Leg 197. 'R" designates that this core was taken during rotary drilling. Since all the samples used here were drilled during Leg 197, I have omitted the leg number from the sample names.

2.3 Paleointensity measurements

2.3.1 Experimental procedure

I used the Thellier-Thellier method as modified by Coe (1969), described in §1.3.2., with a laboratory field $H_{lab} = 40.0 \pm 0.2\mu$T for the first set of samples, and 20.0 or 30.0 $\pm 0.2\mu$T for the second set of samples, depending on the anticipated paleofield value. pTRM checks as well as pTRM tail checks (Riisager et al., 2000) were done every second step. Samples were heated in small temperature steps (between 12 and 25°C, depending on the thermal behaviour of the samples). Temperatures at specific locations inside the MMTD furnace were reproducible to within ± 2°C. Each heating-cooling step required about 3-4 hours. The

samples were heated at a rate of 30°C/min, held at the maximum temperature for 40 min, and cooled to room temperature at a rate of 30°C/min. All the samples were heated in air. Bulk magnetic susceptibility was measured after each temperature step in order to detect mineralogical changes. The best-fit determination and statistical analysis of the results follow the least-squares fitting method described by York (1969).

The various parameters used as selection criteria are as follows:

- The number N of points contained in the segment chosen to determine the paleointensity must be at least 4.
- The parameter f that measures what fraction of total remanence was destroyed in the segment used for the paleointensity determination must be more than 1/3.
- The quality factor S' calculated from the least-squares fitting cannot exceed the quality factor defined for a 99% confidence limit based on a χ^2 distribution (Yu et al., 2000).
- The variation of bulk susceptibility over the temperature interval used for the paleointensity estimate must be less than 15%.
- The mean angular deviation (MAD) calculated from principal component analysis (Kirschvink, 1980) must be less than 15° over the temperature interval used for paleointensity determination.
- The angle α between the fitting line constrained through the origin and the direction of the characteristic remanent magnetization must be less than 15°.

The pTRM check reproducibility is tested by calculating $\frac{pTRM_2 - pTRM_1}{pTRM_{total}}$, where $pTRM_1$ and $pTRM_2$ are the first and repeated pTRMs, and $pTRM_{total}$ is the maximum pTRM in the temperature interval used for the paleointensity measurement. I required this parameter to be lower than 10% for the acceptance of the paleointensity estimate. I consider that pTRM tail checks are positive if the difference of intensity between the two heatings in zero field at the same temperature divided by the NRM is less than 10%.

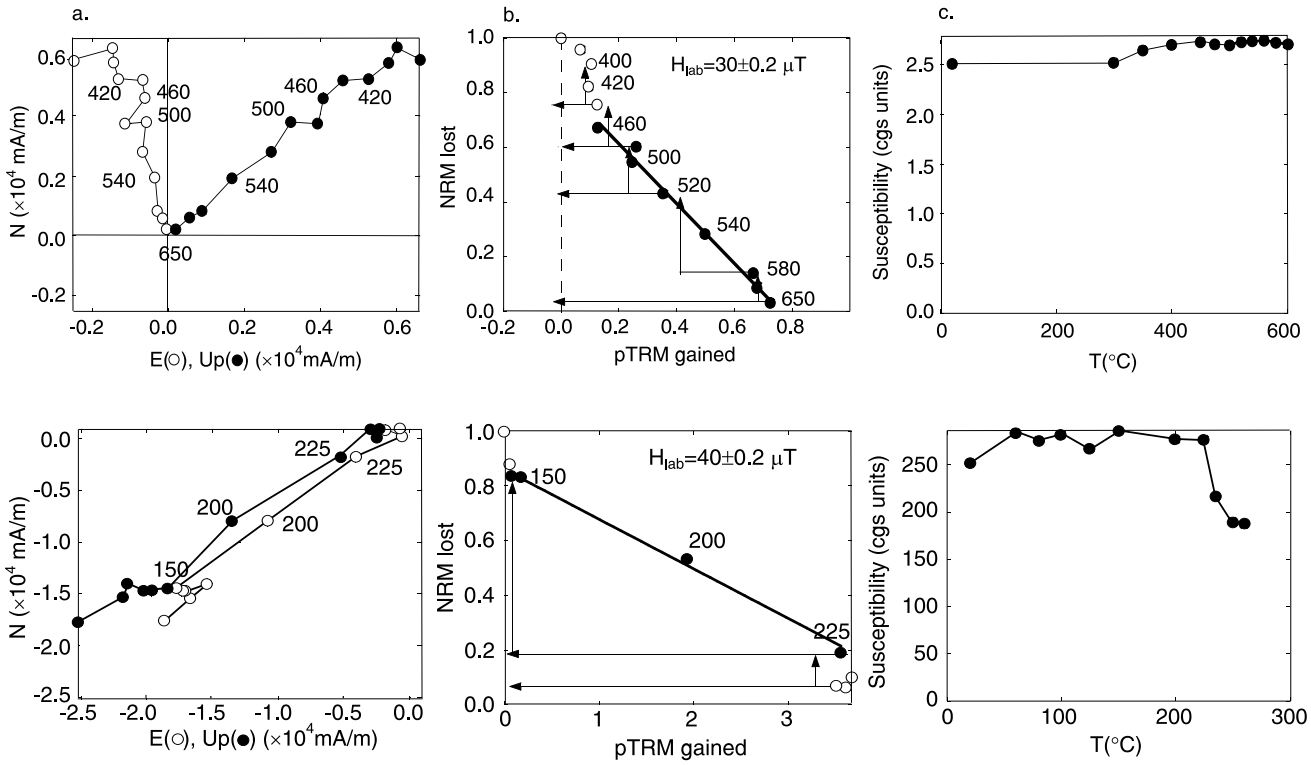

Figure 2.1: Zijderveld diagram (a), Arai plot (b) and susceptibility variation with temperature (c) for sample 1205A-41R-5, 95-97cm (top) and 1206A-22R3-3-5cm (bottom). Arrows point towards pTRM checks and pTRM tail checks.

2.3.2 Results

Out of all the samples, seventeen samples gave reliable paleointensity results (one from Detroit, ten from Nintoku and six from Koko). Results are summarized in Table 2.1 (details in Appendix A-2). Two examples of Arai plots, susceptibility variations and Zijderveld plots for two samples that passed the selection criteria are shown in Fig. 2.1.

The failure of more than 80% of the samples is mostly due to mineralogical changes during the repeated heatings, as indicated by large susceptibility variations and non-repeatability of pTRM checks. I suspect that titanomaghemite in some samples inverted to strongly magnetic magnetite. This is indicated by a strong increase in bulk susceptibility as a result of heating. Most samples are characterized by a very narrow unblocking temperature range. A striking feature is the large variation in Curie temperatures and demagnetization behaviour that I observed both between seamounts and even within a single hole, revealing important

Table 2.1: Paleointensity results. Symbols are defined in the text. Samples with an asterisk are from the second set.

Sample	N	$\Delta T(^{o}\mathrm{C})$	f	S'	$H \pm \sigma_H(\mu T)$	$MAD(^{o})$	$\alpha(^{o})$
1203A-49R-3, 79-81 cm	4	200–250	0.41	0.69	17.9±1.6	5.5	6.2
1205A-18R-2, 16-18 cm	6	450–520	0.36	0.30	19.8±2.3	6.2	14.4
1205A-27R-4, 60-62 cm*	4	200–250	0.47	1.01	21.2±2.4	8.4	9.6
1205A-27R-4, 72-74 cm*	4	200–250	0.58	1.16	17.9±1.6	5.9	10.1
1205A-27R-4, 97-99 cm	4	100–200	0.99	2.55	10.8±0.8	2.5	3.0
1205A-33R-2, 94-96 cm	4	125–225	0.48	0.08	21.9±2.2	12.0	11.7
1205A-33R-3, 87-89 cm	4	150–235	0.56	0.50	27.3±0.7	3.3	7.4
1205A-41R-5, 51-53 cm*	6	520–650	0.40	0.37	31.2±1.8	4.4	0.9
1205A-41R-5, 55-57 cm	6	510–630	0.56	0.05	34.8±1.8	1.9	0.3
1205A-41R-5, 66-68 cm	9	485–600	0.58	0.55	31.6±1.8	2.3	2.9
1205A-41R-5, 71-73 cm*	6	520–650	0.52	0.19	31.1±2.2	3.8	1.6
1206A-22R-1, 127-129 cm	4	100–200	0.64	0.07	6.6±0.4	3.2	6.4
1206A-22R-2, 31-33 cm	4	100–200	0.62	0.13	11.0±0.8	3.4	1.3
1206A-22R-2, 3-5 cm	4	125–225	0.65	0.79	8.2±1.9	4.8	6.6
1206A-32R-2, 117-119 cm	4	150–235	0.43	0.88	7.2±0.8	4.4	9.1
1206A-32R-2, 128-130 cm	4	125–225	0.60	0.55	4.3±0.3	4.0	12.4
1206A-33R-1, 45-47 cm*	6	100–200	0.71	1.56	8.2±0.5	9.9	11.0

variations in Ti content and oxidation state. According to the thermal demagnetizations, Curie points range between 250 and 550°C.

2.4 Paleodirection measurements

The zero-field steps during the Thellier experiments allowed me to calculate paleodirections for the 93 samples. Characteristic remanent magnetizations (ChRM) were determined using principal component analysis. About one-third of the samples altered during heating before a direction could be determined. I applied the following selection criteria:

- The maximum angular deviation must be less than 15°.
- The angle between the ChRM and the ChRM constrained through the origin of the Zijderveld diagram must be smaller than the MAD.
- The susceptibility variations must be less than 15%.

Forty-three samples gave reliable paleodirections according to these criteria. Next I averaged the inclinations for each unit using the method of McFadden and Reid (1982) for inclination-only data. Estimates of directional angular dispersion were transformed into estimates of pole dispersion using the formulas of Cox (1970). Out of the thirteen lava flows sampled for this study, only three, all from Nintoku seamount, yield reliable paleodirections, with the confidence limit $\alpha_{95}<15°$ and the precision parameter k more than 20 (Table 2.2).

Each of these three lava flows belongs to a unit identified using visual core description while on board (Tarduno et al., 2002). Samples named 27R4 belong to unit 12B, samples named 35R4 to unit 19B, and samples named 41R4 and 41R5 to unit 26A.

The inclinations agree with the results from AF demagnetization: -48.3°±10.7° for unit 12B against -62.9°±15.9° from AF demagnetization (Tarduno et al., 2002); -60.1°±2.0° for unit 19B against -64.9°±7.7° from AF demagnetization and -44.3°±1.7° for unit 26A against -45.3°±5.1° from AF demagnetization. The small number of directions does not allow me to calculate an average for the site. However my results are in general agreement with those from AF demagnetization (Tarduno et al., 2002). The paleolatitudes corresponding

Table 2.2: Characteristic remanent magnetization inclination averages based on thermal demagnetization results obtained during the Thellier-Thellier experiment. N: number of direction determinations within each unit; I: estimate of the mean inclination; α_{95}: estimate of the 95% confidence interval of inclination; k: estimate of the precision parameter; λ: paleolatitude derived from the inclination mean. The basalt unit numbers are the same as the numbers used by Tarduno et al.(2002)

Basalt unit	N	$I(^o)$	α_{95}	k	$\lambda(^o)$
12B	10	-48.3	6.5	57	-29.3
19B	5	-60.1	2.2	1711	-41.0
26A	4	-44.3	2.5	2253	-26.0

to the paleoinclinations are -29.3°±13.2°, -41.0°±3.5° and -26.0°±4.3°, respectively. All these values are significantly different from the present-day latitude of Hawaii (19°). The paleolatitude inferred from paleodirections after AF demagnetization obtained on 23 lava flows was -27.1°(+5.2°/-10.8°) (Tarduno et al., 2002, Fig. 1.7)

2.5 Magnetic properties

2.5.1 Room-temperature measurements

For all the samples, I measured natural remanent magnetization (NRM) and bulk magnetic susceptibility, as well as Koenigsberger ratio Q defined by:

$$Q = \frac{NRM}{\chi.H} \tag{2.1}$$

where H is the present day field. I used the values given by the International Geomagnetic Reference Field for the present-day field (48.7 μT at Detroit, 43.0 μT at Nintoku and 39.4 μT at Koko) (Barton, 1995). NRM values range from 0.70 to 15.01 A/m, but most are higher than 2 A/m. Bulk magnetic susceptibilities range from 157× 10^{-6} to 2900× 10^{-6} SI. NRM values and bulk susceptibilities are fairly consistent within lava flows but they

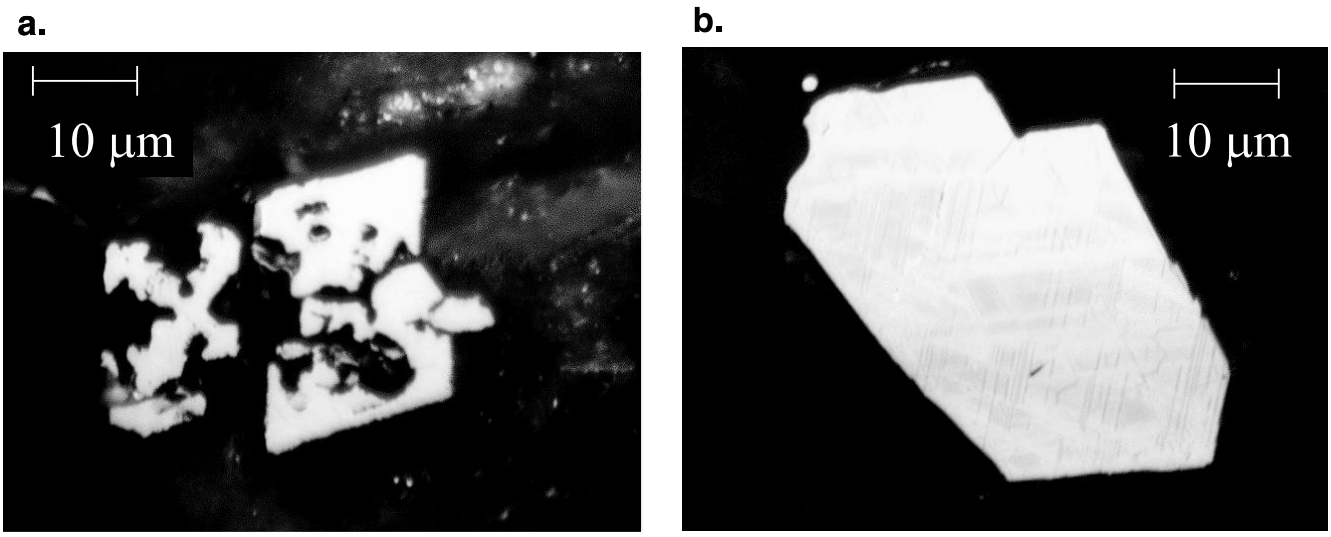

Figure 2.2: Thin section observations. a: sample 1203A, 47R4, 50-52cm. b: 1205A, 18R2, 16-18 cm.

show some important variations between flows, revealing differences in magnetic mineral concentration. Koenigsberger ratios are high (between 1.82 and 48.31), indicating that for most of the samples induced magnetization is not important in comparison with the NRM.

2.5.2 Thin-section observations and microprobe analysis

In order to help identify magnetic minerals, I selected eight samples for observations of thin sections in reflected light. Most of the sections contain large crystals, many of them being cracked. Some samples (1203A, 47R4, 50-52cm; 1204B, 13R3, 46-48 cm; 1205A, 35R4, 56-58 cm) include skeletal crystals which are characteristic of rapidly cooled titanomagnetite or titanomaghemite (Fig. 2.2a). This is expected for two of these samples because of their low unblocking temperatures, but quite surprising for the other sample, which has a high Curie point. I observed ilmenite exsolution in a few samples (1203A, 47R4, 50-52 cm; 1205A, 18R2, 16-18 cm; 1205A, 33R3, 30-32 cm; 1205A, 35R4, 56-58 cm) indicating high-temperature oxidation (Fig. 2.2b.). The two thin sections from Hole 1206 (1206A, 22R1, 127-129 cm 1 and 1206A, 41R1, 35-37 cm) are characterized by very small grains. In 7 out of the 8 samples, I could identify two or more phases, meaning that more than one magnetic mineral is present.

Two sections out of the eight correspond to samples that were so far considered as providing reliable results. The first one is 1205A,18R2,16-18cm (Fig. 2.2b). In the thin section, the crystals appear to be smaller than in other sections. The second one is 1206A,22R1,127-129cm. The very small grain size observed in the thin section is consistent with the narrow distribution of unblocking temperatures.

I carried out electron microprobe analysis on the same samples used for thin section observations. In all the samples, Mg, Al and Si are present as impurities. Sample 1205A, 18R2, 16-18 cm has two magnetic phases: one contains almost no titanium and the other one has an ulvospinel fraction x around 0.55. One sample from the 1205A, 33R lava flow has little or no titanium at all. One sample from the 1206A, 22R lava flow contains a significant amount of chromite as well as some titanium, but the chromite is probably not magnetic. One sample from Hole 1206 (in a lava flow where none of the paleointensity results are reliable) again shows no Ti and is almost pure magnetite.

I also did microprobe analysis on a few samples that failed the paleointensity experiment. The magnetic mineral composition ranges from Ti-free magnetite (or maghemite) to titanomagnetite (or titanomaghemite) with x around 0.6.

2.5.3 Thermomagnetic curves

High-field thermomagnetic curves were measured in air at the Institute for Rock Magnetism, University of Minnesota, using a vibrating-sample magnetometer (μVSM). I observed four types of curves (Fig. 2.3). The first type (samples from flow 1205A, 27R4) is characteristic of moderately oxidized titanomagnetite with a "virtual" Curie temperature of about 260°C (Fig. 2.3a). It is difficult to determine the Curie point from the $M_s - T$ curve because the inversion starts before the Curie temperature of the original titanomaghemite is reached. For this reason, the Curie temperatures are estimated by extrapolation of the curve before inversion begins. The ulvospinel fraction, x, is about 0.5 for this group of samples, estimated by comparing T_C with the data of Hunt et al. (1995). Further heating above 300°C resulted in an increase in magnetization to a peak at temperatures of about 400°C, indicating inversion to an unstable multiphase intergrowth (Özdemir & O'Reilly, 1982). On cooling, this product inverts to a stable final product with a Curie temperature of 530°C. Inversion of

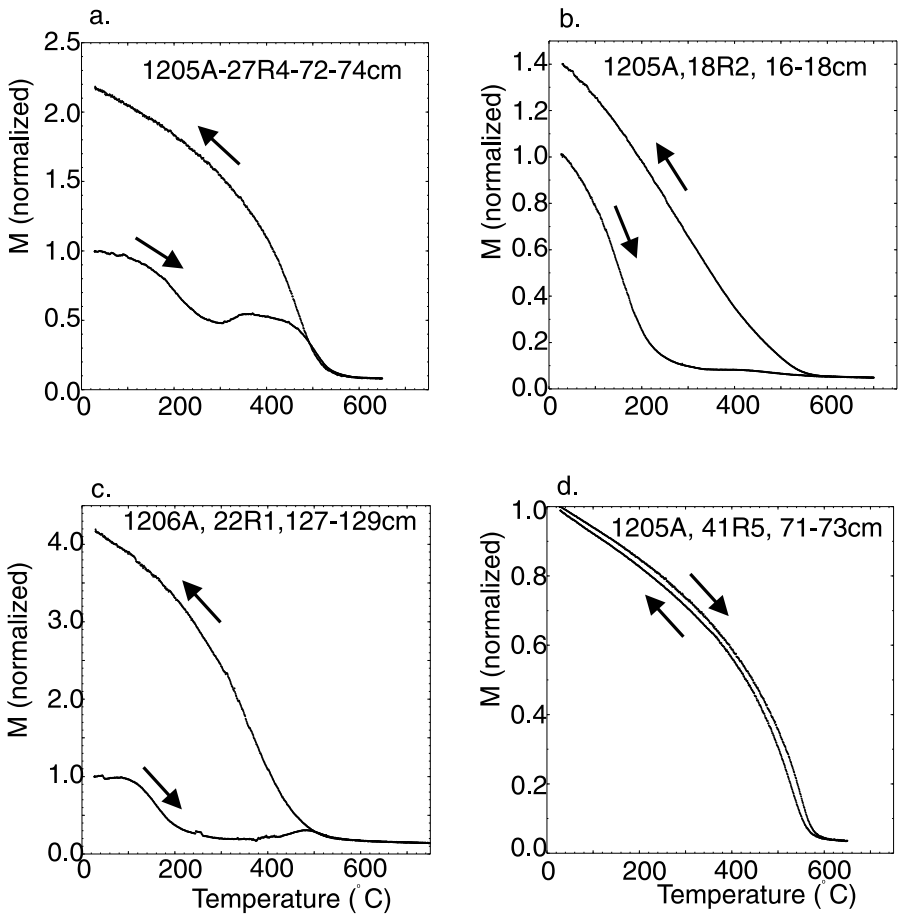

Figure 2.3: Strong-field thermomagnetic curves for four different types of behaviour.

titanomaghemite therefore takes place in two stages (Özdemir, 1987). The saturation magnetization of the final assemblage is twice as high as that of the starting titanomaghemite.

The second type of thermomagnetic behaviour occurs in less oxidized titanomagnetites (1203A, 49R3, 79-81 cm and 1205A, 18R2, 16-18 cm) with a lower Curie temperature of 240°C (Fig. 2.3b). Such a Curie temperature corresponds to an x value around 0.45 (Hunt et al., 1995). Further heating above 250°C results in an inversion. The final product with a T_C of about 500°C has a stronger M_s than that of the original titanomaghemite.

The third type of $M_s - T$ curve is characteristic of less oxidized titanomagnetites with low Curie temperatures between 160 and 170°C (x values between 0.55 and 0.6). A typical thermomagnetic curve for this group (all the samples from Hole 1206) is shown in Figure 2.3c. The first-stage inversion is accompanied by a slight increase in magnetization at about 450°C.

On cooling, this product inverts to a final stable product with T_C=510°C. The saturation magnetization of this iron-rich product is almost four times higher than that of the starting titanomaghemite.

The last type of thermomagnetic curves is characteristic of titanium-poor and iron-rich titanomagnetites (Fig. 2.3d). Samples in this group have reversible $M_S(T)$ curves with a Curie temperature of 570°C, indicating a composition very close to magnetite ($x = 0.03$).

2.5.4 Hysteresis parameters

I measured room-temperature hysteresis parameters using a VSM at the Institute for Rock Magnetism. The results for the accepted samples of Table 2.1 are listed in Table 2.3. According to the criteria defined by Day et al. (1977), samples from Holes 1203 and 1205 fall in the PSD category, whereas samples from Hole 1206 fall in the SD category.

2.5.5 Low-temperature measurements

Low-temperature remanence measurements were made with an MPMS-2 SQUID magnetometer at the Institute for Rock Magnetism. First, samples were given a saturation isothermal remanent magnetization (SIRM) in a field of 2.5 T at 20 K and then warmed in zero field to 300 K. I also measured isothermal remanence cooling and warming curves. A new SIRM was produced by applying a 2.5 T field at room temperature, then cooled to 20 K and back to 300 K in zero field. Low-temperature remanence curves were measured on basalt samples that were successful in the paleointensity measurements.

The SIRM warming and SIRM cooling/warming curves for sample 1205A, 41R5, 71-73 cm are shown in Figure 2.4a (type 1). The SIRM decay curve shows a sharp decrease between 20 and 50 K. In further heating above 70K, the remanence decreases steadily with temperature. The broad remanence transition between 80 and 120 K is probably due to a small amount of titanium and other non-magnetic impurities such as Al^{3+} or Mg^{2+}. The composition of this sample is very close to magnetite, with a T_C of 570°C and x value of 0.03 based on the thermomagnetic analysis (Fig 2.3d). Therefore the broad remanence transition represents the Verwey transition of magnetite with impurities (Özdemir et al., 1993). SIRM cooling

Table 2.3: Magnetic properties of the accepted samples. Samples with an asterisk are from the second set. Underlined samples are the samples that did not show evidence of maghemitization. LT: low-temperature memory; M_{rs}/M_s: ratio of the saturation remanent magnetization over the saturation magnetization; H_c: coercive field; H_{cr}: remanent coercive field; Q_n: Koenigsberger ratio. Numbers in parentheses next to the Curie temperature and to the low-temperature memory correspond to the type of thermomagnetic curve and low-temperature behavior, respectively, as defined in the text.

Sample	$T_C(^o)$	LT (%)	M_{rs}/Ms	$H_c(mT)$	$H_{cr}(mT)$	H_{cr}/H_c	Q_n
1203A-49R-3, 79-81 cm	206 (2)	79 (3)	0.105	4.8	8.2	1.71	7.2
1205A-18R-2, 16-18 cm	220 (2)	56 (1)	0.287	32.1	47.0	1.46	4.3
1205A-27R-4. 60-62 cm*		81 (2)	0.196	8.5	14.3	1.68	2.33
1205A-27R-4, 72-74 cm*	253 (1)	84 (2)	0.211	8.0	10.2	1.28	2.51
1205A-27R-4, 97-99 cm		86 (2)	0.158	6.3	8.8	1.40	4.1
1205A-33R-2, 94-96 cm	579 (4)	72 (1)	0.315	30.3	41.3	1.36	8.3
1205A-33R-3, 87-89 cm	560 (4)	79 (2)	0.238	9.7	12.7	1.31	5.3
1205A-41R-5, 51-53 cm*		59 (1)	0.186	19.7	36.1	1.83	14.2
1205A-41R-5, 55-57 cm	592 (4)	58 (1)	0.224	22.7	43.1	1.90	9.6
1205A-41R-5, 66-68 cm	582 (4)	62 (1)	0.205	21.6	39.6	1.83	9.0
1205A-41R-5, 71-73 cm*	575 (4)	60 (1)	0.172	20.5	38.6	1.88	22.6
1206A-22R-1, 127-129 cm	195 (3)	96 (4)	0.612	66.6	68.0	1.02	20.0
1206A-22R-2, 31-33 cm	170 (3)	97 (4)	0.482	31.2	29.9	0.96	48.3
1206A-22R-2, 3-5 cm		93 (4)	0.572	43.8	48.2	1.10	36.1
1206A-32R-2, 117-119 cm		94 (4)	0.566	65.4	26.3	0.40	11.3
1206A-32R-2, 128-130 cm		97 (4)	0.547	56.3	53.1	0.95	16.2
1206A-33R-1, 45-47 cm*		94 (4)	0.495	19.6	20.4	1.04	28.8

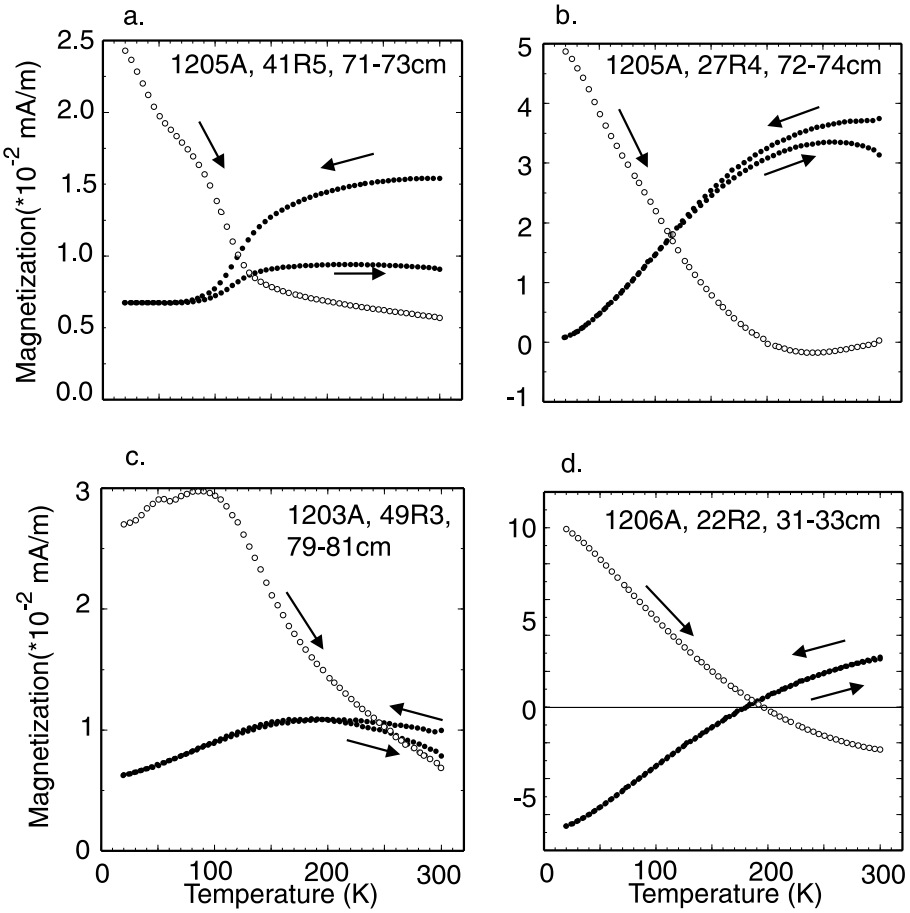

Figure 2.4: Temperature dependence of saturation remanence (SIRM) produced by a 2.5 T field. The open circles show the zero-field SIRM warming curve from 20 K to 300 K. The closed circles show the zero-field cooling (300 K to 20 K) and warming curves for SIRM produced at 300 K.

and warming curves for the same sample are shown in Fig. 2.4a. The remanence decreased with cooling to 80 K and was temperature independent between 80 and 20 K. In warming from 20 to 80 K, the behaviour was completely reversible, but above 90 K, the remanence did not retrace the cooling curve but increased only slightly. The remanence curves for the other samples from this lava flow are very similar to those of Fig. 2.4a. The SIRM memories (percentage of remanence remaining after low-temperature cycling) are between 59 and 62%.

Representative low-temperature remanence curves for sample 1205A,27R4, 72-74 cm are shown in Figure 2.4b (type 2). The low-temperature SIRM decreased almost linearly with increasing temperature between 20 and 200 K, then increased slightly with further warming

to 300 K. In cooling from 300 K to 20 K, the room-temperature SIRM decreased steadily. As the sample was warmed from 20 K, the remanence traced the cooling curve between 20 and 150 K. At room temperature 15% of the initial SIRM was demagnetized. The thermomagnetic behaviour of this sample is characteristic of medium-oxidized titanomagnetite with x between 0.45 and 0.5 (Fig. 2.3a).

The isothermal remanence warming curve for sample 1203A, 49R3, 79-81 cm (the only successful sample from Hole 1203) exhibits a broad peak between 40 and 120 K and then decreases with increasing temperature (Fig. 2.4c) (type 3). The shape of the SIRM demagnetization curve is very similar to that of synthetic titanomagnetite of composition x=0.6 (Moskowitz et al., 1998). The room-temperature SIRM cooling curve for this sample is almost temperature independent, increasing slightly between 300 and 150 K. In further cooling to 20 K, the remanence dropped to 60% of the original SIRM. The remanence retraces the cooling curve in warming from 20 K to 200 K, then decreases with further warming to room temperature. About 80% of the original SIRM remains at 300 K.

Samples from Hole 1206 show interesting low-temperature behaviour (type 4). The SIRM decreases steadily with warming between 20 and 170 K. At 170 K the remanence becomes zero and changes its sign. In further warming above 170 K, SIRM is negative and continues to decrease. In cooling from 300 K, the room-temperature SIRM decreases, passes through zero at 170 K and changes sign. The remanence decreases steadily with cooling to 20 K. As the sample is warmed from 20 K, the remanence retraces the cooling curve. The thermomagnetic analysis for this sample indicates the presence of titanomaghemite with a low T_C=160°C and an ulvospinel ratio of x= 0.6 (Fig. 2.3c). This self-reversal of magnetization below room temperature has been observed in other samples from the same hole (M. Torii, *pers. comm.*), and in other studies of oceanic basalts (e.g. Matzka et al., 2003). It is probably caused by the presence of N-type ferromagnetism in titanomaghemite.

2.5.6 Final results

Samples showing evidence of maghemitization are unsuitable for paleointensity determination as the replacement of TRM by a CRM of reduced intensity will yield low paleointensity values. Based on the rock magnetic properties detailed above, we can now eliminate from

the final list of samples giving a reliable result: 1203A, 49R3, 79-81 cm; 1205A-18R-2, 16-18 cm; 1205A, 27R4, 60-62 cm; 1205A, 27R4, 72-74 cm; 1205A, 27R4, 97-99 cm; 1205A, 33R3, 87-89 cm and all the samples from Hole 1206. For all of these samples, the bulk susceptibility variations with heating temperature show important increases with heating, corresponding to the inversion of (titano)maghemite to magnetite. In the end, only four samples remain as truly reliable results.

Submarine basalts are likely to be subject to shape anisotropy because they usually have high susceptibility and high NRM values. In strongly magnetized lava flows, topographic irregularities create magnetic terrain effects (Baag et al., 1995). The effect of shape anisotropy created by the shape of the cooling unit on inclination values has been discussed by Coe (1979). Dunlop and Zinn (1980) discussed the effect of shape anisotropy on paleointensity values. The method usually used to correct the paleointensity values for anisotropy effects is to use the anisotropy of anhysteretic remanent magnetization (AARM) (Selkin et al., 2000). However, in my case an experimental determination of the anisotropy effects was not possible because all the samples were altered after the repeated heatings. The magnetic material present at the end of the paleointensity experiment is completely different from the original carrier of the magnetization. The only way to have an estimate of the shape anisotropy in this case was by using theoretical calculations. I can calculate how much the paleointensity deviation would be by assuming that the lava flows have the shape of thin, infinite sheets. This will give an upper limit on the anisotropy effect.

The inclination deviation assuming a thin sheet (Coe, 1979) is:

$$tanI_i = tanI_0 \times \frac{1}{k} \times (1 - exp(\frac{-k}{1+\chi})), \tag{2.2}$$

where I_0 is the "true" inclination, i.e. the inclination assuming a spherical shape, I_i is the inclination assuming a thin sheet shape (i.e. the measured inclination), and χ=k/Q, with k being the intrinsic susceptibility and Q is the Koenigsberger ratio.

The intrinsic susceptibility can be calculated by (Coe, 1979):

$$k = ln(\frac{F}{F - J.N}) \times \frac{1}{N} \times \frac{1}{1 - ln(\frac{F}{F-J.N}) \times \frac{1}{Q}}, \tag{2.3}$$

where F is the ancient field measured, J is the intensity of NRM and N is the demagnetizing

Table 2.4: Calculated effect of anisotropy on inclinations and paleointensities. Symbols are defined in the text. Samples with an asterisk are from the second set.

Sample	$I_i(^o)$	$I_0(^o)$	$T_i(\mu T)$	$T_0(\mu T)$	difference
1205A-41R-5, 51-53 cm*	-45.9	-53.6	31.2	36.6	12%
1205A-41R-5, 55-57 cm	-44.0	-47.3	34.8	36.9	11%
1205A-41R-5, 66-68 cm	-44.5	-50.9	31.6	36.6	7%
1205A-41R-5, 95-97 cm*	-43.0	-48.4	31.1	34.2	7%

factor.

"True" inclinations are shallowed by 3 to 8° compared to the inclinations measured, assuming that the lava flows are thin, infinite sheets.

Now I can calculate the paleointensity deviation: if T_i is the field recorded in the presence of the demagnetizing effect, i.e. the measured paleointensity,

$$H_0 = H_i = T_i \times cosI_i \tag{2.4}$$

$$Z_0 = H_0 \times tanI_0 \tag{2.5}$$

$$T_0 = \sqrt{H_0^2 + Z_0^2} \tag{2.6}$$

with H_0, Z_0 and T_0 being the tangential (vertical), normal (horizontal), and total "true" fields respectively.

Paleointensities are increased by 5-10% when I correct for the anisotropy effect. Results are summarized in Table 2.4. The four remaining results show a very good consistency. Paleointensities are between 34.2 and 36.9 μT. The mean paleointensity for this lava flow is 35.8$\pm$0.6 μT.

2.6 Discussion

The main problem in using submarine basalts for paleointensity experiments is low-temperature oxidation of the titanomagnetites, which replaces TRM by CRM and results in too low paleointensities. All the results that were considered reliable before thermomagnetic curves

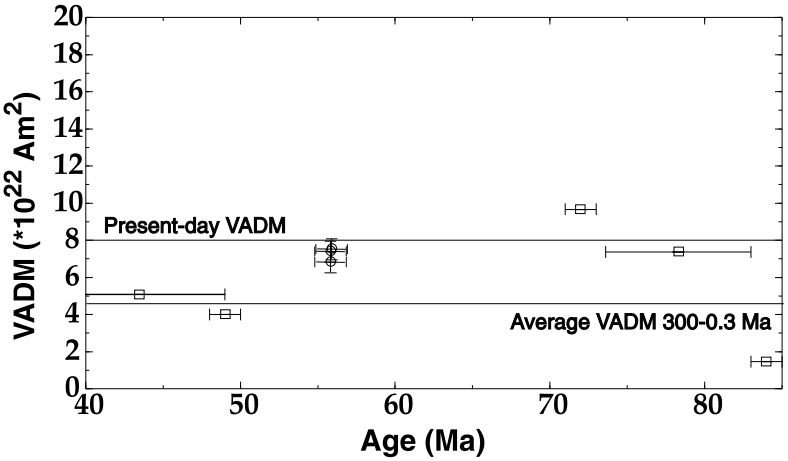

Figure 2.5: Comparison of my VADM values (circles) with VADM values from the Scripps submarine basaltic glass database (squares). My VADM values were calculated using the corrected paleointensities.

were measured but that did show evidence of maghemitization were extremely low, between 5 and 25 μT, which is 1.5 to 7 times smaller than the paleointensities obtained from the non-maghemitized lava flow. This is in agreement with most other studies of paleointensities with sub-oceanic basalts (for instance Grommé et al. (1979) with basalts from the Juan de Fuca Ridge or Carmichael (1977) with basalts from the Mid-Atlantic Ridge). Out of thirteen lava flows sampled on three seamounts, only one (unit 26A of Tarduno et al. (2002)) had not undergone low-temperature oxidation.

I calculated the virtual axial dipole moments (VADMs) associated with our paleointensity values in order to compare them with VADMs measured on basaltic glass samples (Selkin & Tauxe, 2002) (Fig. 2.5). There are only five points in the time range 40-85 Ma. They are fairly dispersed, but all but one are less than the present-day VADM. VADMs are calculated from:

$$VADM = \frac{4\pi}{\mu_0} \frac{R^3 H_a}{\sqrt{1+3cos^2\theta}} \tag{2.7}$$

where μ_0=$4\pi \times 10^{-7}$, R is the radius of the Earth, H_a is the paleofield intensity and θ is the magnetic paleocolatitude calculated from the AF demagnetization (62.9^o). This value is more appropriate than geographic paleocolatitude derived from plate reconstructions which

are based on a fixed hotspot hypothesis.

The average of the four good samples is $(7.3\pm0.1)\times10^{22}$ Am^2. Our data are within the error bars of the average VADM from 0.3 to 300 Ma ($4.6\pm3.2\times10^{22}$ Am^2) calculated by Selkin & Tauxe (2000) using data from basaltic glass but are higher than the average value. It should be kept in mind however that most VADM calculations are based on plate reconstructions which assume fixed hotspots. My data add important VADM values at 56 Ma in a previously unstudied time interval. The trend of VADMs shows low values up to 50 Ma, then an increase up to 8×10^{22} Am^2 sometime between 50 and 56 Ma. However, I have too few data to advance any conclusions on the geodynamo regime in this time range.

Chapter 3

Modelling of FORC diagrams for SD and PSD magnetite

Most of Chapter 3 has been published as: Claire Carvallo, Adrian R. Muxworthy, David J. Dunlop, Wyn Williams, Micromagnetic modelling of first-order reversal curve (FORC) diagrams for single-domain and pseudo-single-domain magnetite, *Earth Planet. Sci. Lett.*, **213**, 375-390, 2003.

3.1 Introduction- Test of the model

As explained in §1.2.1, FORC diagrams are becoming more and more used to determine the grain size distribution and interaction state in natural samples. If the FORC technique is to become widely accepted, it is important for it to be thoroughly understood. In this chapter I use for the first time micromagnetic modelling to predict the theoretical FORC distributions of SD to small PSD grains, as well as arrays of SD particles. In sediments and igneous rocks, the magnetic properties are often controlled by magnetite (Fe_3O_4) because of its frequent occurence and because the magnetization of magnetite is stronger than that of other magnetic minerals. This is why I model a magnetite-like mineral.

The partial hysteresis process is modelled by saturating the grain with an appropriate positive field. The field is then decreased in 2 mT steps until it reaches saturation in a negative field. An equilibrium state is found at each field. FORCs are modelled by starting

from each state obtained on the initial descending hysteresis curve and increasing the field back to positive saturation. The field increment is also 2 mT. This increment was chosen so that the total number of FORCs is around 100, a number usually accepted as large enough to obtain a good quality FORC diagram (Roberts et al, 2000; Pike et al., 1999). In order to avoid marginally stable states, I introduce perturbations of 5^o or less to each dipole and re-run the minimization until the energy difference between two successive minimizations normalized to the single domain energy is less than 10^{-3}. I tested the effect of varying these two minimization parameters (perturbations between 3 and 8^o and energy differences between 10^{-2} and 10^{-4}). The micromagnetic states are not affected by these changes, although the fields at which switching occurs vary between 2 and 4 mT.

It is important to note that a number of simplifications have been made in the model to make the computation feasible. I have neglected thermal fluctuations and any mineral microstructure, and have assumed a very simple grain geometry. My goal in this study is to examine the trends of hysteresis properties and I make no claim that the coercivities or remanences would be a good match for realistic grain geometries. What is intended is that some insight should be gained as to the effects of grain interactions and domain states on the trends observed in FORC analysis.

It is possible to test the model using "standard problem #1" proposed by the micromagnetic modeling activity group (μMAG) at the NIST Center for Theoretical and Computational Material Science (CTCMS; website: www.ctcms.nist.gov/ rdm/mumag.org.html). The standard problems allow researchers to compare computational techniques and identify problems. The goal of standard problem #1 is to calculate the hysteresis loop for a thin sheet of permalloy (1000×2000×20 nm). The material parameters are: A= 1.3×10^{-11} J/m, M_S=8.0×10^5 A/m, K=5.0×10^2 J/m^3. The anisotropy is uniaxial, with easy axis parallel to the long edges of the rectangle. The solutions submitted so far show some discrepancy: when the field is applied along the short axis, coercivities vary between about 1 and 12 mT. This is not suprising however, because these solutions cover a huge range of model types: most of the solutions are for 2-dimensional grids with 2-dimensional magnetization spins. Some are 3D spins, some are 3D grids.

My model is not optimized for two-dimensional problems, so I used a resolution of

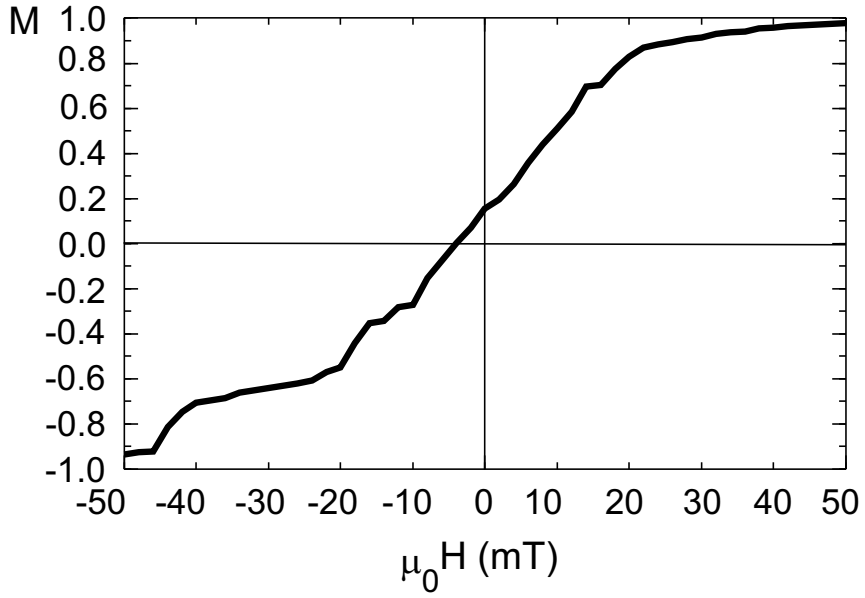

Figure 3.1: Half major hysteresis loop for my solution to the permalloy thin sheet micromagnetic problem #1 . The field is along the short axis of the sheet.

50×25×1 cells, smaller than what is ideally required by the exchange length of permalloy. Therefore, I also had to increase the thickness of the permalloy sheet from 20 nm to 40 nm. Nevertheless, I find a coercivity of 4.1 mT when the external field is applied along the short axis of the sheet (Fig. 3.1), which is consistent with some of the submitted solutions for this problem (e.g. ts96b, H_C=5.3 mT; pb97, H_C=4.9 mT; solutions available at: www.ctcms.nist.gov/ rdm/std1/prob1report.html).

3.2 Hysteresis and FORC diagrams of isolated grains as a function of size

3.2.1 Single field orientation

In an elongated grain of magnetite, the easy axis of magnetization is along the direction of elongation and the hard axes are along two directions perpendicular to the easy axis. It is considerably more difficult to saturate the magnetization of a magnetite crystal along the

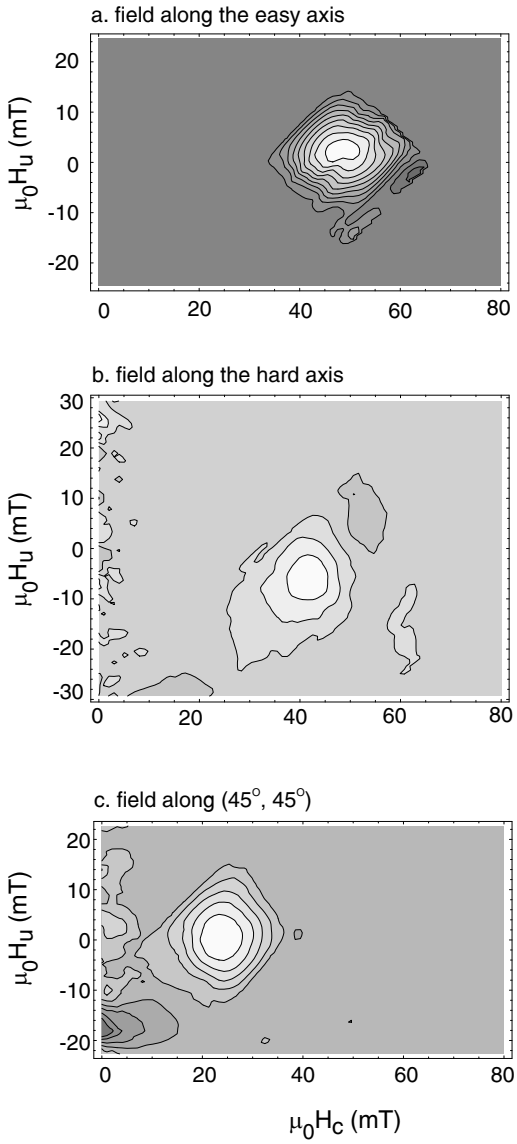

Figure 3.2: FORC diagrams for an isolated elongated SD grain (grain size 0.045×0.03×0.03 μm, elongation ratio 1.5). (a) Field oriented along the easy axis; (b) field oriented along the hard axis; (c) field oriented at 45° to the easy axis axis. SF=5.

hard direction than along the easy direction, and therefore I expect the hysteresis curves and the FORC diagrams to be different depending on the field orientation.

Micromagnetically calculated FORC diagrams are shown in Figure 3.2 for an SD particle with the field applied along an easy axis, a hard axis, and an intermediate direction. The particle size is 0.045×0.03×0.03 μm, i.e., an aspect ratio of 1.5.

I obtained rectangular hysteresis loops for SD particles if the field was applied along the easy axis. If the field was applied along the hard axis, the magnetization rotated reversibly at all fields. In both cases, the magnetization reversed by coherent rotation. This behavior is consistent with results from other studies (Stoner & Wolfarth, 1948; Virdee, 1999; Williams & Dunlop, 1995; Williams & Wright, 1997). If the field was applied at nearly 45° to the easy axis, the hysteresis showed a combination of reversible and irreversible behavior. The coercive force in this case was approximately half the coercive force for the field along the easy axis, as predicted by Stoner & Wohlfarth (1948).

In the two cases where there is hysteresis, ideally the FORC diagram would display a delta peak at the coercive field H_c with no spread in the H_u direction (zero interaction field in the Preisach-Néel interpretation). In reality, the peak has a finite width due to the fitting of a polynomial function and to the spread of coercivities on the reversal loops caused by perturbations introduced in the minimization process (Pike et al., 2000)(2 to 4 mT). For all the following models of isolated particles, I use the intermediate field orientation at 45° to the easy axis.

When the grain size is increased just above the SD-PSD limit to a 0.10×0.08×0.08 μm grain (q=1.25), the magnetization reverses during the major hysteresis loop through a vortex state which is stable for applied fields between –10 and –26 mT. Nucleation of the vortex is progressive. The initial state is a flower state (Fig. 3.3a), i.e., a SD state with fanning of the magnetization from the uniform state near the grain surface. The next state (Fig. 3.3b) is a precursor to a vortex state, which collapses to a well-defined vortex state on relaxation of the applied field (Fig. 3.3c). Such behavior has been described by Enkin et al. (1994) while modelling PSD magnetite grains. The vortex exits at one of the corners through the same intermediate state previously described (Fig. 3.3d) and the structure becomes a flower state in the negative saturation field (Fig. 3.3e).

Secondary branches appear in the reversal curves when the fields are in the range of any of the intermediate states between the two flower states (Fig. 3.4a) (Newell & Merrill, 2000). This causes the main peak on the FORC diagram to split into several positive and negative peaks (Fig. 3.4b).

Although I tried to minimize instabilities as much as possible, switching to a vortex state

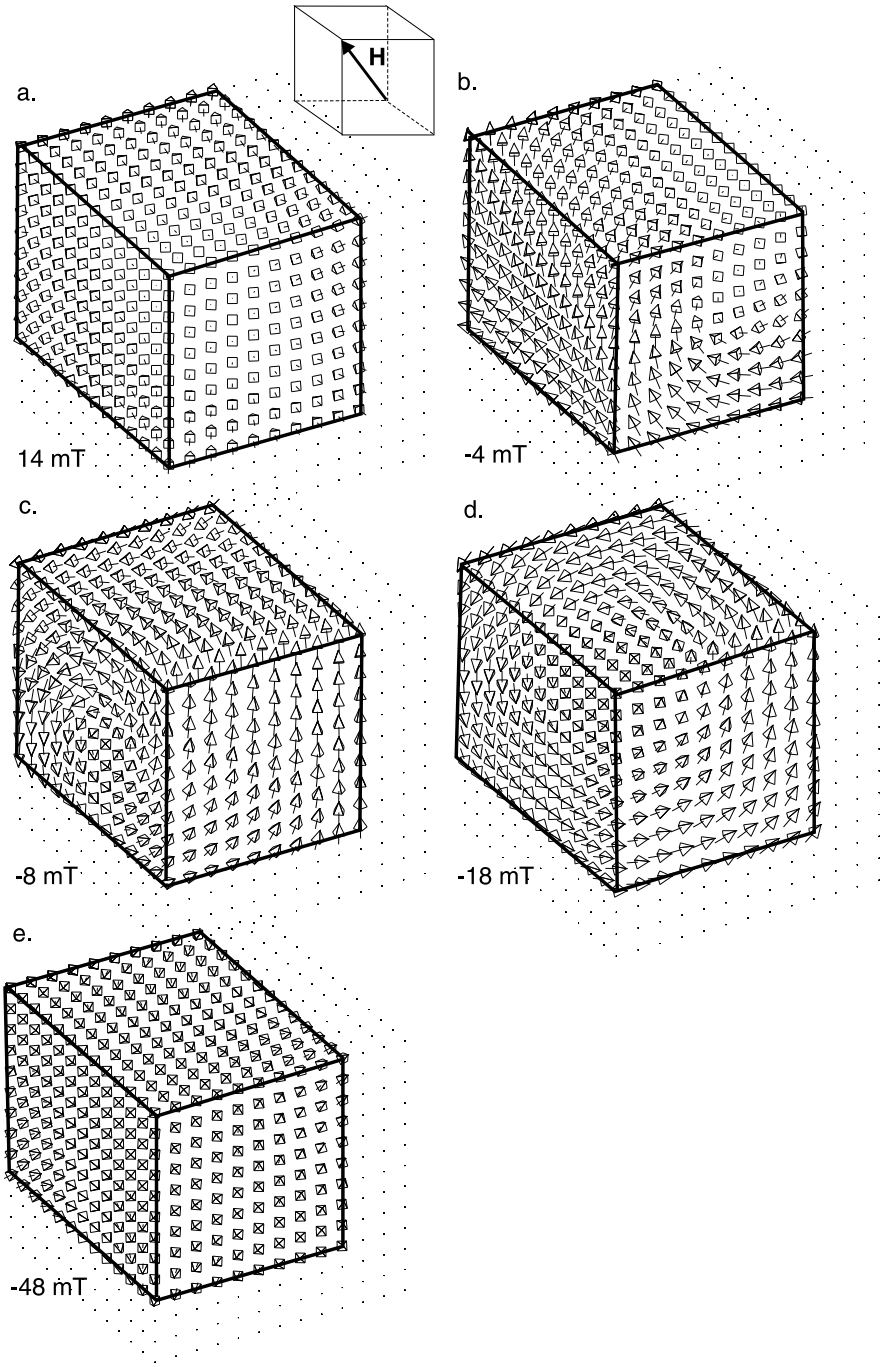

Figure 3.3: Micromagnetic structure obtained during a complete hysteresis loop for a 0.10×0.08×0.08 μm isolated particle. (a) applied field is 14 mT; (b) applied field is -4 mT; (c) applied field is -8 mT; (d) applied field is -18 mT; (e) applied field is -48 mT. Arrows represented by a cross inside a square are pointing out of the page; arrows with a dot inside a square are pointing into the page.

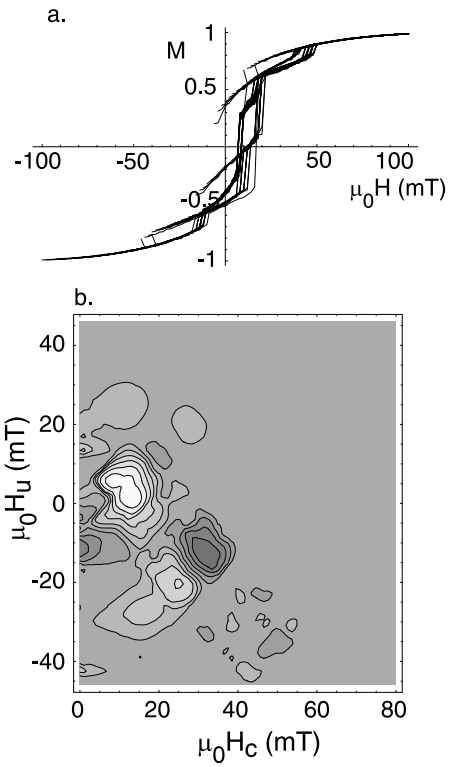

Figure 3.4: Hysteresis loop with reversal curves (a) and FORC diagram (b) of an isolated elongated PSD grain (grain size 0.10×0.08×0.08 μm). The field is oriented at 45° to the easy axis. SF=5.

or to a flower state does not occur at exactly the same field for all the reversal curves. In some cases, the micromagnetic state does not pass through the vortex state but flips directly to the flower state. As a result, smaller secondary peaks appear on the FORC diagram and the peaks are relatively spread out (Fig. 3.4b). The ∼45° line of alternating positive and negative peaks is due to the perturbations introduced in the model to test the stability: this causes the Barkhausen jumps to occur at different fields on each reversal curve. The same pattern has been observed by C.R. Pike (pers. comm.) in pyrrhotite single grains.

For a somewhat larger grain (0.12×0.09×0.09 μm), the intermediate states encountered during the magnetization reversal are more numerous and complex, leading to a large number of different reversal curves and peaks on the FORC diagram.

3.2.2 SD grains oriented in different directions

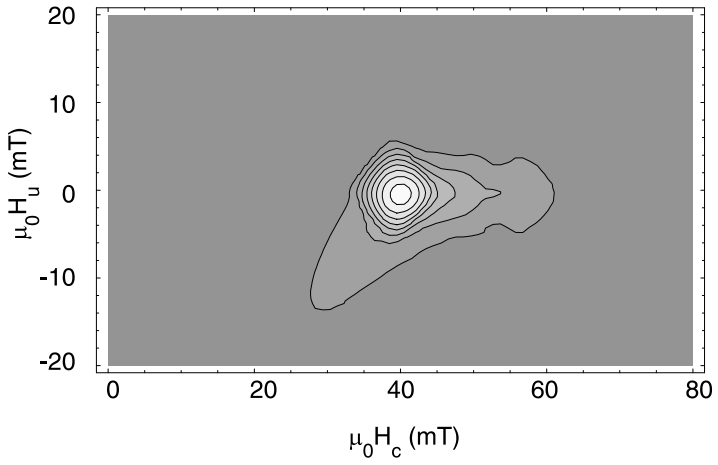

Figure 3.5: Average of 100 FORC diagrams of isolated elongated SD grains (grain size 0.045×0.03×0.03 μm, elongation ratio 1.5), with the applied field oriented along 100 different randomly chosen directions. SF=3.

In order to reproduce the distribution of orientations of the grains in a natural sample, I averaged FORC distributions for a set of 100 random field orientations. The particle size is 0.045×0.03×0.03 μm. The FORC distribution is now more spread out on the H_c axis than on the H_u axis (Fig. 3.5). I would expect the FORC diagram to be elongated along the H_c axis because particles with different orientations have different coercive fields. Again, the spread on the interaction axis is due to the averaging effect of the smoothing factor and to the perturbations introduced during the minimization process. The "boomerang shape" may be an effect of different return paths of the FORCs. If H_a is a saturating field then the FORCs are identical. However, if H_a is not a saturating field, then the return curves for randomly oriented grains display a dependence on H_a at relatively large positive fields, resulting in the asymmetry along the H_u=0 axis. This asymmetrical feature may be a result of the asymmetry of the FORC determination process itself. Such asymmetrical patterns are present on many measured and modelled FORC diagrams.

3.3 Hysteresis and FORC diagrams of 3D arrays: effect of interactions

Three-dimensional arrays of particles were modelled by masking some cells in a model consisting of a large number of cells. In so doing, it was possible to vary the size of the grains in the array as well as the spacing between the grains within the array. Based on micromagnetic calculations, grains interact significantly if the spacing between them is smaller than one grain width (Virdee, 1999; Muxworthy et al., 2003a). Modelling the effects of interactions on magnetic susceptibility in distributions of Stoner-Wohlfarth SD particles, Muxworthy (2001) found that the effect of interactions drops off when the spacing between grains is between one and two times the grain diameter. Modelling arrays of particles requires high resolution, so we restricted ourselves to arrays of 2×2×2 and 3×3×3 SD particles. A 2×2×2 array is physically somewhat unrealistic, but it allows us to gain some insight into interaction effects within the constraints of current computational resources.

3.3.1 Arrays of aligned particles

Arrays are formed of elongated particles aligned along the same direction (z-axis). The size of each SD particle within the array is 0.045×0.030×0.030 μm (q=1.5). The resolution of each individual grain is 3×2×2 cells. The spacing is defined as the distance corresponding to the free space between grains.

2×2×2 arrays

Hysteresis and reversal curves depend crucially on the spacing between grains. When the spacing between particles is twice the particle length or more, the micromagnetic structure is uniform and evolves toward a flower state as the field is decreased. Magnetic moments are aligned within one grain and with those of other grains. At a particular switching field, all the moments rotate coherently, then the structure again evolves toward a flower state where less and less deflection of the spins is observed at the corners as the field intensity increases. The FORC diagram is similar to that observed for a single crystal (Fig. 3.6a). It has a single

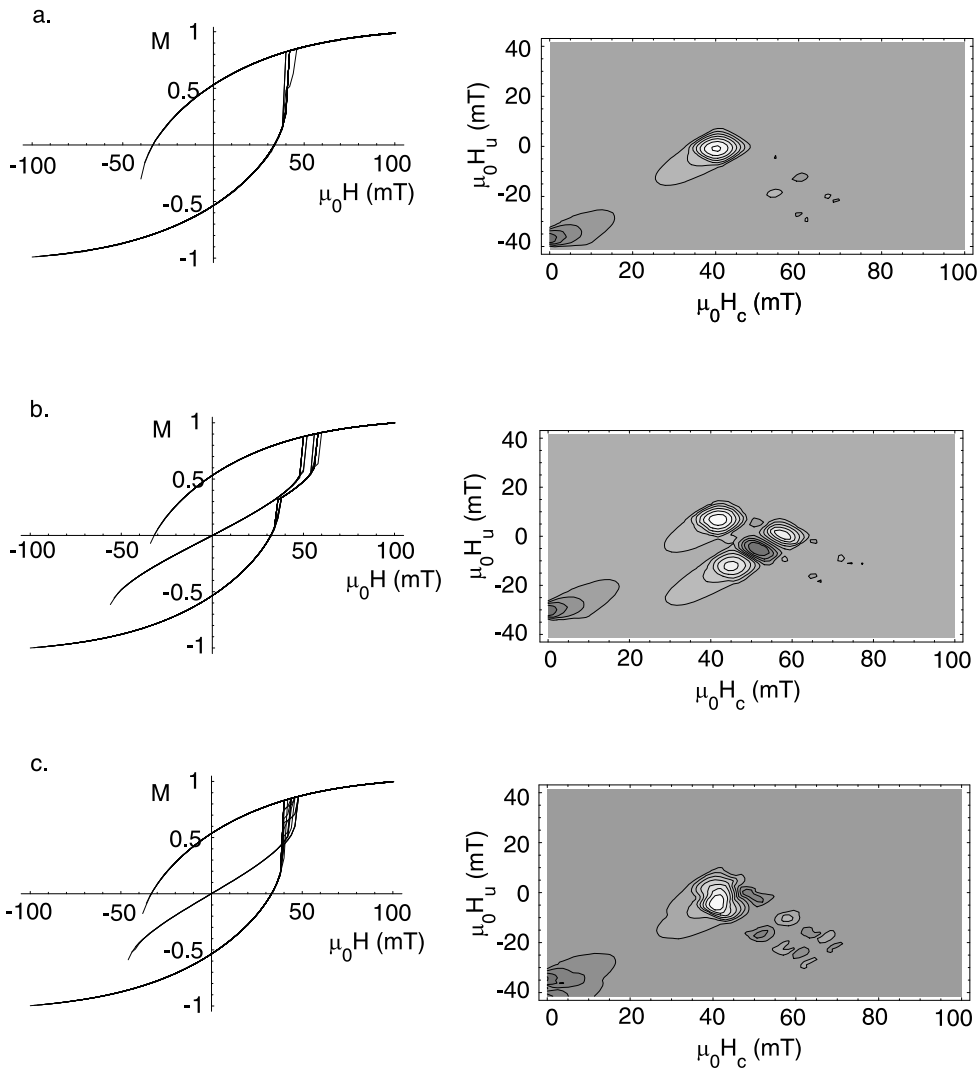

Figure 3.6: Hysteresis loops with reversal curves and FORC diagrams for an array of 2×2×2 elongated SD grains (grain size 0.045×0.03×0.03 μm, elongation ratio 1.5). The spacing between the different grains is: (a) twice the grain length; (b) two-thirds the grain length; (c) four-thirds the grain length. SF=4.

peak centered at zero interaction field and at the coercive field of the particle ensemble.

The hysteresis and micromagnetic structure of the array show some specific features when the spacing is reduced (Fig. 3.6b). First, the hysteresis loop exhibits two jumps when the field is decreased. The micromagnetic structure in the critical region of a reversal curve is shown in Figure 3.7. Between saturation and the first switching the grains have a uniform magnetization oriented in the direction of the field. Then, there is an intermediate state

(when the field is between 38 and 60 mT) where each grain still has a uniform magnetization, but where half of the grains have reversed their moments. Finally, all the moments switch again to a uniform state.

The presence of these two switching fields causes the hysteresis curve to show two discontinuities, as was found also by Virdee (1999). The reversal curves have different behavior depending on the reversal field H_a at which the curve begins. If H_a is larger than the first switching field, the reversal curve follows the same path as the hysteresis curve, and the structure stays as a flower state nearly up to saturation. If H_a is between the two switching fields, the reversal curve shows one jump at which the structure suddenly changes from a vortex state to a flower state, and then stays as a flower state. Finally, if H_a is less than the second switching field, the array undergoes either one or two switching events: the intermediate vortex is not always reached and if it is, only for a narrow range of fields (typically between 4 and 8 mT).

If the spacing is less than two-thirds the particle length, the intermediate state exists for a large range of fields (between 25 and 40 mT). The switching to the intermediate state or to the flower state on the reversal curve

happens at almost the same fields for all the different reversal curves (within 2-4 mT). As a result, the FORC diagram shows three distinct peaks corresponding to each switching: one for the switching from intermediate state to the flower state when H_a is in the range where the intermediate state is stable; one for the switching from flower state to intermediate state, plus one for the switching from the intermediate state to the flower state when H_a is beyond the range of stability of the intermediate state (Fig. 3.6b).

The range of stability of the intermediate state decreases when the spacing is increased. When the spacing is between two-thirds and twice the particle length, the intermediate state is only stable for a narrow range of fields: from 12 mT for a spacing of one particle length to 4 mT for a spacing of five-thirds the particle length. The switching does not occur at the same field for the different reversal fields, but over a range of about 8 mT. The two ranges of fields over which switching occurs overlap. This effect causes the peaks on the FORC diagram to become much noisier, and to eventually form only one peak (Fig. 3.6c). With the increasing variation of switching fields depending on the reversal fields we also

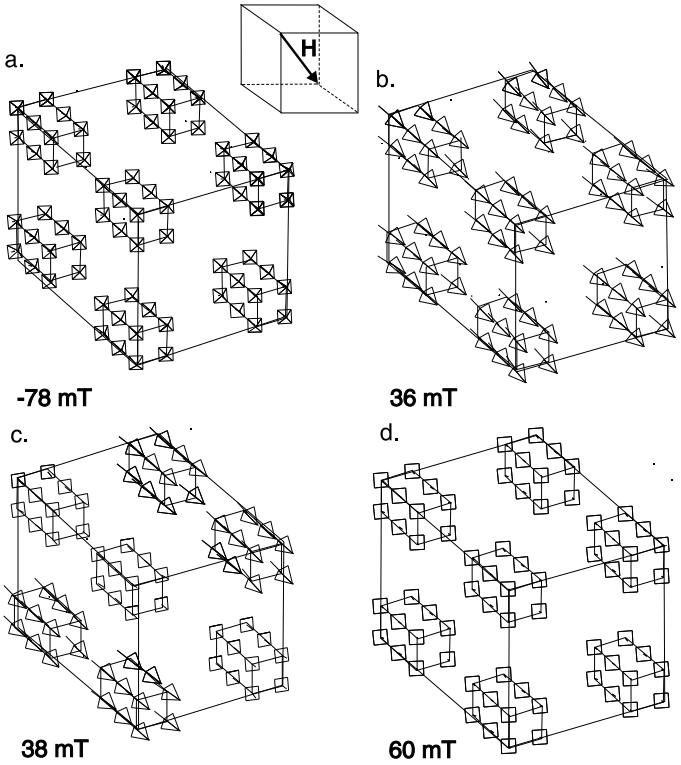

Figure 3.7: Micromagnetic structure of an array of 2×2×2 interacting elongated SD grains (grain size 0.045×0.03×0.03 μm, elongation ratio 1.5). The reversal field is -80 mT. (a, b): all the moments are still antiparallel to the field. (c) half of the moments have reversed. (d) all the moments are aligned with the field. Arrows represented by a cross inside a square are pointing out of the page; arrows with a dot inside a square are pointing into the page.

observe the appearance of a 45° line of alternating positive and negative peaks. When the intermediate state is stable over a range smaller than 4 mT, as is the case for a spacing of five-thirds the particle length, it is possible that this state would completely disappear when the minimization parameters are changed. In this case, the array would behave as a non-interacting ensemble. The critical spacing for the array to behave as a non-interacting array is between five-thirds and two particle lengths.

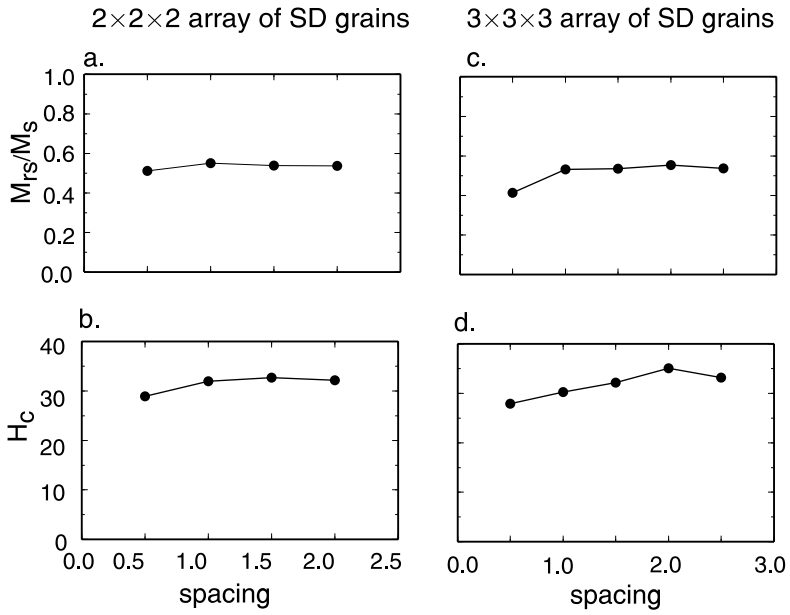

Figure 3.8: Hysteresis parameters as a function of spacing between particles for 2×2×2 (a, b) and 3×3×3 (c, d) arrays of elongated aligned SD particles. Spacing is in particle widths.

The ratio $M_{\rm rs}/M_{\rm s}$, which is traditionally used as an indicator of particle size, remains fairly constant when the spacing of the grains is changed (Fig. 3.8a). In particular, there is no obvious variation when the secondary branch disappears as a result of going from an interacting to a non-interacting system. The coercive field H_c is also fairly constant when the spacing of the grains varies (Fig. 3.8b). In this special grain arrangement, where all the grains are aligned, these two parameters would fail to indicate the interaction state of the system.

The effect of varying the spacing in an array of 2×2×2 grains is shown in Figure 3.9. There is a slight variation in coercivity depending on the spacing, but the main features on

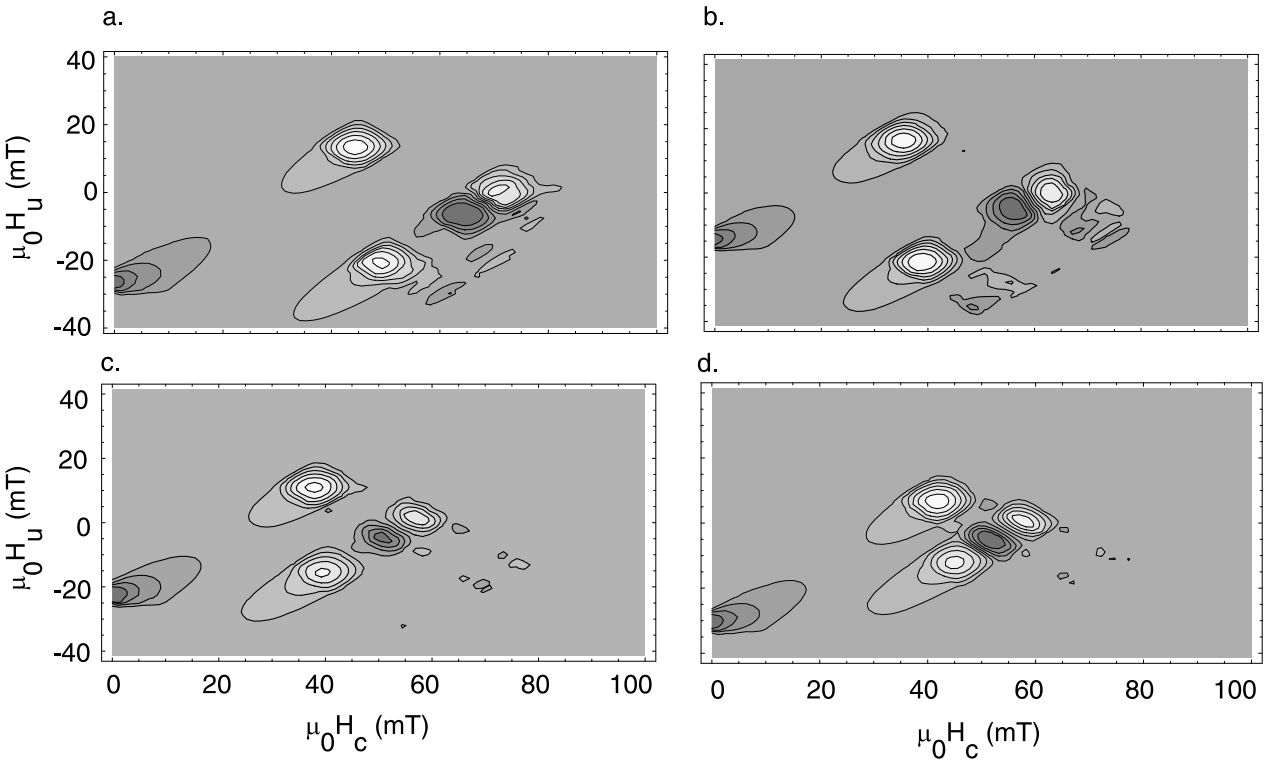

Figure 3.9: FORC diagrams for arrays of 2×2×2 particles with different sets of spacings between grains. Spacing between grains in terms of particle length are: (a): 1/3, 1/3, 1/3; (b): 1/3, 1/3, 2/3; (c): 1/3, 2/3, 2/3; (d): 2/3, 2/3, 2/3. SF=4.

the FORC diagram are still the same. In general, FORC diagrams for irregular arrays are intermediate between the FORC diagram for equally spaced arrays with separations equal to the largest and smallest separations in the irregular array, respectively.

3×3×3 array

Now, the model contains 27 elongated SD (0.045×0.03×0.03 μm) particles, arranged in a 3×3×3 array. We again found that there is a threshold in the spacing between cells that determines whether the grains are interacting (Fig. 3.10). The spacing has to be more than twice the grain length in order for the particles to behave like isolated grains (Fig. 3.10a): all the moments are aligned with the field at saturation, then the structure slowly evolves toward a flower state. All the moments reverse coherently at the same switching field. The reversal curves are either symmetrical with the main loop if the reversal field is smaller than

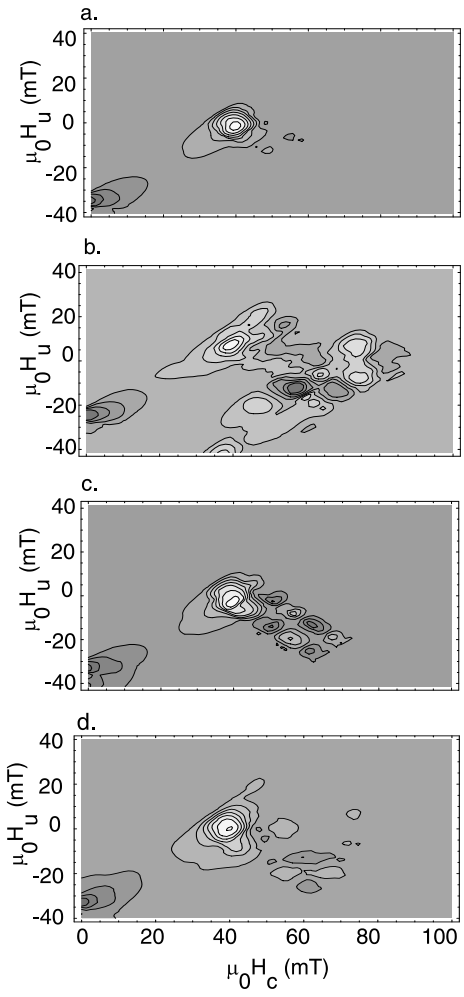

Figure 3.10: FORC diagram for an array of 3×3×3 elongated SD grains (grain size 0.045×0.03×0.03 μm, elongation ratio 1.5). The spacing between grains is: (a) 5/3 the grain length; (b) 1/3 the grain length; (c) 4/3 the grain length. (d) Average of FORCs for spacings of 1/3, 2/3, 1 and 4/3 the grain length. SF=4.

the switching field, or they follow the main loop if the reversal field H_a is larger than the switching field. This behavior results in a single peak on the FORC diagram.

If the spacing between grains is less than twice the grain length, intermediate states appear on the major hysteresis loop, leading to secondary branches on the reversal curves. The intermediate structures are now more complex than for the 2×2×2 array. Each jump in the hysteresis loop and the reversal curves corresponds to one or several of the grains reversing their magnetization, as shown by Pike and Fernandez (1999) (Fig. 3.11). In general,

the smaller the spacing, the more secondary branches appear. As for the 2×2×2 array, secondary branches give rise to several peaks on the FORC diagram (Fig. 3.10b). We can distinguish separated peaks up to a spacing of one particle length. When the spacing is between four-thirds and twice the particle length, the switching ranges all overlap on the reversal curves and it becomes difficult to judge if the secondary peaks are due to different switching fields because of different micromagnetic states on the reversal curve or to the range of fields over which switching occurs (Fig. 3.10c). These ranges are so small that, again, some states can disappear when varying the minimization parameters. In this case, we establish the critical spacing for the array to interact between four-thirds and twice the particle length.

In an attempt to simulate the effects of interactions in a random assemblage of particles in a real sample, we averaged the FORC diagrams obtained for interacting arrays of spacing 1/3, 2/3, 1, and 4/3 the grain length (Fig. 3.10d). One main peak emerges that is wider on the H_u axis than the peak observed in the non-interacting case (Fig. 3.10a.). This supports the idea that the spread on the H_u axis observed in interacting assemblages in natural samples might be due to a superposition of the secondary peaks we observed on very small arrays.

The full width at half maximum (FWHM) of the main peak of the cross-section taken in the H_u direction through the maximum of the FORC distribution is a measure of interaction in the Néel model (Pike et al., 1999). As expected, it shows a decrease when the spacing is increased (Fig. 3.12). The first point (measured when the spacing is half the grain width) was not well defined because of the multiple peaks on the FORC diagram).

Again, the ratio $M_{\rm rs}/M_{\rm s}$ stays constant and could not be used to indicate a change in the interaction state of the system (Fig. 3.8c). The coercive field $H_{\rm c}$ increases when the spacing is increased up to 2 subcells and then decreases slightly (Fig. 3.8d). However, this variation is not correlated with the change from an interacting to a non-interacting system.

In the case of a 3×3×2 or 3×2×2 array, we observed the same pattern as for symmetric arrays: secondary branches appear as a result of interactions between grains and create secondary peaks on the FORC diagram.

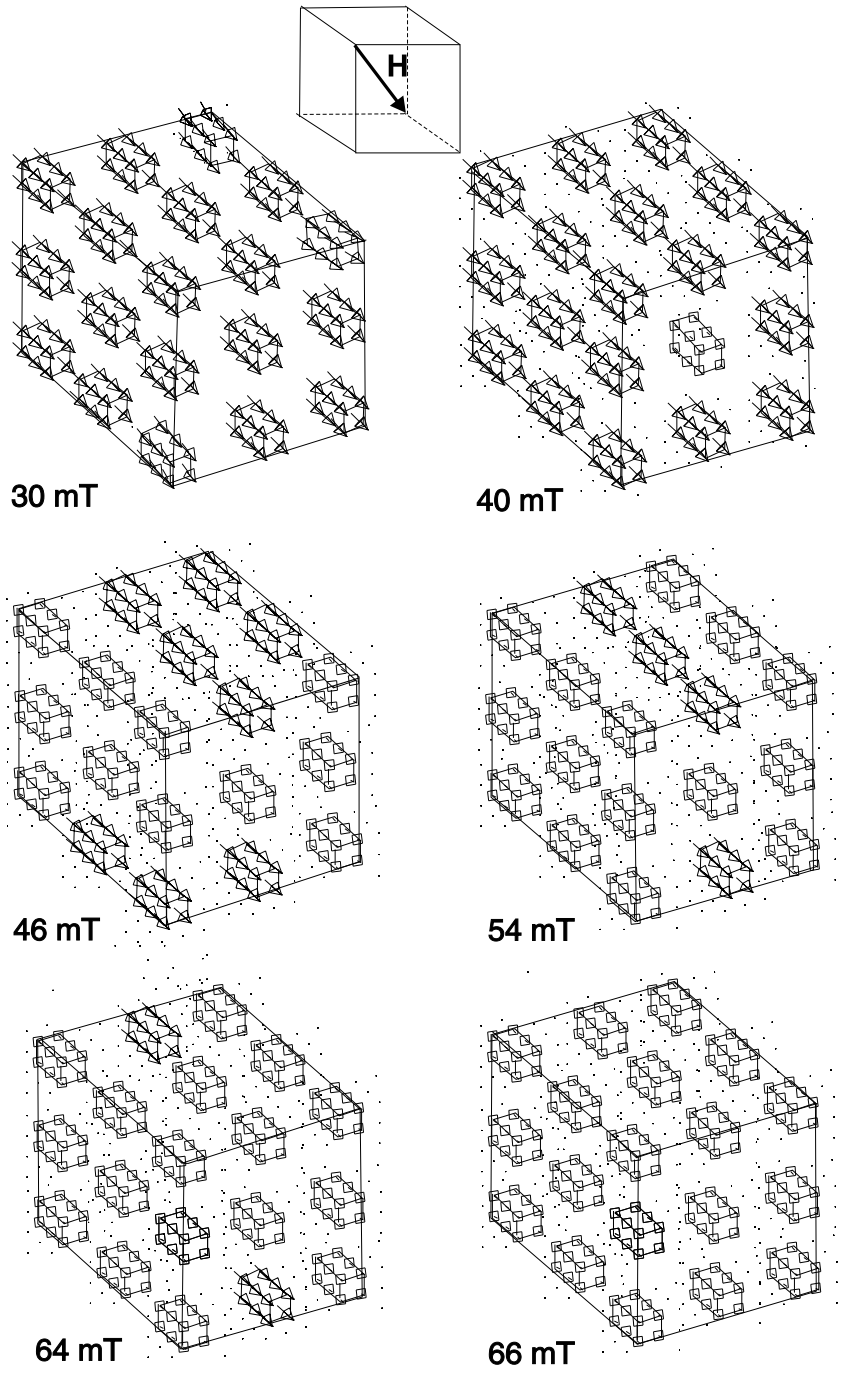

Figure 3.11: Micromagnetic structure of an array of 3×3×3 interacting elongated SD grains (grain size 0.045×0.03×0.03 μm, elongation ratio 1.5) during the measurement of a reversal curve corresponding to a reversal field of -70 mT. Arrows represented by a cross inside a square are pointing out of the page; arrows with a dot inside a square are pointing into the page.

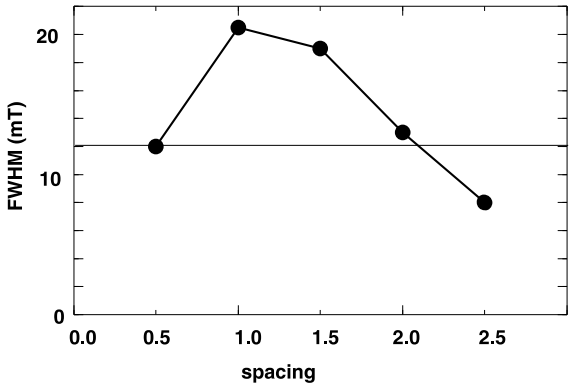

Figure 3.12: Full width at half maximum (FWHM) of the main peak of the FORC distribution parallel to the H_u axis through the peak H_c, as a function of spacing between particles, for a 3×3×3 array of SD elongated particles (grain size: 0.045×0.03×0.03 μm). The line at 12 mT represents the FWHM of an individual grain. If there are two peaks on the FORC distribution, I plot the average width of the two peaks. The field is applied along the [111] axis.

3.3.2 Array of cubic particles having random magnetocrystalline anisotropy axes

In order to study the case where particles are randomly oriented within an array, we revert to cubic particles but introduce uniaxial magnetocrystalline anisotropy whose orientation is random. I take for K_{u1} the first magnetocrystalline anisotropy constant for magnetite, K_1.

In the case of aligned anisotropy axes, the grains behave as a non-interacting array when the spacing is large because they all switch from a flower state in one direction to a flower state in the other direction at the same field. Now each grain has a different anisotropy direction, and so there is a range of switching fields. There are many more intermediate states, in principle one for each grain. There is a similar distribution for switching from the anisotropy easy axis to alignment with the negative field. Thus, the FORC diagram has a multiplicity of peaks. In the interacting case, the ensemble should behave more like a single magnetic structure, with grains reversing their magnetizations in different stages but this time because of the interactions. In both cases there will be intermediate states during the reversal process creating multiple peaks on the FORC diagram, but it is difficult to know if this effect is due to interactions between grains or because the moments of grains orient

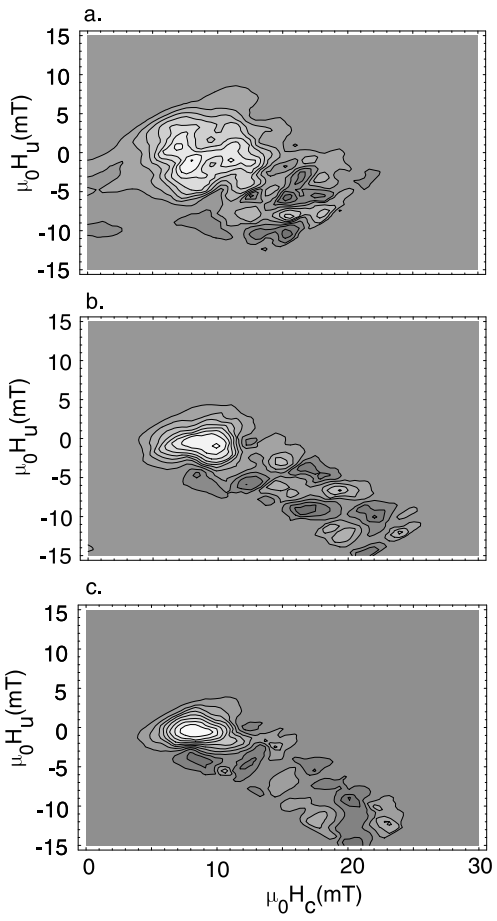

Figure 3.13: FORC diagram for an array of 5×5×5 cubic SD particles (grain size 0.04 μm). The spacing between grains is: (a) 2 times the grain length; (b) 3 times the grain length; (c) 4 times the grain length.

along different anisotropy axes when the field is reduced. Moreover, FORC diagrams are noisier than in the case of aligned shape anisotropy axes, making it even more difficult to look for fine features that might distinguish between the two cases.

3.4 Discussion

My FORC diagram for models of isolated SD particles is consistent with Stoner-Wohlfarth theory (Stoner & Wolfarth, 1948). FORC diagrams for PSD particles are characterized by secondary peaks resulting from minor branches on the reversal curves.

My micromagnetic models of FORC diagrams for assemblages of SD grains show distinctive features that can help to differentiate between interacting and non-interacting assemblages. For arrays of SD particles having aligned anisotropy directions, the presence of minor branches on the reversal curves indicates interactions among grains and causes the FORC diagram to have several positive and negative peaks instead of the single peak that occurs when the grains behave as independent systems. When the particles are closely spaced in a large array, the FORC distribution becomes noisy. In simpler cases (smaller arrays or fewer interacting particles where there is only one minor branch), I can identify two positive peaks that are symmetrical with respect to the H_c axis, another positive peak further away on the H_c axis at H_u=0, and a negative peak between the latter positive peak and the lower positive peak (Fig. 3.6).

In order to investigate the superposition of the peaks that would lead to the spread on the H_u axis that is observed experimentally, I modelled an array of 5×5×5 cubic SD particles. Each grain is represented by only one subcube. This simplification allows us to compare FORC diagrams for different spacings, even though the resolution is obviously too small. The spreading clearly appears in the more interacting array and diminishes with increasing spacing (Fig. 3.13).

Pike and Fernandez (1999) measured FORC diagrams for an array of Co dots with a strong uniaxial shape anisotropy. When saturated along their short axes, the grains relax into single vortex states (Fernandez et al., 1998). The FORC diagrams measured on these samples show a "butterfly" structure composed of two positive and two negative peaks. It is difficult to tell if this array is interacting or not because the M_s and C_E for cobalt are three times larger than M_s and C_E for magnetite and the exchange length for cobalt is a hundred times smaller than the exchange length for magnetite. Therefore, the conclusions drawn from my modelling cannot be quantitatively applied to the observations of Pike and Fernandez (1999). Moreover, micromagnetic modelling of even SD grains of cobalt would be very time consuming because of the resolution required by such a small exchange length. Since I have shown that interactions in arrays of particles with aligned anisotropy axes give rise to multiple peaks on the FORC diagram, it is, however, a possibility that the peaks defining the "butterfly" structure are due to interactions among grains.

An isolated PSD grain and an array of interacting SD grains show the same features on a FORC diagram, even though the physical origin of the splitting into several peaks is different in the two cases. This ambiguity cannot be resolved by our simple models of identical, regularly spaced grains. In a real sample having a distribution of grain sizes, orientations and spacings, the situation will be different. Experimentally, the FORC distribution of an ensemble of interacting SD grains has a closed peak (Roberts et al., 2000, Pike et al., 1999, Muxworthy & Dunlop, 2002) that spreads out along the H_c axis because of the distribution of coercivities and in the H_u direction because of the superposition of the secondary peaks caused by interactions. FORC distributions for PSD or MD grains are characterized by contours that diverge as one approaches the origin of the diagram (Roberts et al., 2000, Pike et al, 2001b, Muxworthy & Dunlop, 2002). I can explain the spreading parallel to the H_u axis as a superposition of secondary peaks resulting from the appearance of vortex and flower states.

The particles I have modelled are stress-free and defect-free. In real samples, the presence of defects is likely to cause stress fields impeding rotation of SD moments, therefore increasing H_c (Xu & Merrill, 1989). The spacing limit between interacting and non-interacting systems may change as well, but the splitting of the peaks would still be observed for interacting arrays.

Measured FORC diagrams are often found to be asymmetrical (Roberts et al., 2000, Pike et al., 1999; Pike et al., 2001b; Muxworthy & Dunlop, 2002). Experimental Preisach diagrams are also often asymmetrical (Hejda & Zelinka, 1990), even though in theory Preisach distributions are constrained to be symmetrical. The moving Preisach model (Hejda & Zelinka, 1990) in which the effective field is the sum of the applied field plus an interaction field proportional to the overall magnetization accounts for most of the asymmetry in Preisach diagrams. I find, however, that FORC diagrams for isolated PSD grains are asymmetrical, as are FORC diagrams for arrays of interacting SD particles.

For some paleomagnetic measurements, such as Thellier-Thellier paleointensity determinations, it is important to know if the assemblage is interacting or not, since interacting assemblages are likely to make the experiment fail. The best material for paleointensity experiments should have a FORC diagram with a symmetrical single peak having a high H_c

and little spread in the H_u direction. PSD-like FORC diagrams (peak at a smaller H_c and contours converging away from the H_u axis) may also be acceptable.

In paleoclimatic studies, changes in magnetic grain size and mineralogy can indicate changes in magnetic mineral sources and pathways, as well as changes in the flux of magnetic components to the sediment. These changes can be controlled by the effect of climate on the pathways, in particular through changes in atmospheric circulation and ocean currents in the case of deep-sea sediments (Evans & Heller, 2003). In environmental studies, a knowledge of grain size and magnetic mineralogy can give indications of various parameters such as sediment load and velocity, or particle transport during erosion. The ability of FORC diagrams to give a better description of grain size distribution and magnetic mineralogy is therefore also helpful for environmental and paleoclimatic studies.

Chapter 4

First-order reversal curve (FORC) diagrams of elongated single-domain grains at high and low temperatures

Most of Chapter 4 has been published in J. Geophys. Res. as: Claire Carvallo, Özden Özdemir and David J. Dunlop, First-order reversal curve (FORC) diagrams of elongated single-domain grains at high and low temperatures, doi: 2003JB002539, reproduced by permission of the American Geophysics Union.

4.1 Introduction

As was discussed in the previous chapter, FORC distributions contain a wealth of information not recorded by the bulk hysteresis parameters, which average over all grains. The properties of FORC distributions have been tested, mainly on magnetite (Fe_3O_4), for grain sizes with resulting domain structures that range from MD through PSD to single-domain SD (Pike et al., 1999, 2001a,b; Muxworthy & Dunlop, 2002). Because SD behavior in equidimensional magnetite occurs over a narrow size range, 0.03-0.07 μm, it is difficult to produce a purely SD magnetite sample. Grains typically have a range of sizes that encompasses PSD through thermally stable SD to thermally unstable SP behavior. This mixture of states complicates the interpretation of FORC results.

One solution is to use elongated grains, which have an extended SD size range. The long dimension of the grain can be as much as a few μm without compromising SD behavior, i.e., remanent magnetic states in which all spins are aligned, producing a magnetization equal to the spontaneous magnetization M_s, and rotation between these states at a critical magnetic field, H_c. For this reason, elongated SD grains are used in most magnetic recording media.

In this chapter, I report FORC diagrams measured below, at, and above room temperature for elongated SD grains of maghemite (γFe_2O_3). I chose a well characterized maghemite used in high-resolution magnetic recording because of its narrow size distribution (Özdemir, 1990). Maghemite has no low-temperature crystallographic transition, allowing me to measure FORC distributions below 120 K (the magnetite Verwey transition).

Maghemite generally inverts to hematite (αFe_2O_3) in heating above 500°C, making it impossible to determine the Curie temperature T_C, but this sample is unusually stable and has a T_C of 645°C (Özdemir & Banerjee, 1984). This and many other magnetic properties (e.g., $M_s(T)$ dependence, coercivity values, SD size range) resemble those of magnetite. The reason for measuring FORC diagrams at a variety of temperatures is to test predicted properties of the FORC distribution of interacting SD grains.

4.2 Sample characteristics

The synthetic maghemite sample contains grains of average length 0.45 $\pm$ 0.15 μm and elongation 9.4 $\pm$ 0.2 (Özdemir & Banerjee, 1984). X-ray analysis using Cu-K radiation gave numerous superstructure lines typical of maghemite. The spinel unit cell edge was a = 8.33 $\pm$ 0.01 Å. The room-temperature value of saturation magnetization M_s of 65.3 Am^2/kg is lower than the standard value 77 Am^2/kg due to micropores.

The ratio of saturation remanence M_{rs} to saturation magnetization M_s is 0.49 and the ratio of remanent coercive force H_{cr} (measured after the major loop) to H_c is 1.21. These values are typical of SD grains with uniaxial (shape) anisotropy and weak interactions (Dunlop & Özdemir, 1997). The remanence state is SD, but we do not assume that the reversal mode for these particles is uniform rotation. As shown by Newell and Merrill (1999), the limiting volume for a uniform reversal mode is $(0.1\ \mu m)^3$, which is about the mean size of

our particles. Another test of interactions is the crossover value R of normalized alternating field (AF) demagnetization and isothermal remanent magnetization (IRM) acquisition curves (Cisowski, 1981). Crossover occurred at $R = 0.43$ ($R = 0.46$ for DC demagnetization and IRM acquisition curves), compared to a theoretical $R = 0.50$ for no interactions (Wohlfarth, 1958).

4.3 FORC distributions

FORC measurements were made using two automated vibrating-sample magnetometers, measuring in the ranges 20 K–300 K and 300 K–900 K, respectively. The noise increased near T_C, where magnetizations are weak, requiring more smoothing (SF = 5) than at lower T (SF = 2 or 3).

FORC distributions measured at and below room temperature are highly reproducible and very similar in shape, apart from a slight expansion along both axes dictated by the increase in $M_s(T)$ (Fig. 4.1). The distribution has a single major peak centered on the H_c axis and roughly symmetrical in form. At room temperature, the peak is at $H_c \approx 40$ mT, $H_u = 0$, with a spread at half peak height of about ± 12.5 mT in both H_c and H_u. The microcoercivity distribution f(H_c) is thus quite narrow about the mean but the distribution g(H_u) is broader than anticipated from the interaction sensitive parameters M_{rs}/M_s and R (section 4.2).

The FORC distributions in Fig. 4.1 have two lobes, extending to high H_c and negative H_u. Both are most accentuated in the three lowest contours, the central distribution being close to circular. The $-H_u$ lobe is flanked at low H_c by a small negative peak, which persists at all temperatures up to 700 K (428°C; Fig. 4.2d) and seems to be real. The pattern is reminiscent of the distribution found theoretically by Pike et al. (1999) using a moving Preisach model with both local interaction fields (Néel, 1954) and a mean interaction field proportional to the net sample magnetization. However, in Pike et al.'s distribution, the negative peak lies immediately below the main positive peak and forces contours inward, whereas our negative peak is offset diagonally and the main peak contours are deflected around it. Thus it is uncertain whether the persistent pattern in our FORC distributions is

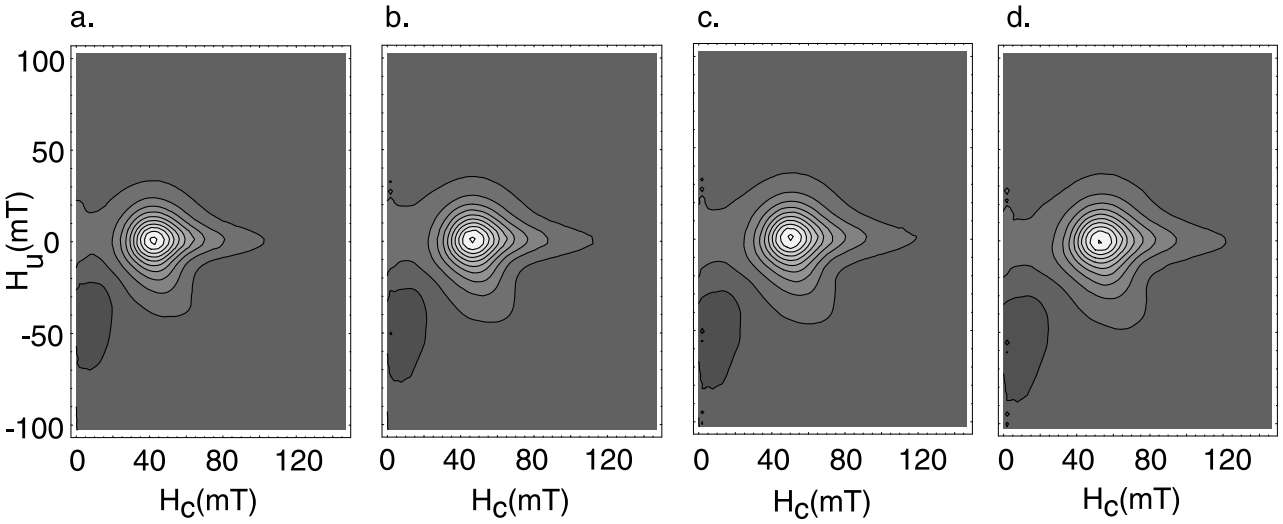

Figure 4.1: Low temperature FORC diagrams. a: 300K; b: 200K; c: 100K; d: 20K (SF=2)

evidence of mean-field interactions or not.

FORC distributions determined at and above room temperature appear in Fig. 4.2. The H_c scale has been expanded 30% relative to the H_u scale in Figs. 4.2a-d (the scales are identical along the two axes in Figs. 4.2e, f and in Fig. 4.1). As T increases from 150°C to 428°C, the tailing of the microcoercivity distribution to high H_c becomes more marked. The high-H_c lobe now includes the central contours, not just the outer ones, and the overall asymmetry in f(H_c) is more accentuated. Beginning with the 312°C data, the peak of the spectrum moves to lower H_c, eventually merging with the H_u axis at 580°C.

A similar trend was seen by Muxworthy & Dunlop (2002) over a similar T range for their finest (0.3 μm) PSD magnetite and was interpreted by them as marking a progressive change from SD-like to MD-like behavior. However, whereas their contours spread along the $+H_u$ and $-H_u$ axes in a symmetrical fashion at high T (a characteristic MD pattern), mine remain highly asymmetrical even at 580°C. There is no spreading at all along the $+H_u$ axis. In the $-H_u$ direction, the contours are actually compressed, while abrupt bends in these contours define a largely separated $-H_u$ lobe extending at least 3 times farther than the main distribution. As the $-H_u$ lobe moves with the main spectrum to lower H_c at 553 and 580°C, the flanking negative peak is annihilated.

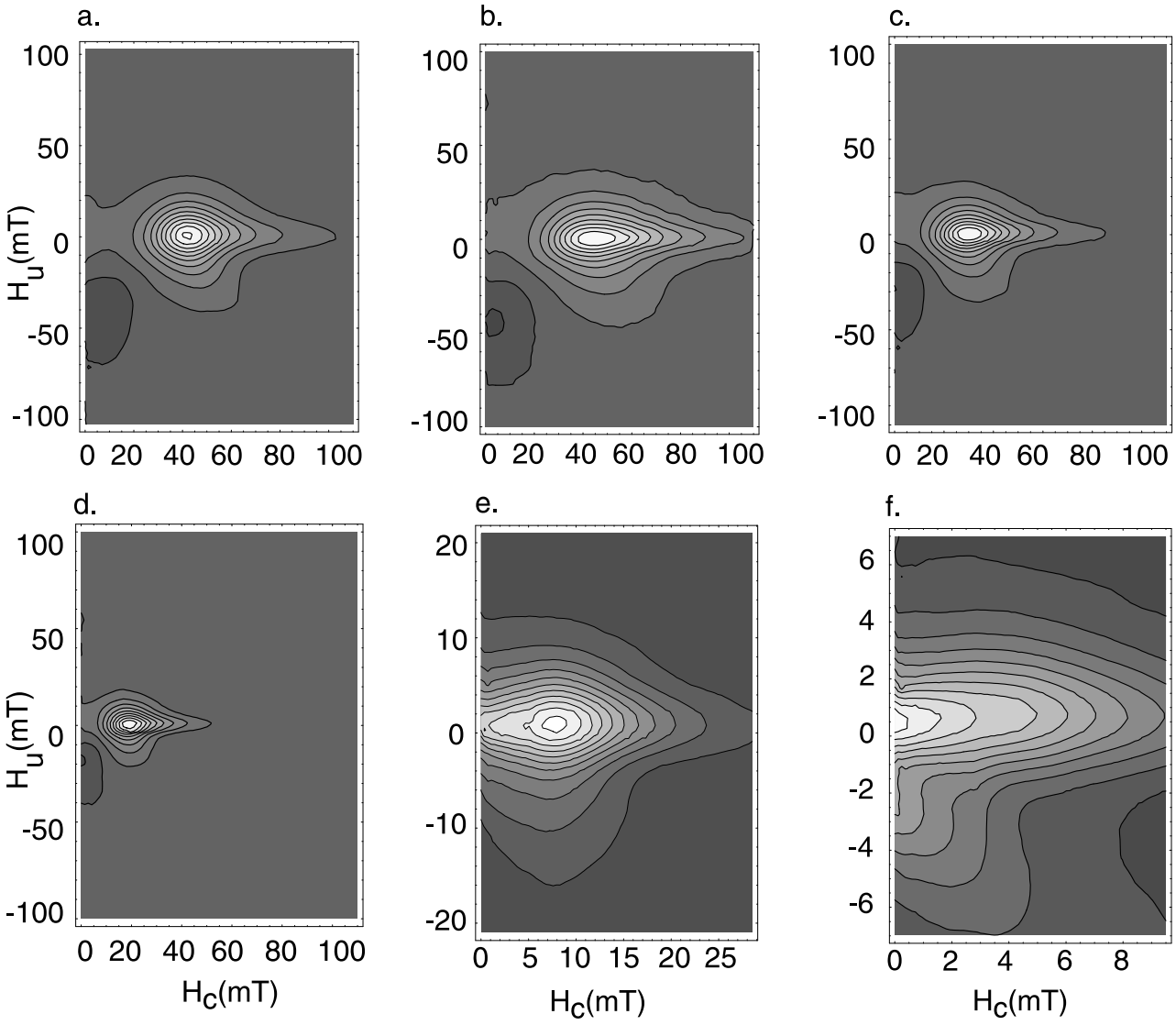

Figure 4.2: FORC diagrams for different temperatures. a: 25°C (SF=2); b:150°C (SF=2); c: 312°C; d: 428°C (SF=2); e: 553°C (SF=3); f: 580°C (SF=5)

4.4 Comparison with FORC diagrams of elongated SD magnetite

Magnetotactic bacteria are a very good example of elongated SD magnetite. These bacteria contain magnetite crystals within the stable SD size and shape arranged in chains within a magnetosome. Accordingly, individual SD magnetite crystals in bacterial magnetosomes have maximum intensity and stability of magnetization. The alignment of the crystals causes

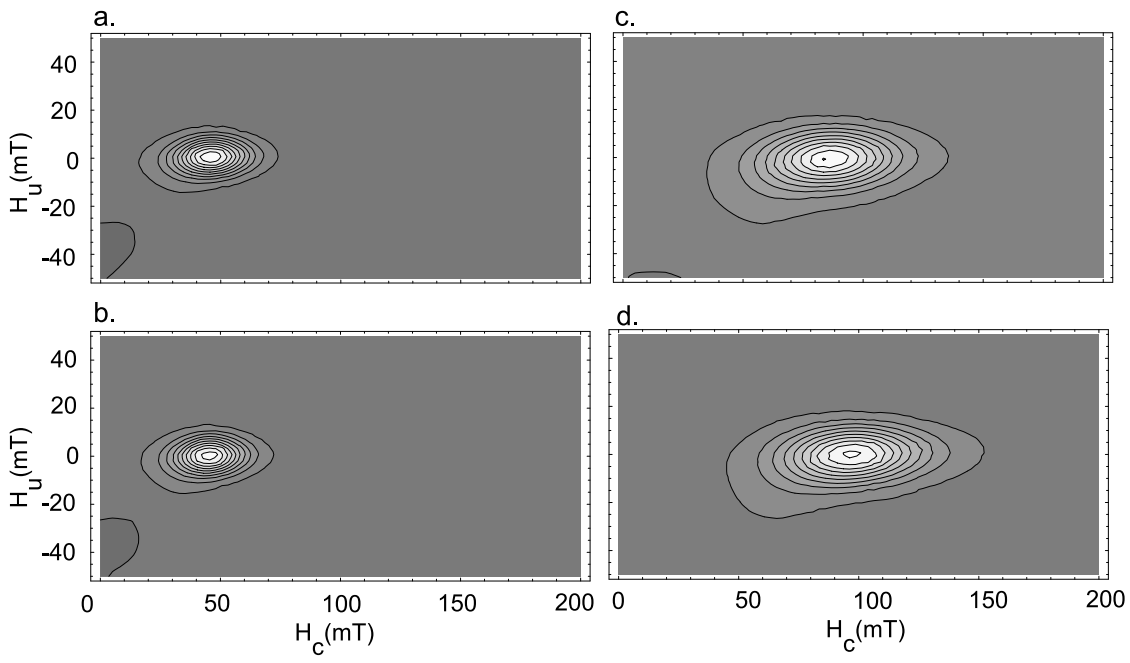

Figure 4.3: FORC diagrams of magnetotactic bacteria for different temperatures. a: 300 K; b:150 K; c: 50 K; d: 20 K. SF=2.

magnetocrystalline easy directions to be parallel to the chain and produces a very effective and stable magnet (Moskowitz et al., 1988). This magnet serves as a geomagnetic sensor that guides magnetotactic bacteria down magnetic flux lines, helping them to remain within the preferred habitat of oxygen-poor zones within muddy layers of accumulating sediment (Blakemore, 1975).

I measured FORC diagrams at room temperature and low temperatures for a sample of magnetotactic bacteria (supplied by Dr. B. Moskowitz). High-temperature FORCs were not measured in order not to alter the sample. FORC diagrams at all temperatures show a remarkably symmetrical closed peak and relatively little spread along the H_u axis (Fig. 4.3), indicating SD magnetic minerals with a small level of interactions in the sample. This pattern is consistent with FORC distributions obtained with micromagnetic models for aligned assemblages of non-interacting SD magnetite (Chap. 3).

There is almost no change in the FORC distribution when the temperature is decreased, until it reaches the Verwey transition (Fig. 4.3 a-b). At the Verwey transition, the coercivity at which the FORC distribution is maximum suddenly doubles, and then stays constant

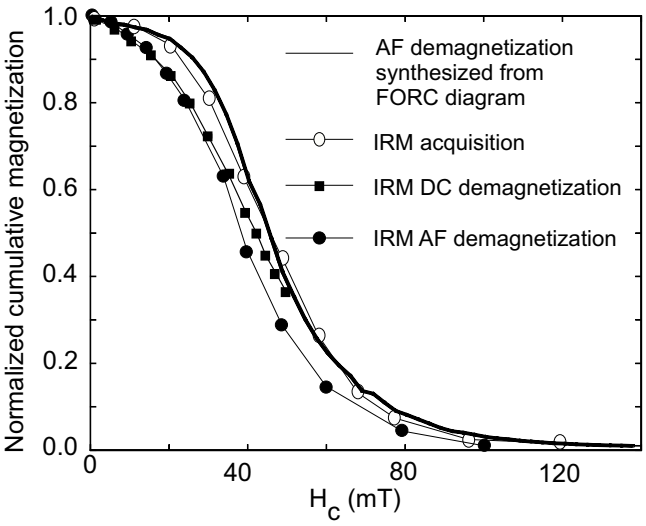

Figure 4.4: Cumulative distribution calculated from the FORC diagram at room temperature (heavy line) compared with other cumulative spectra calculated from: open circles: IRM acquisition curve; solid squares: IRM DC demagnetization curve; solid circles: IRM AF demagnetization curve.

when the temperature is decreased further. This increase in coercivity is accompanied by a spread of the distribution identical for both FORC variables (Fig. 4.3 c-d). Below the low-temperature crystallographic transition, the absence of changes in the FORC diagrams is consistent with the low-temperature FORC diagrams measured on elongated SD maghemite.

4.5 Analysis and discussion

Even though the low-temperature FORC diagrams of the magnetite and maghemite samples show consistent evolutions with temperature, it is more appropriate to use the maghemite sample for the analysis because the low-temperature crystallographic transition in magnetite adds further complexity to the interpretation of the evolution of the FORC diagrams.

Özdemir (1990) found that M_{rs}/M_s of this maghemite remained close to 0.5 for $T \leq$ 500°C, reached 0.45 by 550°C, and finally decreased strongly in the range 585° C to T_C. My measurements are similar and extend the range of constant $M_{rs}/M_s = 0.5$ to 20 K$\leq$ $T \leq$ 300 K. The lowest value measured was $M_{rs}/M_s \approx 0.27$ at 580°C. The constancy of M_{rs}/M_s at the value 0.5 expected for uniaxial SD grains confirms that the contraction of the FORC distribution observed above 300–400°C (Figs. 4.2c-f) is not a result of a shift to

more MD-like behavior. Rather it results from the decrease in all microcoercivities H_c due to thermal fluctuations at high T (Dunlop & Özdemir, 1997, Chap. 8). M_{rs}/M_s decreases abruptly when grains pass through their blocking temperatures T_B and become SP, but H_c decreases continuously over a broad range below T_B.

The constancy of M_{rs}/M_s has implications also for interactions. Mean-field interactions will affect M_{rs}/M_s, decreasing it for a net negative interaction (in the same manner as the internal demagnetizing field in MD grains) and increasing it for positive interaction. Since M_{rs}/M_s remains at or near 0.5 over a very wide range of T, I conclude that mean-field effects are minor compared to local interaction fields in this sample. Another hallmark of mean-field interactions, tilting of the axis of the FORC distribution (Pike et al., 1999), is also absent from my results. Thus, the diagonally flanking negative peak in my FORC diagrams for all $T \leq 428$°C must have a different cause than Pike et al.'s vertically offset negative peak.

Next, I test two predicted features of FORC distributions. These are the assumed match of a profile f(H_c) taken parallel to the H_c axis through the main peak with the microcoercivity distribution, and the association of a profile g(H_u) through the main peak parallel to the H_u axis with the spectrum of (local) interaction fields. The first is directly testable because the microcoercivity distribution can be measured independently by IRM acquisition and/or AF or DC demagnetization of the saturation remanence M_{rs}.

The commonest measure of the microcoercivity spectrum is the AF demagnetization curve, a (reverse) cumulative distribution, starting from 100% magnetization at zero AF. Other cumulative coercivity spectra can be recast in the same form, the IRM acquisition curve by plotting 1 – $M_{ir}(H)/M_{RS}$ vs. H and the DC demagnetization (or backfield) curve by plotting 1/2 [1 + $M_r(-H)/M_{RS}$] vs. H (Dunlop & West, 1969; Dunlop, 1986). Fig. 4.4 illustrates these three spectra, determined from the results of Özdemir (1990). For SD grains, differences between these distributions are usually attributed to interactions, e.g., the δM method (El-Hilo et al., 1992) and the Henkel plot (Proksch & Moskowitz, 1994). The interactions here are negative, since the AF and DC demagnetization curves lie below the inverted IRM acquisition curve, and small, with a maximum difference between pairs of curves of $\approx$ 7.5 mT.

In Fig. 4.4 is plotted also the cumulative distribution obtained by integrating f(H_c),

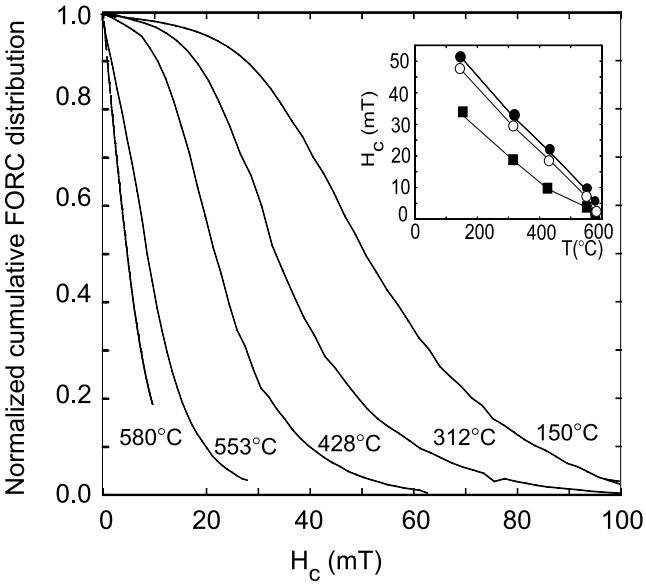

Figure 4.5: Cumulative distributions calculated from the FORC diagram at different temperatures. Inset: solid circles: median field of the cumulative FORC distribution; open circles: peak value of the FORC distribution; solid squares: $H_c(T)$ from the major hysteresis loops.

profiled parallel to the H_c axis through the peak of the 300 K FORC distribution. It closely resembles the experimental coercivity spectra, especially the AF demagnetization curve, although it is displaced slightly to higher fields. There is little doubt that the FORC diagram has the power to predict the measured microcoercivity distribution of a sample.

A further test of the interpretation that H_c in the FORC diagram represents microcoercivity is to compare cumulative f(H_c) profiles at different T (Fig. 4.5). The initial plateau in the spectrum measured at 150°C is also seen in AF demagnetization curves of SD grains; indeed it is one of the hallmarks of SD behavior (Dunlop & Özdemir, 1997, Chaps. 11, 12). The plateau in the spectrum is reduced in size at 312°C and 428°C and disappears above 550°C. Exactly the same pattern is seen in AF demagnetization curves of saturation remanence directly measured at high T for equidimensional SD and near-SD magnetite grains (Fig. 4.6). The main difference between my set of curves (Fig. 4.5) and the measured high-T AF curves (Fig. 4.6) is that our elongated SD grains have higher shape anisotropy and correspondingly higher H_c values. The change in shape of the spectrum with increasing T does not indicate a shift towards more MD-like behavior. It is due to the effect of thermal fluctuations on H_c (Dunlop & Bina, 1977; Dunlop & Özdemir, 1997, Chap. 8).

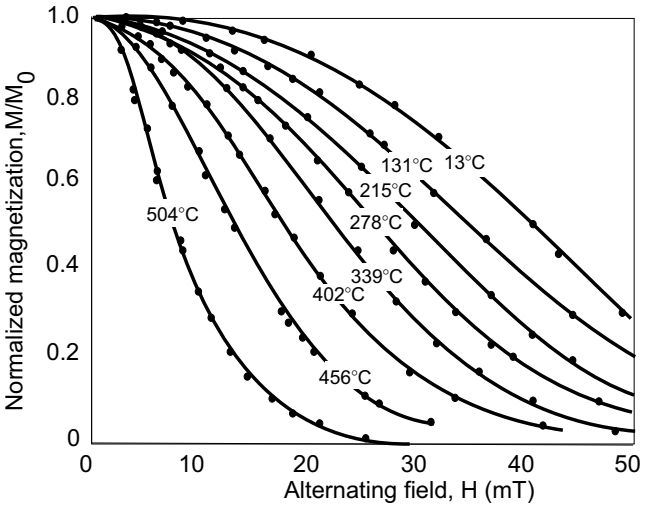

Figure 4.6: Alternating field demagnetization of a 0.037 μm SD magnetite sample measured at high temperatures, after *Dunlop & Bina* (1977).

The bulk coercive force H_c is an average over the microcoercivity spectrum f(H_c). H_c is consistently smaller than remanent coercivities such as H_{cr} or the median fields of IRM acquisition and AF demagnetization because the condition $M = 0$ is reached with a smaller backfield $-H$ than the condition $M_r = 0$. Nevertheless H_c should decrease in much the same way as remanent coercivities when T increases. This expectation is tested in Fig. 4.5 (inset), which compares $H_c(T)$ data from the major loop at each T with peak and median H_c values of the FORC distribution at the same T. The variations are quite similar, although H_c is about 35% lower than the peak and median H_c values at the lower temperatures and this difference increases at high T where unblocked SP grains provide a large negative induced M that causes H_c to plummet.

Testing the equivalence of H_u in the FORC distribution and particle interaction field H_i is more problematic because interactions cannot be measured directly. Pike et al. (1999) measured an $\approx 30\%$ increase in the width of g(H_u) at half peak height as the concentration of dispersed SD particles increased from 1.5% to 9%. A different test is based on the fact that the interaction field, whether local or averaged over the sample, is magnetostatic and should therefore vary with T as $M_s(T)$ (Muxworthy & Dunlop, 2002). In Fig. 4.7, I show half-profiles g(H_u) taken through the FORC peak in the $+H_u$ direction (the more regular half of the distribution) at different T. The median field H_{med} of each profile is plotted

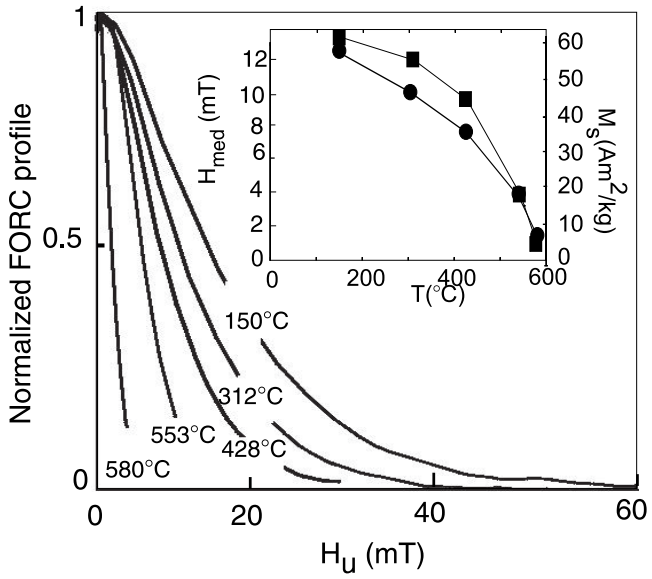

Figure 4.7: Half-profile taken through the FORC peak in the $+H_u$ direction for different temperatures. Inset: solid circles: median field of the profiles; solid squares: $M_s(T)$ from the major loops

against T (inset) and compared with $M_s(T)$. Like Muxworthy & Dunlop (2002) but unlike Dunlop et al. (1990), who found $H_{med}(T) \propto H_c(T)$, I find $H_{med}(T) \propto M_s(T)$. My results therefore support $H_u \equiv H_i$.

Preisach diagrams are in principle able to predict and interpret the results of different types of magnetic measurements, such as ARM and IRM acquisition, or AF demagnetization. (Dunlop & Özdemir, 1997). The comparison of experimental coercivity spectra of various types (AF demagnetization of IRM, IRM acquisition and DC demagnetizaion of IRM) to the FORC profiles shows that FORC diagrams also have a predictive power. For example, the results from this chapter suggest that a FORC diagram could be constructed based on minor DC field loops but used to predict the AF demagnetization properties. However, this result is based on only one type of sample (elongated SD, weakly interacting material). Comparisons between FORC profiles and coercivity spectra should be carried out on samples having varius grain sizes and interaction states in order to establish the predictive power of FORC diagrams.

Even though the most important application of this study is to show that, in the case of SD grains, the FORC distribution along the horizontal axis does represent the microcoerciv-

ity distribution and the distribution along the vertical axis, the interaction field distribution, our work is also applicable to studies of elongated SD grains in nature. For example, crystallographically oriented needles of magnetite in pyroxenes (Evans et al., 1968; Renne et al., 2002; Feinberg et al., 2003) and plagioclase (Murthy et al., 1971; Hargraves and Young, 1969) are common in nature and they impart unexpectedly intense and stable natural remanent magnetization to gabbros, anorthosites and some diabases. Also, rods of titanium-poor titanomagnetite isolated by ilmenite lamellas in the course of oxyexsolution are thought to carry the highest-coercivity fraction of NRM in continental and submarine basalts (Strangway et al., 1968).

Chapter 5

FORC diagrams of magnetic mixtures: measurements and micromagnetic modelling

5.1 Introduction

Natural samples usually contain mixtures of magnetic minerals in various domain states. An accurate identification of the magnetic minerals and domain states is necessary in many studies in paleomagnetism or environmental magnetism. For example, the reliability of paleomagnetic recording is strongly dependent on grain size. However, mixtures greatly complicate magnetic signals.

Hysteresis loops have been used quite often to identify minerals in magnetic mixtures, particularly distorted loops. For bimodal mixtures, these may be characterized by a constricted middle ("wasp-waisted loops") or by a spreading middle and slouching shoulders ("potbellies") (Tauxe et al., 1996). Measurements and simulations have indicated that SD/SP mixtures can readily produce wasp-waisted and potbellied loops (Tauxe et al., 1996). Mixtures of two minerals, one magnetically soft (magnetite or maghemite, for example) and one magnetically hard (like hematite or goethite) can also produce wasp-waisted loops, provided the two phases contribute comparable amounts of magnetization. Because the saturation

magnetization of hematite is 200 times smaller than that of magnetite, a very large amount of hematite must be present in the mixture to produce a wasp-waisted loop (Roberts et al., 1995).

Hysteresis parameters give some indications of the domain state of the dominant magnetic mineral. However there is more and more evidence that hysteresis parameters can give ambiguous results, because variations in internal stress, grain interactions, mineral composition and grain size can yield similar hysteresis parameters (Dunlop, 2002a). Thermomagnetic curves or susceptibility variations with temperature can sometimes help in identifying the magnetic mineralogy, provided that the ranges of Curie points do not overlap. Phase transitions at low temperature (Verwey transition at $\sim$120 K for magnetite, Morin transition at $\sim$258 K for hematite, pyrrhotite at 30-34 K) are also a very useful way of identifying the presence of these minerals. Magnetic granulometry techniques usually provide only a measure of the average mineral magnetic properties in a sample and tend to break down when a sample contains a mixture of grain sizes (e.g., Day et al., 1977). Mixtures of grains of different sizes can be detected in several ways. For example, SP grains can be detected by measuring the frequency dependence of magnetic susceptibility (Bloemendal et al., 1985). Low-temperature demagnetization (cooling below the anisotropy transition of magnetite and warming up to room temperature in zero field) can be helpful in estimating the domain state. The SIRM of MD grains will be preferentially demagnetized during low-temperature treatment, while SD grains stay largely unaffected (Dunlop & Argyle, 1991). This method allows one to discriminate between mixtures of SD+SP and SD+MD magnetite, because SP grains do not contribute to the remanence.

In non-interacting assemblages, the magnetizations of different phases are linearly additive (Roberts et al., 1995). However, in assemblages with magnetostatic interactions, linear additivity is more controversial. Lees (1997) demonstrated non-linearity of magnetization as a function of mixing ratio, while Carter-Stiglitz et al. (2001) found linear additivity in their samples.

Since FORC diagrams are able to reveal the coercive force distribution as well as the magnetic interactions within an assemblage, they should provide a good method to identify individual minerals in magnetic mixtures. In particular, mixtures of magnetic minerals

that have distinct coercivities (magnetite and hematite, or magnetite with different grain sizes for example) should plot in different areas of the FORC diagram. Only a few FORC diagrams of bimodal distributions and assemblages of different magnetic minerals in both natural and synthetic samples have been measured (Roberts et al, 2000; Muxworthy et al., 2003c). I have taken a micromagnetic modelling approach to better understand the response of interacting and non-interacting assemblages of single-domain grains on a FORC diagram. I have also measured FORC diagrams for a series of mixtures of magnetites that have a bimodal coercivity distribution, as well as mixtures of magnetite and hematite.

5.2 Modelling of FORC diagrams for mixtures

5.2.1 Micromagnetic model

The micromagnetic model used here is very similar to the model used in Chapter 3. In order to model large arrays of particles, the grains are assumed to be perfectly single-domain, i.e., there is no variation of magnetization within a grain and each grain can then be represented by one magnetic moment. The spacing between the grains can be adjusted; this permits modelling different levels of interactions in the assemblage (Muxworthy et al., 2003b).

5.2.2 Bimodal mixtures of magnetite

I used arrays of 6×6×6 (216) grains to model mixtures of magnetite having a bimodal coercivity distribution. In order to determine the coercivity of a particular grain in the array, a random number between 0 and 1 is picked for each grain. As an example, if the assemblage is 20% of coercivity A and 80% of coercivity B, the grain will be assigned coercivity A if the random number is smaller than 0.2 and coercivity B if the random number is larger than 0.2. The assemblages modeled in this section are composed of 20% of A, 80% of B; 40% of A, 60% of B; 60% of A, 40% of B; or 80% of A, 20% of B. For the model assemblages of non-interacting randomly oriented uniaxial SD grains, the ratios M_{rs}/M_s are between 0.48 and 0.50, in good agreement with the theoretical value of 0.5 (Dunlop, 1971).

FORC diagrams were modelled for five bimodal mixtures. Coercivities for the first mix-

ture were 28 mT (M1) and 22 mT (M2). The second mixture was composed of grains having coercivities of 18 mT (M3) and 28 mT. The third mixture had grains of coercivities of 14 (M4) and 28 mT. The fourth mixture had grains of coercivities of 11 mT (M5) and 28 mT. Finally, the particles in the fifth mixture had coercivities of 8 mT (M6) and 28 mT.

Variations in H_c for the same nominal grain size are sensitive to the method of sample preparation, so it is difficult to give an estimate of grain size that corresponds to each coercivity fraction in the mixtures. Moreover, the exact grain size does not really matter for this study. Based on experimental data from crushed grains (Hunt et al., 1995), estimated orders of magnitude for the grain sizes would be: 0.03 μm for M1, 0.05 μm for M2, 0.07 μm for M3, 0.09 μm for M4, 0.12 μm for M5, and 0.2 μm for M6.

The linear additivity of mixtures was first tested by producing a linear combination of the FORC diagrams of the end-members weighted according to the proportions of each element and comparing it with the FORC diagram obtained for a mixture of the same proportions of particles of either coercivity. A more rigorous way of checking the linear additivity is to inversely numerically fit the FORCs of the endmembers to the FORCs of the mixed sample (Muxworthy et al, 2003c). This gives the proportion of each end-member that best fits the mixture. Fitting is done using a least squares method. I can then compare the proportions obtained from the fitting to the actual proportions of the model mixture.

Non-interacting mixtures

Micromagnetic models of FORC diagrams for an array of non-interacting uniform SD particles having the same size (therefore the same coercivity) are characterized by a single peak centered at ($H_u = 0$, H_c). The FORC diagrams of non-interacting mixtures were all calculated with a smoothing factor of 3, which is rather low. Figures 5.1 and 5.2 show two examples of various combinations of the three mixtures, as well as the linear addition of the end-members for each mixture. The presence of two different coercivities is apparent in each case. The FORC peaks might overlap if the coercivities are too similar (Fig. 5.2 for example).

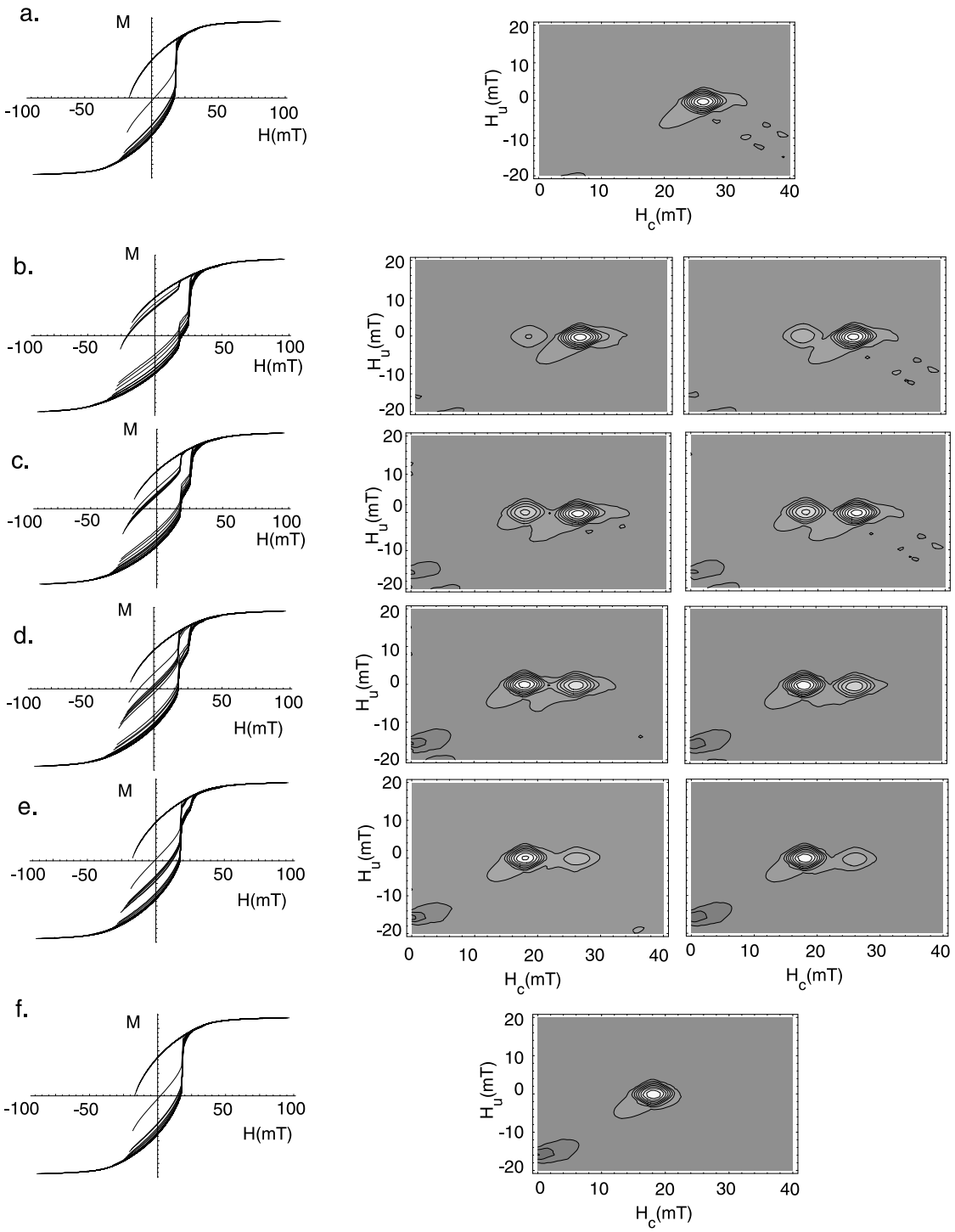

Figure 5.1: FORC diagrams for different non-interacting mixtures of M1 (28 mT) and M3 (18 mT). a: 100% M1; b: 80% M1, 20% M3; c: 60% M1, 40% M3; d: 40% M1, 60% M3; e: 20% M1, 80% M3; f: 100% M3. On the left are plotted the first-order reversal curves. The centre column shows the FORC diagrams modelled as explained in the text; the right column shows the FORC diagrams calculated by linearly superimposing the endmembers.

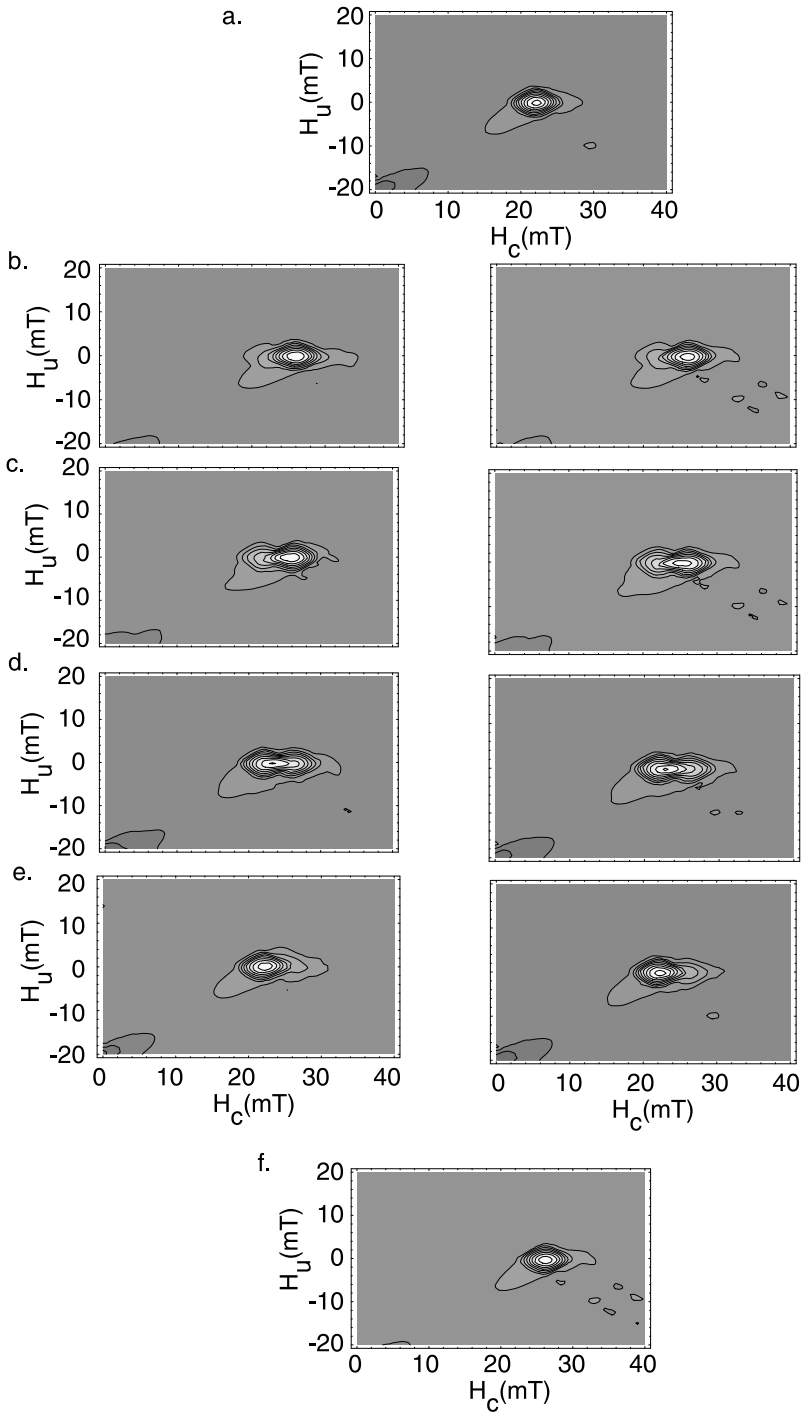

Figure 5.2: FORC diagrams for different non-interacting mixtures of M1 (28 mT) and M2 (22 mT). a: 100% M1; b: 80% M1, 20% M2; c: 60% M1, 40% M2; d: 40% M1, 60% M2; e: 20% M1, 80% M2; f: 100% M2. The left column shows the FORC diagrams modelled as explained in the text; the right column shows the FORC diagrams calculated by linearly superimposing the endmembers.

Interacting mixtures

The FORC distributions of interacting mixtures are much noisier than for non-interacting mixtures, and the noise level increases with decreasing spacing. The smoothing factor is now increased to 5. Three different particle spacings (between particle boundaries, in units of particle length) were used to model interacting assemblages: 1.5, 2 and 3.

The FORC diagrams for two different mixtures of M1 and M4 are plotted in Figures 5.3 and 5.4. Another example of a mixture with different coercivities (M1 and M2) is shown in Figures 5.5 and 5.6. Linear additions of the end-members are also shown. The FORC distributions are much more spread out along the H_u axis than in the non-interacting case. For example, with identical smoothing factors of 5, an assemblage of non-interacting M1 and M5 only spreads over 12.5 mT on the H_c axis and 12 mT on the H_u axis, whereas the main peak of an interacting mixture (d=1.5) still spreads over 12.5 mT on the H_c axis, but almost 25 mT on the H_u axis. This is consistent with the experimental evidence that spreading along the H_u axis indicates the presence of magnetostastic interactions. The full widths at half maximum (FWHM) are shown in Fig. 5.7. Muxworthy et al. (2003b) observed the same evolution of spreading along the vertical axis with decreasing spacing.

Linear additivity

Figure 5.8 shows experimental proportions of one end-member versus the predicted proportions of the same end-member from the end-member fitting, for the five different mixtures. Because the proportions of the mixture are calculated by picking random numbers, there is also an error in the composition itself. As an example, for a mixture composed of nominally 20% of M1 and 80% of M2, a grain will be M1 if the random number is smaller than 0.2 and M2 if the number is larger than 0.2. Because the assemblages are composed of only 216 grains, the actual proportions of M1 and M2 in the assemblage will deviate somewhat from the nominal composition. By trying several random compositions, I find that the actual composition of the mixture can deviate as much as 6% from the assigned composition. Therefore I estimate the error on the actual composition to be $\pm$6%.

Regardless of the spacing, additivity holds quite well for all the mixtures. The predicted

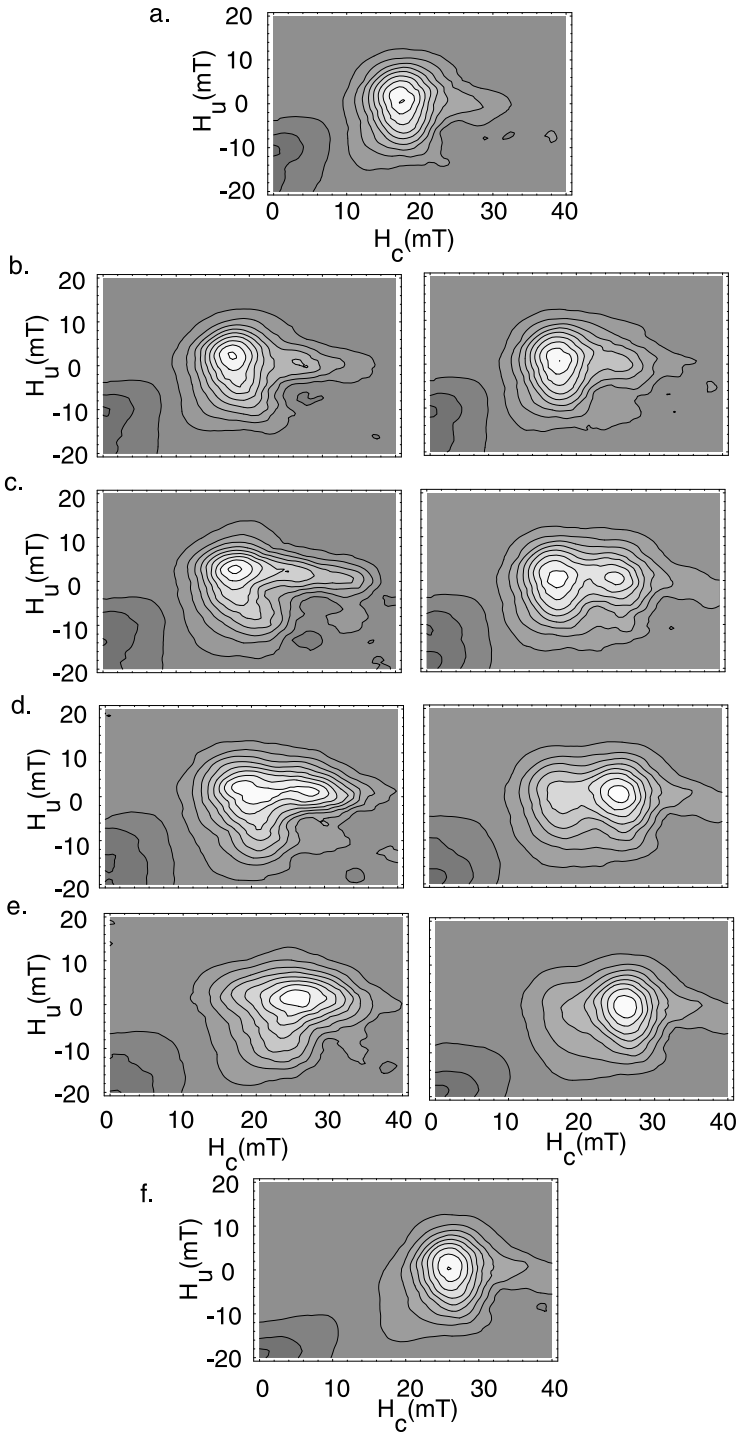

Figure 5.3: FORC diagrams for different mixtures of M1 (28 mT) and M3 (18 mT). a: 100% M1; b: 80% M1, 20% M3; c: 60% M1, 40% M3; d: 40% M1, 60% M3; e: 20% M1, 80% M3; f: 100% M3. The left column shows the FORC diagrams modelled as explained in the text; the right column shows the FORC diagrams calculated by linearly superimposing the endmembers. Spacing is 1.5 particle lengths.

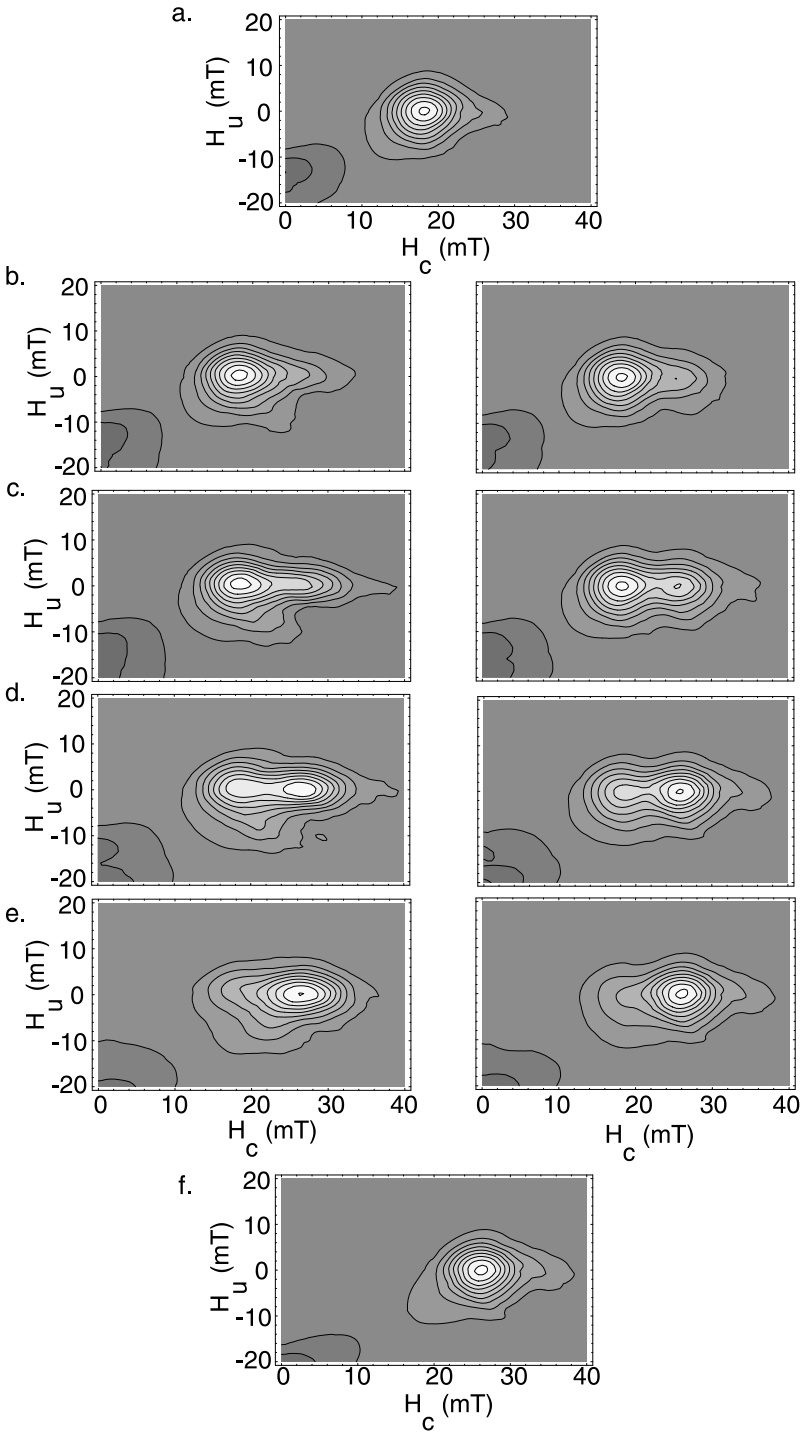

Figure 5.4: FORC diagrams for different mixtures of M1 (28 mT) and M3 (18 mT). a: 100% M1; b: 80% M1, 20% M3; c: 60% M1, 40% M3; d: 40% M1, 60% M3; e: 20% M1, 80% M3; f: 100% M3. The left column shows the FORC diagrams modelled as explained in the text; the right column shows the FORC diagrams calculated by linearly superimposing the endmembers. Spacing is 2 particle lengths.

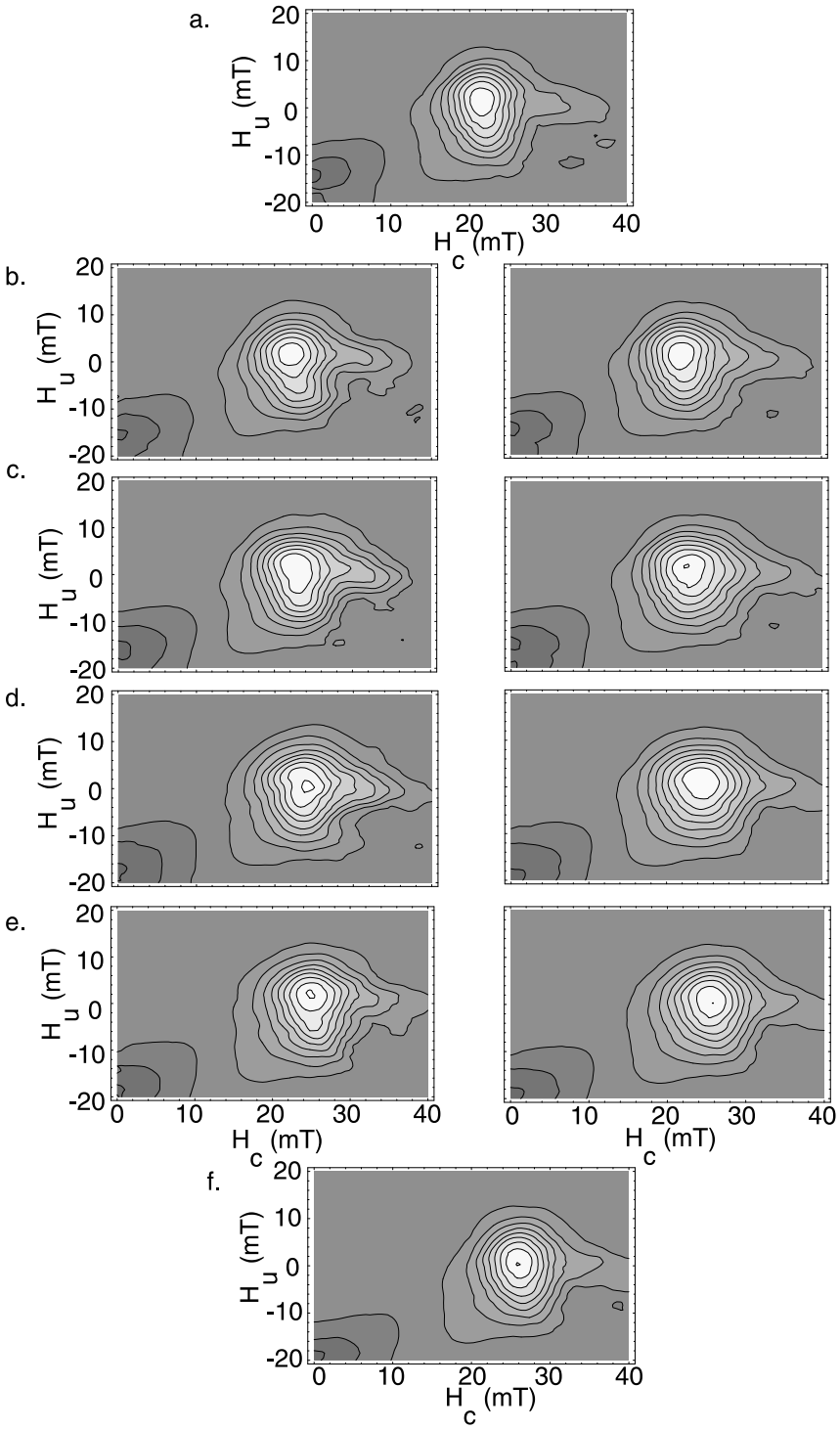

Figure 5.5: FORC diagrams for different mixtures of M1 (28 mT) and M2 (22 mT). a: 100% M2; b: 80% M1, 20% M2; c: 60% M1, 40% M2; d: 40% M1, 60% M2; e: 20% M1, 80% M2; f: 100% M2. The left column shows the FORC diagrams modelled as explained in the text; the right column shows the FORC diagrams calculated by linearly superimposing the endmembers. Spacing is 1.5 particle lengths.

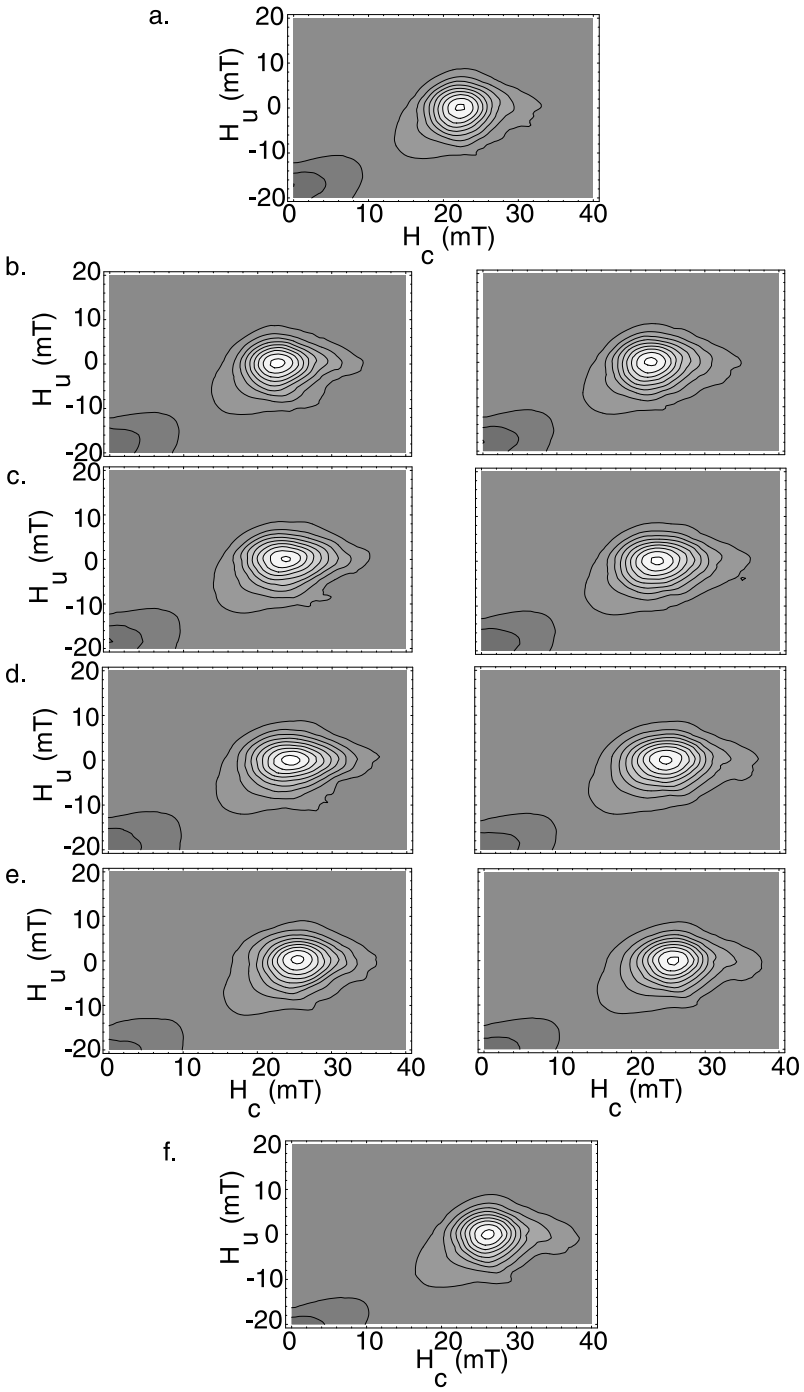

Figure 5.6: FORC diagrams for different mixtures of M1 (28 mT) and M2 (22 mT). a: 100% M1; b: 80% M1, 20% M2; c: 60% M1, 40% M1; d: 40% M1, 60% M2; e: 20% M1, 80% M2; f: 100% M2. The left column shows the FORC diagrams modelled as explained in the text; the right column shows the FORC diagrams calculated by linearly superimposing the endmembers. Spacing is 2 particle lengths.

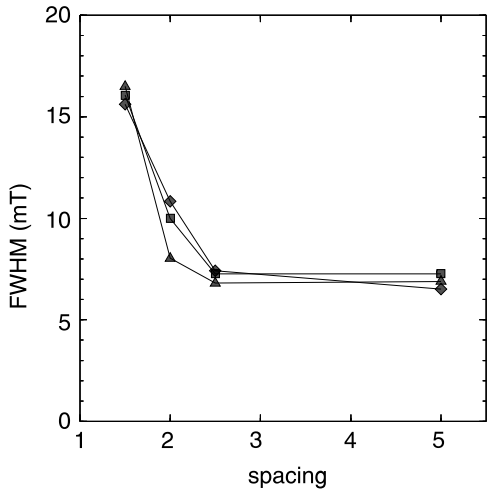

Figure 5.7: Full width at half-maximum of the FORC diagrams as a function of spacing in particle lengths between grains. Squares: M1-M2 mixture; diamonds: M1-M4 mixture; triangles: M1-M6 mixtures.

proportions are always within 7% of the actual proportions. This result is expected for the non-interacting mixtures, but was not anticipated for the interacting mixtures (Figs. 5.3 to 5.6). The errors in the fits are small because of the large number of data used for each fit (more than 6000). However, the standard deviations of the fits are about ten times larger when the particles in the mixtures are interacting than when they are not. This error is still at least three orders of magnitude smaller than the differences between predicted and actual mixture proportions.

For interacting mixtures, the comparison between predicted and measured FORC diagrams show that interactions do have an effect on the FORC diagrams (Fig. 5.3, 5.4 for instance). The low-H_c component remains more dominant than simple linear superposition of FORCs would predict. The test of linear additivity only tests whether it is possible to unmix and get approximately the correct proportions, within about 7%. Non-linearity in the sense of being able to see a difference between FORC measurements and predictions is a plus if the objective is to detect interactions, for instance for pre-selection of paleointensity samples.

A larger error in the fitted compositions comes from the random nature of the grain orientation in the assemblage. Since the array is relatively small (216 grains), there will be

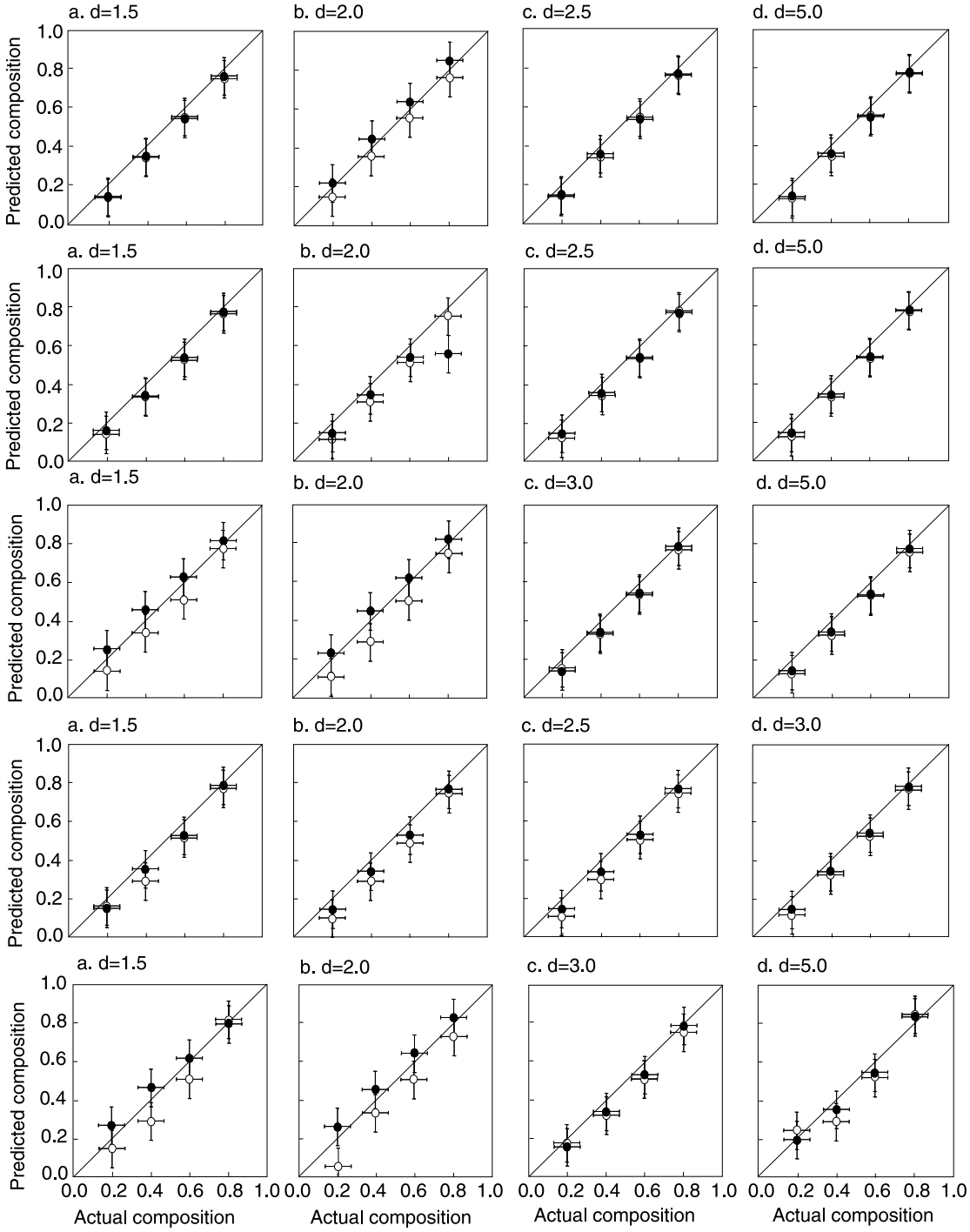

Figure 5.8: Predicted percent of one end-member versus that in the actual mixture, for various values of spacing between particles. The predicted percent was obtained by linearly fitting: closed circles: end-member FORCs to the mixed sample FORC; open circles: end-member major hysteresis loops to the mixed sample hysteresis loops. The y=x line shows linear addition. Mixtures are, from top to bottom: M1 and M6; M1 and M5; M1 and M4; M1 and M3; M1 and M2.

some variation in the predicted proportions of end-members when a different set of grain orientations is used to model the end-member. This error is difficult to estimate. I re-calculated FORC diagrams for each of the end-members using a set of grain orientations different from the orientations previously used. Then I fitted the mixture FORC diagrams to these new end-members. Composition differences range from 2 to 10%. Therefore I chose 10% as an error estimate on the predicted compositions. The errorbars in Fig. 5.8 represent this error. The error could be decreased by increasing the size of the arrays, but the computation time would then be significantly increased.

Linear additivity of the major hysteresis loops was also tested. By repeating the fitting using different random orientations of the grains in the end-members, I also find a difference up to 10%. In general, predicted proportions of end-members follow the trend of the actual proportions fairly closely, but not as closely as the proportions predicted from FORC diagram linear additivity. However, they generally are only different by a few percent from the compositions predicted by FORC diagram linear additivity.

5.2.3 Mixtures of magnetite and hematite

In order to investigate the linear additivity of FORC diagrams for mixtures of hematite and magnetite, some of the magnetite was replaced by hematite in the model used in the previous part. Hematite's magnetocrystalline anisotropy is hexagonal in the basal plane, and the orientation of the easy axis was randomly chosen. The saturation magnetization of hematite is only 0.5% that of magnetite, so it is expected that the mixtures must contain mostly hematite and a very small amount of magnetite for the effect of hematite to be visible. The number of particles in each mixture was increased to 1000. Another consequence of the huge difference in saturation magnetization between the two minerals is that significant magnetostatic interactions between hematite and magnetite are unlikely. This was also proven by Williams (1995) in the only micromagnetic model of hysteresis loops for magnetite and hematite mixtures.

I calculated FORC diagrams for mixtures of hematite and magnetite for various spacings between particles. Fig. 5.9 shows the FORC diagrams for mixtures of grains separated by 5 grain lengths. Unlike the mixtures of magnetite, the spacing variation has no effect on

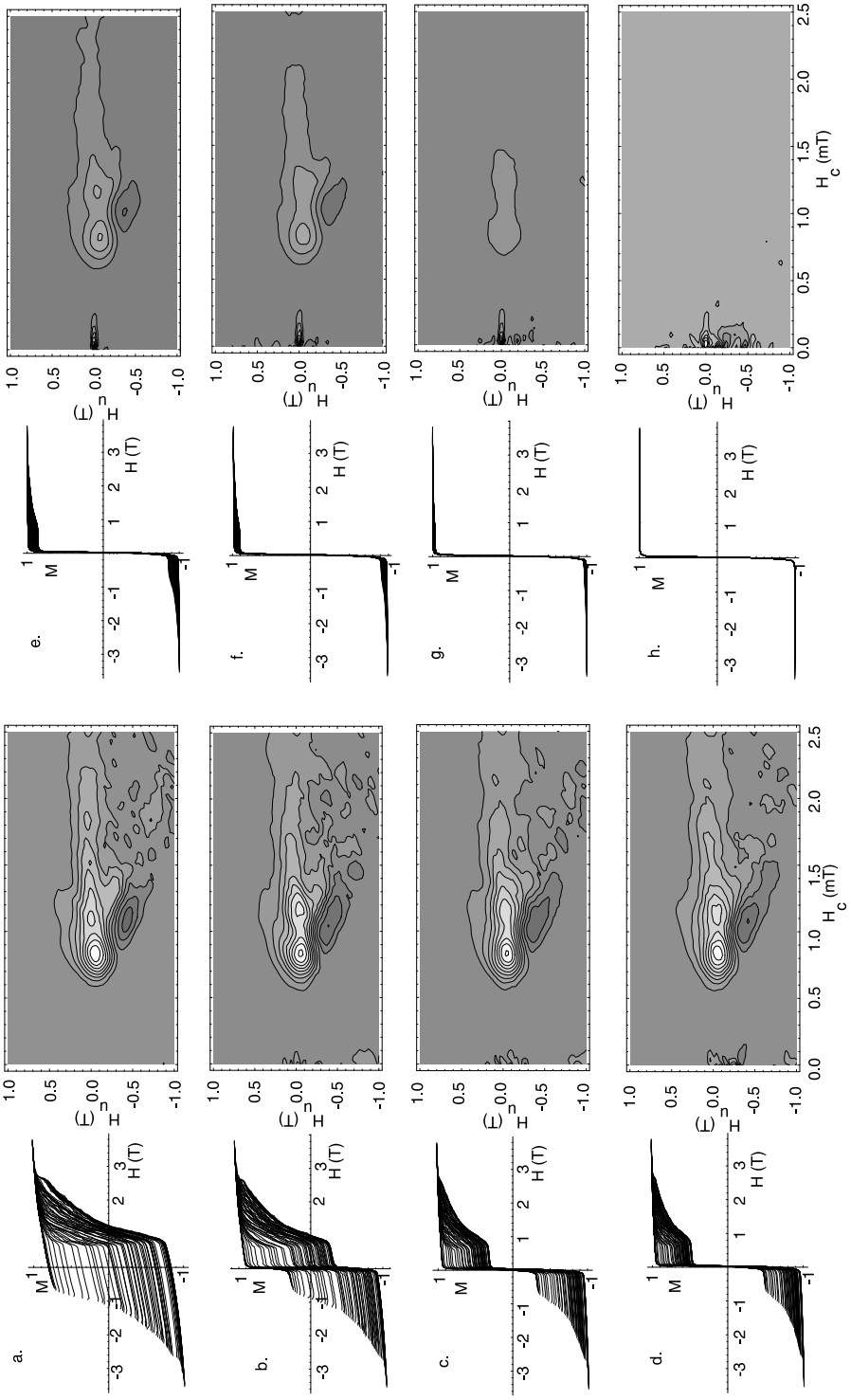

Figure 5.9: First-order reversal curves (left) and FORC diagrams (right) for mixtures of hematite and magnetite. a: 100% hematite; b:0.2% magnetite, 99.8% hematite; c: 0.5% magnetite, 99.5% hematite; d: 1% magnetite, 99% magnetite; d: 5% magnetite, 95% hematite; e: 10% magnetite, 90% hematite; f: 20% magnetite, 80% hematite; g: 30% magnetite, 70% hematite; h: 100% magnetite.

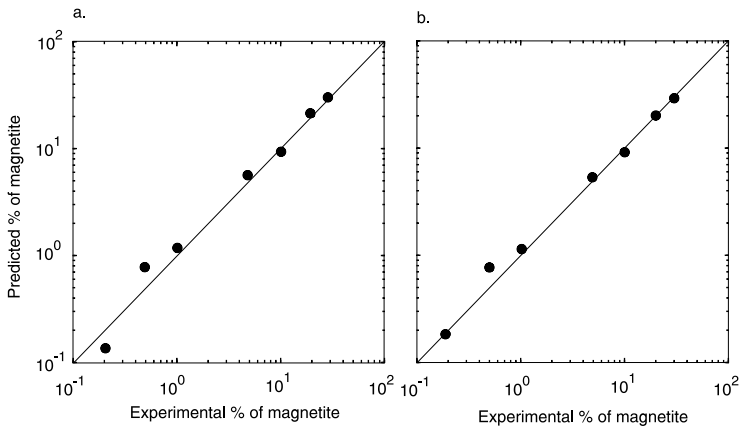

Figure 5.10: Predicted percent of one end-member versus that in the actual mixture, for various values of spacing between particles. The predicted percent was obtained by linearly fitting end-member FORCs to the mixed sample FORC. a: spacing is 5 particle lengths; b: spacing is 0.5 particle length.

the aspect of the FORC diagrams. Because the saturation magnetization of hematite is about 0.5% of that of magnetite, even a very small amount of magnetite in the mixture will be identifiable on the FORC diagram. For example, for a hematite sample containing 0.2% of magnetite, the peak caused by the coercivity of magnetite (much smaller than that of hematite) is already apparent (Fig. 5.9b). The peak caused by hematite fades away compared to the peak caused by magnetite when more and more magnetite is added to the mixture (Fig. 5.9). When there is more than 30% of magnetite in the mixture, only the magnetite is visible on the FORC diagram. All contribution from hematite has disappeared.

The linear additivity was again tested, by fitting the FORCs of each mixture to the FORCs of the endmembers. Linear additivity of the FORC diagrams is verified, regardless of the spacing between particles (Fig. 5.10).

5.3 Experimental measurements of FORC diagrams for magnetic mixtures

5.3.1 Bimodal magnetite mixtures

Samples and experiments

The measurements of magnetite mixtures were carried out using an alternating gradient force magnetometer (AGFM) at the University of Toronto. The maximum field was 0.5 T, enough to saturate magnetite. The three synthetic magnetites used as end-members to make mixtures were Wright magnetite 4000, Wright magnetite 5000, and Wright magnetite W112878. A grain size characterization by scanning electron microscopy gives the following grain sizes (Yu et al., 2002): 0.065±0.036 μm (q=1.48±0.42) for W4000; 0.34±0.21 μm (q=1.65±0.63) for W5000 and 0.44±0.20 μm (q=1.33±0.29) for W112978.

The mixtures were made by combining the end-members in prescribed mass percentages and dispersing them in CaF_2, which is non-magnetic. A significant error in the mass percentages can occur in the process, because some material may be lost when transfering the powders, and also because the mixture may not be perfectly homogeneous. Each mixture was made with two different concentrations in the CaF_2 matrix (10% and 1%), with the intention of studying the effect of interactions on the additivity properties.

I first measured FORC diagrams for each of the end-members. W4000 has a FORC distribution characteristic of small PSD grains, with closed innermost contours and outermost contours that intersect the vertical axis (Fig. 5.11a). The spreading parallel to the vertical axis indicates a fair amount of interaction. W5000 has an SD-like FORC diagram, with most of the contours closing on the diagram, and also some interactions between grains (Fig. 5.11e and Fig. 5.12a). Finally, the FORC distribution of W112978 indicates a PSD grain size, larger than that of W4000 (Fig. 5.12e). Contours diverge away from the vertical axis more than on the FORC diagram of W4000. FORC diagrams for W4000 and W112978 are consistent with their grain size. The SD-like FORC diagram of W5000 might be caused by an elongation ratio relatively large compared to the other two magnetites.

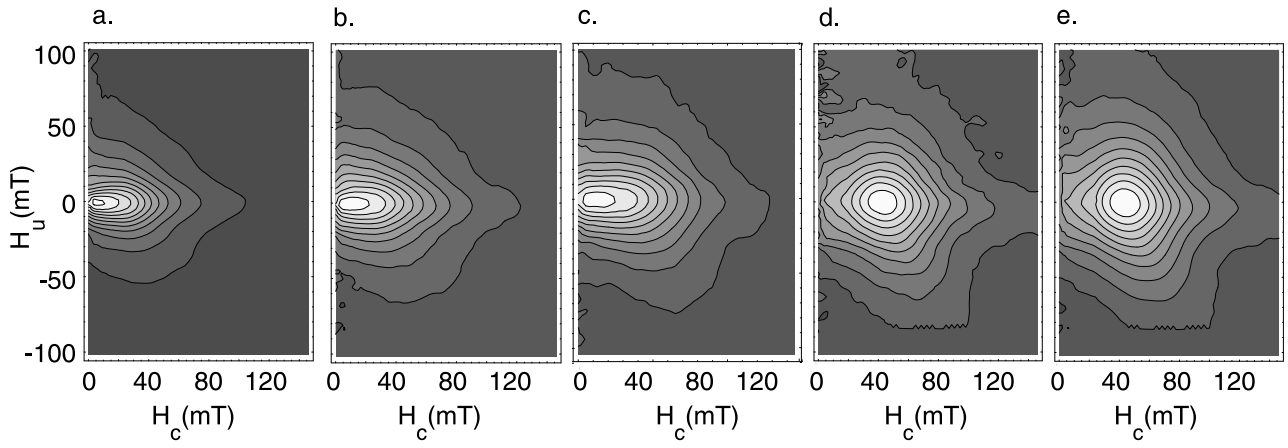

Figure 5.11: Series of FORC diagrams showing mixtures of magnetite W4000 and magnetite W5000. a: 100% W4000; b: 75% W4000, 25% W5000; c: 50% W4000, 50% W5000; d: 25% W4000, 75% W5000; e: 100% W5000

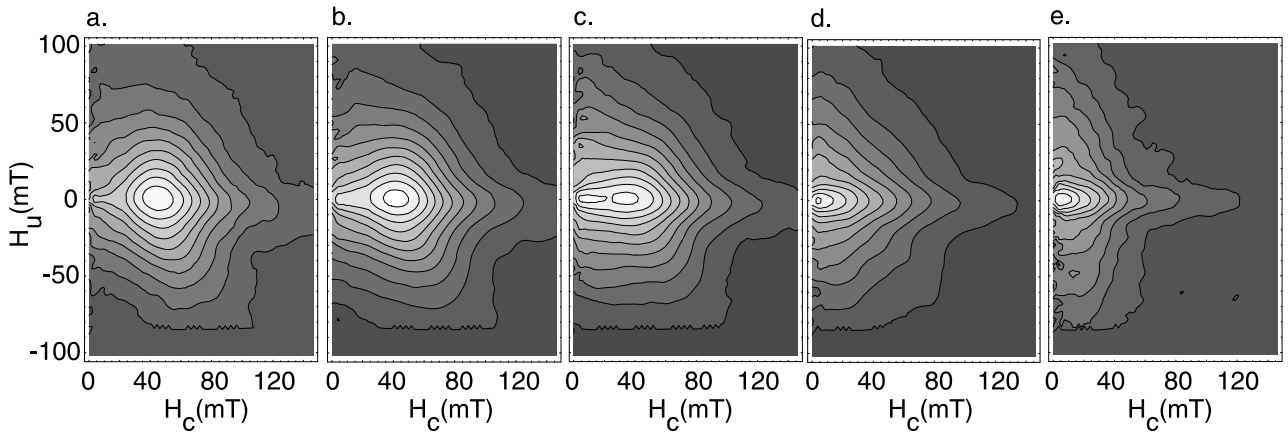

Figure 5.12: Series of FORC diagrams showing mixtures of magnetite W5000 and magnetite 1129178. a: 100% W5000; b: 75% W5000, 25% 112978; c: 50% W5000, 50% 112978; d: 25% W5000, 75% 112978; e: 100% 112978.

FORC distributions- Results

I measured FORC diagrams for mixtures of W4000 and W5000, W4000 and W112978, and W5000 and W112978, each with the two different concentrations. The concentration differences did not have any discernible effect on the FORC distributions. All FORC diagrams showed the same spreading whether 10% or 1% concentration was used. This is probably because it is difficult to make non-interacting samples: the magnetic grains always have a

tendency to cluster together and it is difficult to disperse them uniformly in the CaF_2 matrix.

The FORC distributions for the mixtures of W4000 and W5000 clearly show a progressive shift from a PSD-like pattern to a more SD-like pattern (Fig. 5.11). In particular, the coercivity peak which is close to the vertical axis for W4000, moves towards higher coercivities, and the FORC distribution becomes more and more spread out when W5000 is added to the mixtures. The progressive shift from one end-member to the other is also apparent in the mixtures of W5000 and W112978 (Fig. 5.12). The coercivity contrast between the two endmember is larger than in the mixture of W4000 and W5000. In this case, the two coercivity peaks appear separately on the FORC diagram of the mixture with 50% of each endmember.

Linear additivity

The results of the linear fitting to the end-member FORCs for each of the mixtures are shown in Fig. 5.13. The composition error range is estimated to be $\pm 5\%$. Errors on the predicted proportions are difficult to estimate. The error on the fit is extremely small (3 or 4 orders of magnitude smaller than the fit itself) because of the very large number of data points that are fitted. There is a larger error in the end-members themselves, because of the possible non-homogeneity of the end-members. In order to estimate this error, I re-measured a FORC diagram for a new sample of each end-member and fitted the mixtures to the re-measured end-members. The difference between the two fits is between 2 and 5% for the 10% concentration mixtures, and between 6 and 12% for the 1% concentration mixture. The larger error in the 1% mixture was expected, since it is more difficult to accurately measure proportions and to make a homogeneous sample in a less concentrated mixture. Therefore errors on the fits are estimated to be 5% for the 10% concentration mixtures and 12% for the 1% concentration mixtures.

Most of the proportions predicted from the linear fitting to the endmembers are within 5% of the actual proportion. The predicted proportions of the 10% concentration mixtures fit very well with the actual proportions (all except one point within 7%). The 1% concentration mixtures do not show such a good agreement. This is probably because it is more difficult to do accurate mass measurements when the magnetite is so diluted.

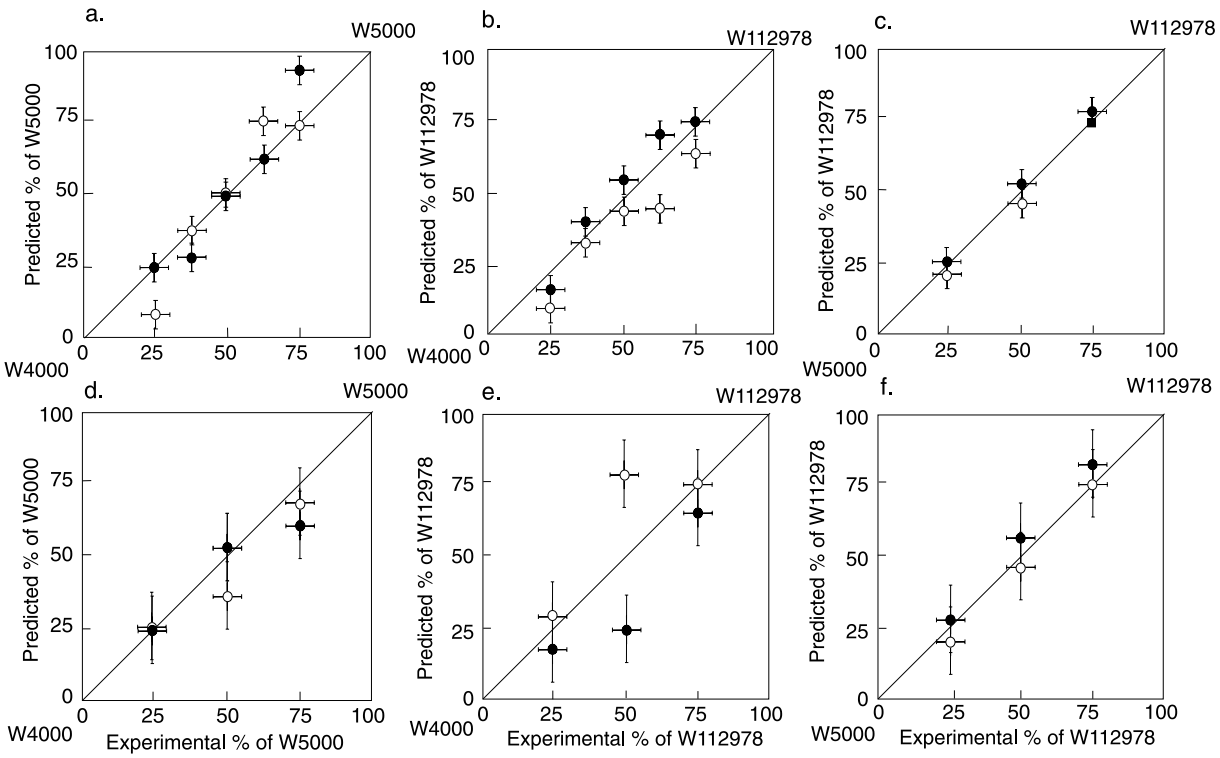

Figure 5.13: Predicted percentage of W5000 or W112978 versus that in the actual sample for all the series. a, b, c: concentration 10%; d, e, f: concentration 1%. The y=x line shows ideal linear addition. The predicted percentages were obtained by linearly fitting: closed circles: end-member FORCs to the mixed sample FORC; open circles: end-member hysteresis loops to the mixed sample hysteresis loops. In d, two sets of FORCs were measured and fitted for 50% of W5000.

In Fig. 5.13 are plotted also predicted compositions inferred from linear additivity of major hysteresis loops. Hysteresis loops of the end-members were re-measured and mixtures re-fitted to the new hysteresis loops, yielding an estimated error in the fits similar to the error on the FORC diagrams fits (5% for the 10% concentration mixtures and 12% for the 1% concentration mixtures). Predicted proportions roughly follow the trend of the actual proportions, but the agreement with the actual proportions is not as good as it was when using FORC diagrams.

5.3.2 Assemblages of magnetite and hematite

FORC diagrams of mixtures of hematite and magnetite were measured at the Institute for Rock Magnetism (University of Minnesota), because the magnet on our AGFM at the University of Toronto is too weak to saturate the hematite. By comparison, I was able to apply up to 1.8 T at the IRM. Hematite was produced by oxidizing synthetic magnetite. Three different kinds of hematite were produced by heating up three magnetite powders: W4000, W5000 and W112978. Magnetite was usually heated at 700° for 4 to 5 hours. Before making the mixtures, I measured SIRM cooling curves of hematite samples from room temperature to 20 K. Only samples showing a clear Morin transition just below 300 K and no trace of a Verwey transition (caused by magnetite that has not been oxidized) were used in the mixtures. Mixtures were not diluted in CaF_2, for several reasons. First, according to the micromagnetic modelling results, interactions are unlikely in mixtures of magnetite and hematite. Second, it is really difficult to estimate the degree of interaction in mixtures diluted in any non-magnetic matrix, because grains will tend to cluster together. Third, there would not be any room for CaF_2 in the mixture because a lot of hematite is needed to be detected on the FORC diagram.

Figure 5.14 shows an example of FORC diagrams for a mixture of hematite and magnetite, as well as the FORC diagrams for the end-members. The FORC distribution of hematite is characterized by a broad peak centered at a high coercivity (around 400 mT). This pattern is consistent with other measurements of FORC diagrams on hematite (Muxworthy et al., 2003c; Roth et al, 2003). More contours had to be plotted on the FORC diagrams in order to see the pattern created by the hematite in the mixtures. The FORC diagrams shown on Fig. 5.14c-e (mixtures with respectively 4.6, 8.4 and 11.5% magnetite) contain three times more contours than the FORC diagrams on Fig. 5.14a-b and f, and the hematite peak is barely visible. The hematite would not be noticed if the number of contours was not dramatically increased. However, the presence of hematite would not be detected at all if only hysteresis loops were measured. FORC diagrams are a better tool than hysteresis loops for detecting hematite mixed with magnetite, provided the concentration of magnetite is not greater than about 12% and if FORC diagrams are plotted with a very large number of

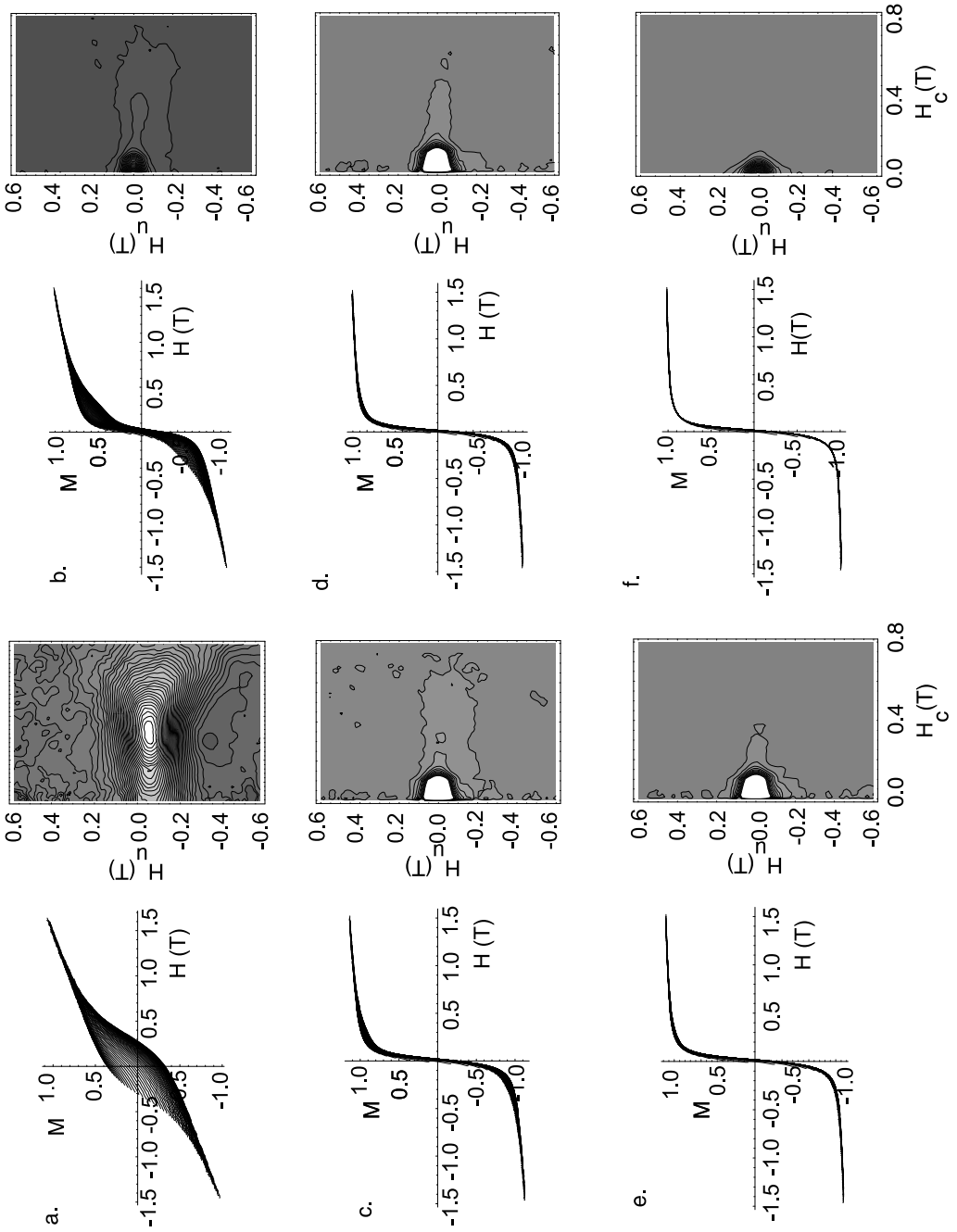

Figure 5.14: FORCs (left column) and FORC diagrams (right column) of a mixture of W4000 magnetite and hematite made from W4000 magnetite. a: 100% hematite; b: 99% hematite, 1% magnetite; c: 95.4% hematite, 4.6% magnetite, d: 91.6% hematite, 8.4% magnetite; e: 88.5% hematite, 11.5% magnetite; f: 100%magnetite

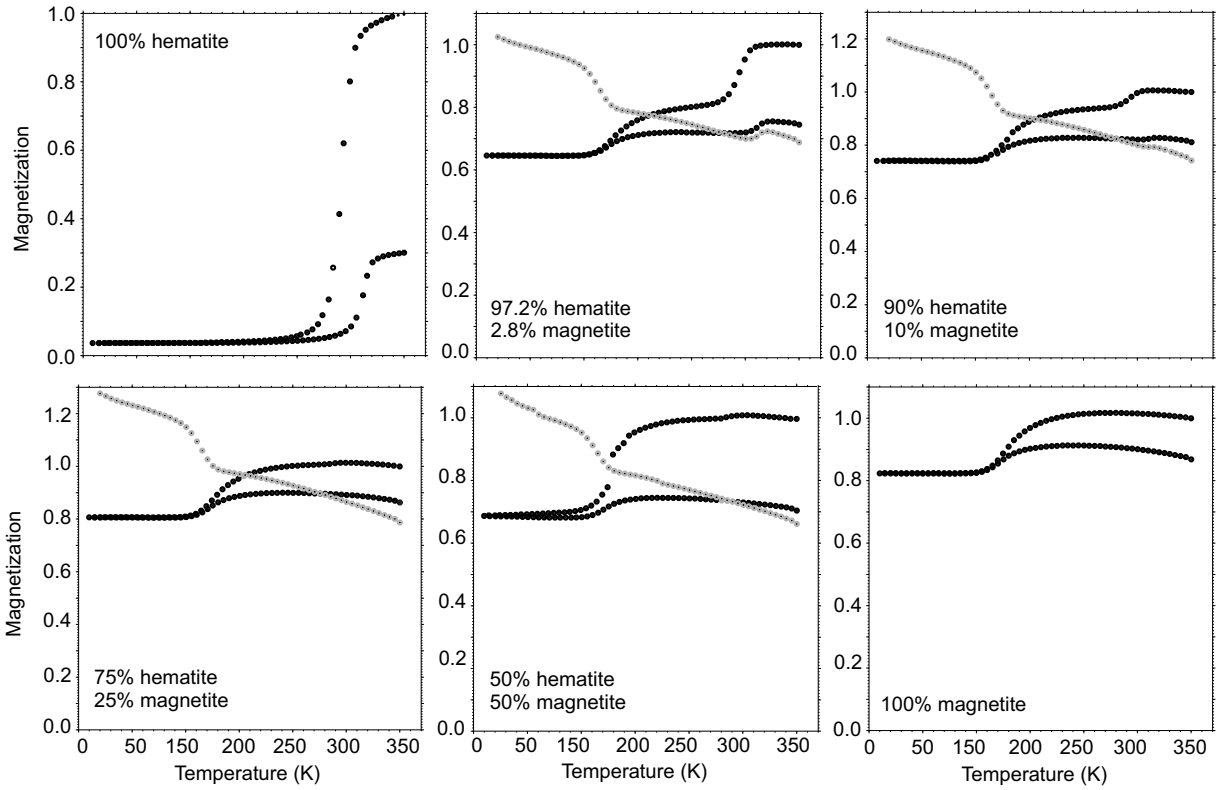

Figure 5.15: Temperature dependence of saturation remanence (SIRM) produced by a 2.5 T field. The grey circles show the zero-field SIRM warming curve from 20 K to 300 K. The black circles show the zero-field cooling (300 K to 20 K) and warming curves for SIRM produced at 300 K.

contours.

I measured cooling and warming curves of SIRM for some of the mixtures (Fig. 5.15). The Morin transition around -15°C is caused by hematite, whereas the Verwey transition and the isotropic point at about 130 K indicate the presence of magnetite. In mixtures of magnetite and hematite, both the Morin transition and the Verwey transition should be present. When magnetite is added to the original hematite sample, the Verwey transition appears in both the low-temperature warming curve of SIRM (20 K) and the low-temperature cooling and warming of SIRM (300 K). The Morin transition is still very clear (in particular in the SIRM (300 K) cooling curve) even when magnetite constitutes as much as 10% of the mixture. If more magnetite is added to the mixture, the Morin transition can still be noticed by a very slight hump in the SIRM (300 K) cooling curve (e.g. 50-50 mixture).

5.4 Discussion

It is well accepted that non-interacting mixtures have linearly additive magnetizations. For example, Carter-Stliglitz et al. (2001) argue that their experiments were unaffected by interactions because they used components dispersed in a magnetically clean diamagnetic matrix. Lees (1997) carried out another set of experiments on the additivity of magnetization in mixtures and demonstrated non-linearity of magnetization as a function of mixing ratio for many of the samples. However, her results are not necessarily in conflict with my results showing linear additivity even for interacting mixtures. One factor that could have caused the non-linear behaviour in Lees' case is the change in interaction state between the pure end-members and the mixtures: the end-members likely suffered from interaction effects before the dispersion in the mixture; once the end-members were mixed, the interaction effects were reduced. In my case, the mixture samples and the end-member samples were prepared exactly in the same way, with the same dispersion, so I expect that the interaction state stays the same when the mixing ratio is increased. This might explain why linear additivity is still observed in my measurements, even when magnetic grain concentration is as high as 10%. It is also worth noting that it is very difficult to know exactly the interaction state in a mixture. In my case I only assumed that the mixtures used in the measurements are interacting, based on the spread on the H_u axis and the relatively high concentration. It might also be possible that the interactions present in the experimental samples were not high enough to compromise linear additivity. Even though results from the modelling and the measurements are consistent, it has to be kept in mind that in the modelling I studied assemblages of SD grains, whereas the grain size of samples measured is much more diverse and goes from $\sim$ SD to PSD. Modelling arrays of particles larger than SD would require huge resolutions and therefore computer power that is not yet available, so only assemblages of SD grains were modelled.

Strictly speaking, interacting mixtures are non-linearly additive, as proved by the visible differences between predicted and measured FORC diagrams. However, fitting the FORCs of the mixtures to the FORCs of the end-members usually gives te expected proportions of end-members. Besides the possibility of predicting end-member proportions, visually observable

differences in the FORC diagrams have potential applications in detecting interactions in mixtures.

In any case (interacting or non-interacting mixtures), FORC diagrams can predict mixing ratios better than major hysteresis curves. Using the entire hysteresis curve, Carter-Stiglitz et al. (2001) designed a singular-value decomposition to solve for the various concentrations of the magnetic phases in mixtures. They proved the efficiency of the method with several examples. The drawback of their technique is that it requires complete hysteresis loops together with low-temperature SIRM curves. In contrast, FORC diagrams are faster to acquire compared to low-temperature SIRM curves, and also provide much more information.

The linear additivity of FORC diagrams of hematite/magnetite mixtures is not a surprise, because in mixtures containing only one hard magnetic mineral (hematite in my case), which has a small M_s compared to magnetite and large magnetocrystalline anisotropy, there are negligible magnetostatic interactions between the phases. Therefore even concentrated mixtures will have linearly additive magnetizations, and hence FORC distributions. However, both the models and the measurements suggest that FORC diagram measurements are not a very suitable method for identifying hematite in mixtures dominated by magnetite, or probably any other soft magnetic mineral. High-field low-temperature remanence methods are much more appropriate. However, FORC diagrams work relatively well in identifying small amounts of soft magnetic minerals in a matrix of hard magnetic mineral, as could be the case in red beds, for example. The maximum concentration of magnetite that still permits hematite to be detected is $\approx 12\%$.

My study complements the work of Muxworthy et al. (2003c) by verifying the linear additivity of FORC diagrams with micromagnetic modelling and confirming the experimental linear additivity for non-interacting mixtures. My results on interacting mixtures disagree with Muxworthy et al's results: for one of the mixtures, they found a difference of 30% between predicted and actual end-member proportion. However, their measurements of interacting bimodal magnetite mixtures were for only two mixtures, whereas my study is much more detailed.

Together, these two studies open the possibility of unravelling magnetic mixtures using FORC diagrams. This could be applied to quantitative determination of the contributions

of the rock magnetic components in a sample, and could have potential applications in many studies of magnetism in rocks.

Chapter 6

How is a FORC diagram different from a Preisach diagram?

6.1 Introduction

Preisach and FORC diagrams have been introduced in Section 1.2. Since FORC diagrams have started to be used in rock magnetism, there has been much debate on whether FORC and Preisach diagrams are equivalent. Dunlop et al. (1990) measured Preisach diagrams on magnetite samples ranging in size from SD to large MD. The patterns observed as a function of size match patterns usually obtained for FORC diagrams. SD and small PSD samples have contours that are closed ovals. Distributions for large MD grains are characterized by broadly spreading contours almost perpendicular to the diagonal $a = -b$. PSD grains have closed contours linked to the diagonal that peak away from the origin. However, the procedures used to measure FORC and Preisach diagrams are somewhat different. The initial state of the sample plays a large role in the final Preisach diagram. Dunlop et al. (1990) used AF or DC demagnetized states. An SIRM initial state would be closer to the procedure to measure FORC diagrams. When measuring a Preisach diagram, successive positive and negative fields are applied, increasing in steps to saturation, and resulting IRMs are measured. $F(a, b)$ can be worked out in squares on a grid. The magnetizations measured in a Preisach diagram are remanent magnetizations only. On the contrary, remanent and induced magnetizations are measured in hysteresis loops and therefore FORC diagrams.

6.2 Measurements of FORC and Preisach diagrams

I measured FORC and Preisach diagrams, using an SIRM state as initial state, for a selection of synthetic and natural samples. The resolution varied between 20×20 points and 30×30 points for the Preisach diagrams. This resolution is much smaller than that of a FORC diagram, therefore in general my Preisach diagrams show much less detail than the FORC diagrams. The range of values taken by the Preisach distribution is usually small, and the signal to noise ratio is fairly high, typically 10/1. Some smoothing is necessary for a comparison with FORC diagrams. I used the same smoothing method as is used to produce FORC diagrams by applying a running average in two directions. When the SF is increased, the distribution on the edges of the diagram is truncated. Since a Preisach diagram has many fewer points than a FORC diagram, I was limited to small SF (2 or 3) so as not to reduce the number of data too much. I used SF=2 for most of the Preisach diagrams, corresponding to an average of 9 points on the diagram: the central point plus four nearest neighbours plus four nearest on the diagonal.

6.2.1 W5000 magnetite

The Preisach distribution for W5000 is fairly flat, and quite noisy. The resolution is 23×23 points. However, there is a very good agreement with the FORC diagram at identical SF (Fig. 6.1). The main peak occurs around 45 mT on the Preisach diagram, which is almost the same as on the FORC diagram (∼43 mT). The two distributions are roughly symmetrical, centered on the horizontal axis, and the spreading along the horizontal axis is also in good agreement between the two diagrams: the FWHM along the horizontal axis is 54 mT on the Preisach diagram and 60 mT on the FORC diagram. With a SF of 2, the main peak shows more noise on the FORC diagram than on the Preisach diagram, but the Preisach diagram is noisier on the edges.

6.2.2 Basalt sample from Detroit Seamount

The FORC and Preisach diagrams again show very similar characteristics (Fig. 6.2), even though the resolution of the Preisach diagram is only 15×15 points. On both diagrams, the

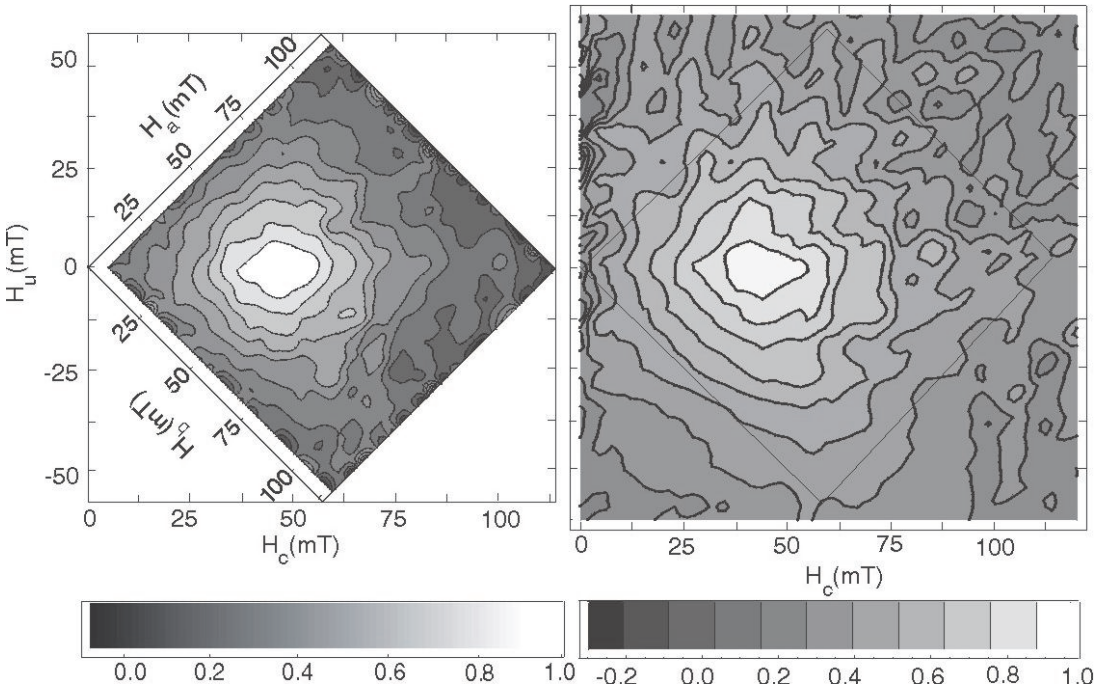

Figure 6.1: Preisach diagram (left) and FORC diagram (right) for W5000. Both diagrams are at the same scale.

whole distribution slants below the H_c axis. Both distributions are also asymmetric in similar ways. Spreading along the H_u and H_c axes is fairly consistent (7.9 mT for Preisach diagram, 7.7 mT for the FORC diagram along the H_c axis; 5.2 mT for the Preisach diagram, 4.7 mT for the FORC diagram along the H_u axis). However, the contours close to the H_u axis are only visible on the FORC diagram, and not at all on the Preisach diagram. I also measured a Preisach diagram with a higher resolution close to the origin. The contours apparent on the FORC diagram close to the H_u axis are still not visible on this high-resolution Preisach diagram, because the region of the FORC contours is still not covered by the Preisach distribution.

6.2.3 Basalt sample from Nintoku seamount

The noise level (with SF=2) is quite high, especially on the FORC diagram (Fig. 6.3). Nevertheless, the two diagrams show good similarity. The Preisach diagram contains 20×20 points. The main peak is located at the same place (25 mT for the Preisach diagram, 23

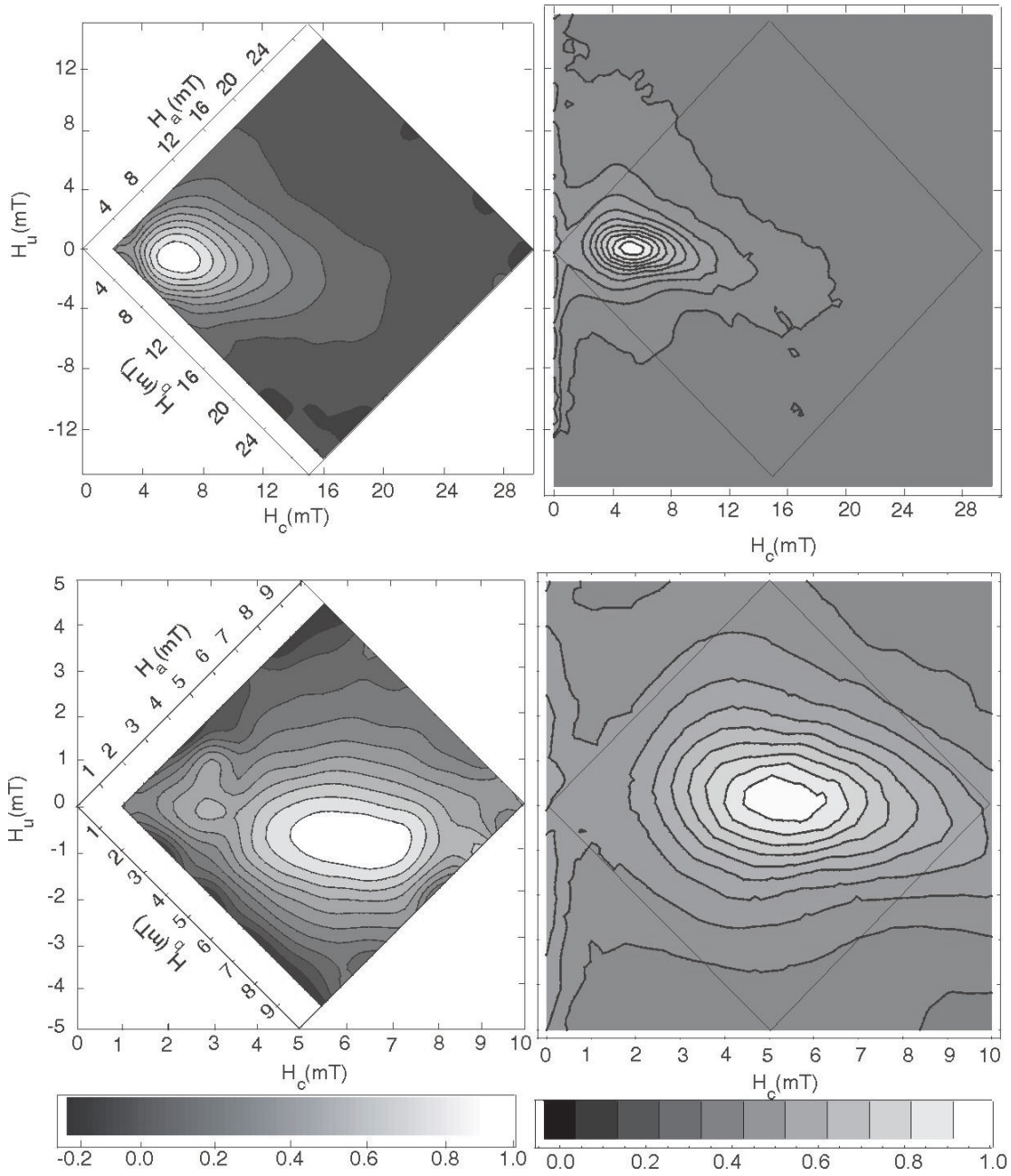

Figure 6.2: Preisach diagram (left) and FORC diagram (right) for a basalt sample from Detroit seamount (ODP ID: 197-1203A-47R4-50-52 cm). Both diagrams are at the same scale.

mT for the FORC diagram) and the spreading along the H_c axis is also very similar on both diagrams (FWHM is 25 mT on the Preisach diagram, 24 mT on the FORC diagram). On the Preisach diagram, the distribution falls to zero along the horizontal axes (according to the FORC axis system), whereas the FORC distribution does not show such a sharp decrease.

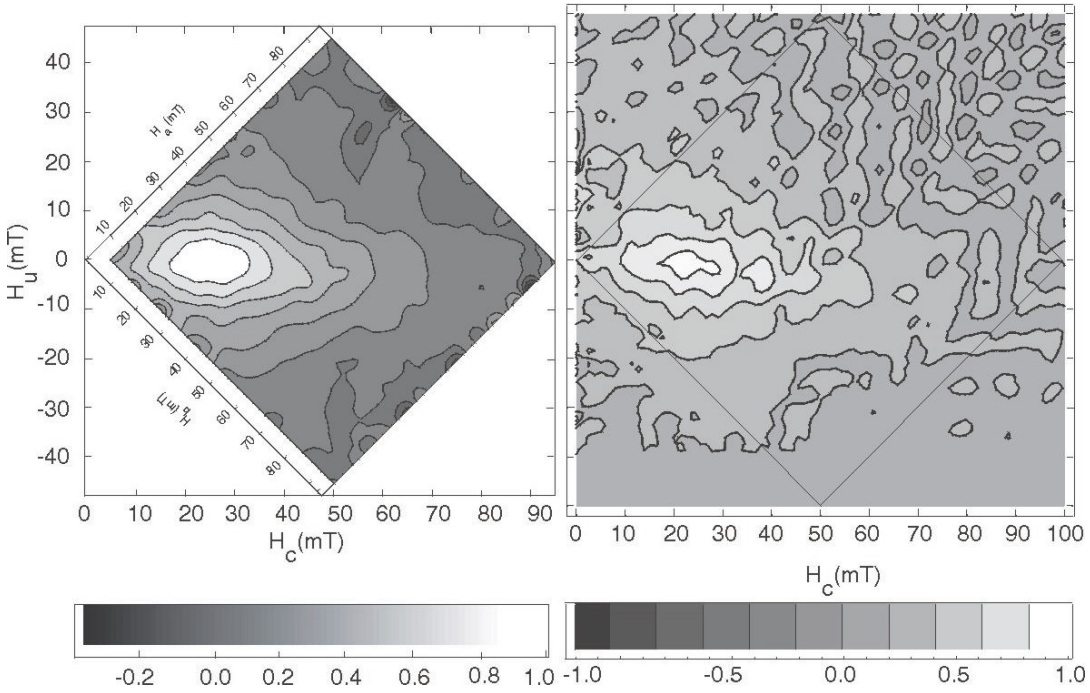

Figure 6.3: Preisach diagram (left) and FORC diagram (right) for a basalt sample from Nintoku seamount (ODP ID: 197-1205A-41R5-66-68 cm). Both diagrams are at the same scale.

6.2.4 Basalt sample from Koko seamount

The FORC diagram is characteristic of non-interacting SD magnetic grains: the coercivity peak is well separated from the H_u axis and the spreading along the H_u axis is very limited (Fig. 6.4). The Preisach diagram has the same features. Spread of the distribution along the H_c axis is observed in both diagrams. The FWHM along the H_u axis is 13.7 mT for the Preisach diagram and around 16 mT for the FORC diagram. The resolution of this Preisach diagram is quite high (30×30 points). This particular example shows very good agreement between the FORC and the Preisach diagrams.

6.2.5 Another basalt sample from Koko seamount

The FORC diagram of this sample is characteristic of PSD grains. A Preisach diagram with a low resolution (10×10 points) only shows a maximum of the distribution close to the origin of the diagram (Fig. 6.5). When the resolution is increased closer to the origin with a second

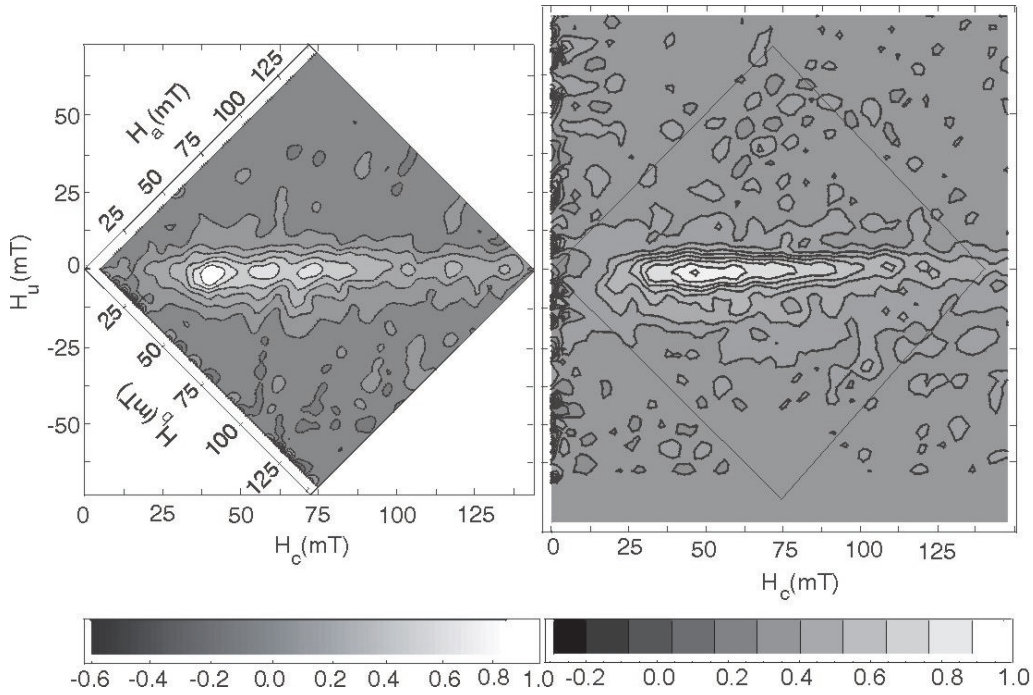

Figure 6.4: Preisach diagram (left) and FORC diagram (right) for a basalt sample from Koko semount (ODP ID: 197-32R2-117-119 cm). Both diagrams are at the same scale.

set of measurements, the contours are closed, in disagreement with the FORC diagram.

6.2.6 Subaerial basalt

This sample is from a basaltic lava flow from Poker Jim Ridge (Oregon), where an excursion of the magnetic field was recorded during the Miocene (Goldstein et al., 1969, Mankinen et al., 1987). Low-temperature measurements revealed the presence of almost pure magnetite as the carrier of magnetization in this sample. Both the Preisach and the FORC diagrams are noisy, but again they show essentially the same features: a coercivity peak characteristic of small PSD magnetic carriers centered at 25 mT (both the FORC and the Preisach diagram), and a similar FWHM parallel to the H_u axis of 29.4 mT on the Preisach diagram and 26 mT on the Preisach diagram. The only significant difference between the two diagrams is the presence of more closed contours on the Preisach diagram than on the FORC diagram.

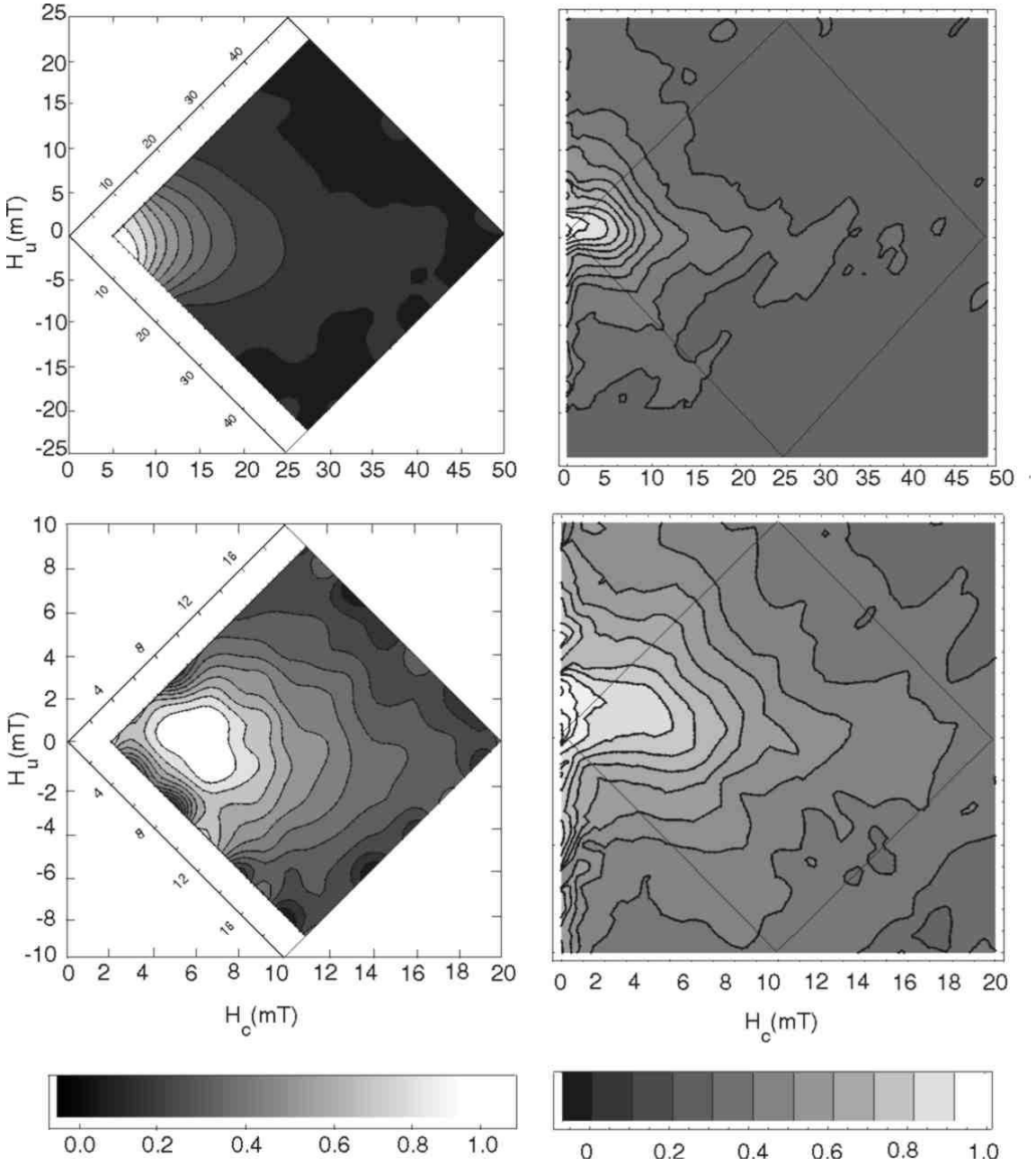

Figure 6.5: Preisach diagram (left) and FORC diagram (right) for a basalt sample from Koko seamount (ODP ID: 197-1206A-41R1-35-37 cm). Left and right diagrams in each pair are at the same scale.

6.2.7 Elongated SD maghemite

The Preisach distribution contains 18×18 points. With an SF of 2, the agreement between the FORC and the Preisach diagrams is excellent (Fig. 6.7). Again, the main peak occurs

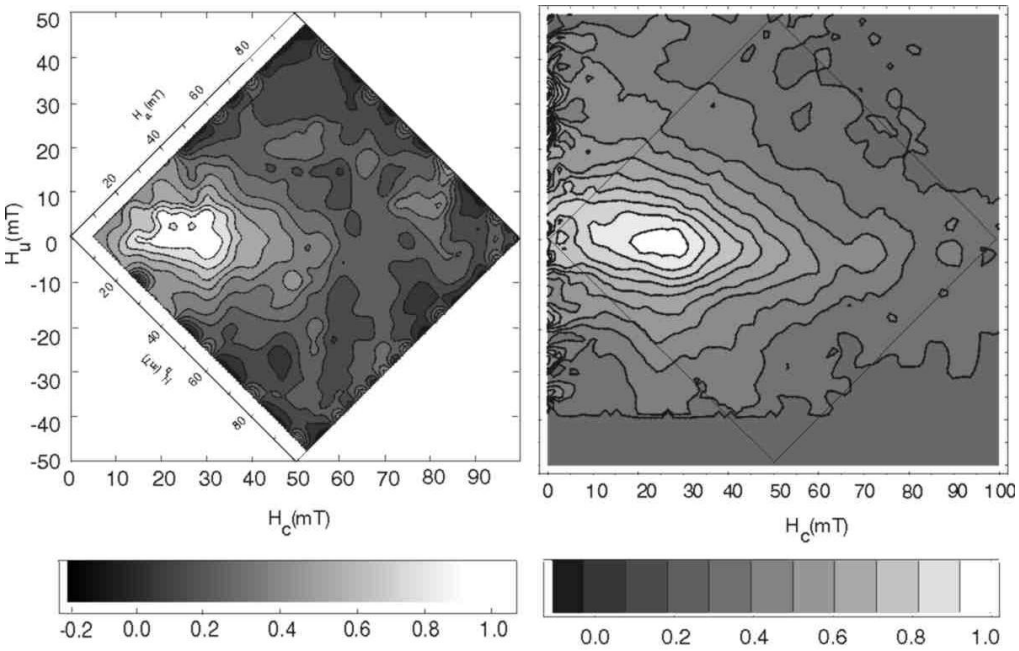

Figure 6.6: Preisach diagram (left) and FORC diagram (right) for subaerial basalt from Poker Jim Ridge. Both diagrams are at the same scale.

at the same H_c value on the Preisach and FORC diagrams (45 mT). The noise levels are also very similar. The two lobes in the FORC distribution (one extending to high H_c and the other one extending to negative H_u) are also present in the Preisach distribution. The FWHM of the main peak along the H_c axis is 25.8 mT on the Preisach diagram and 24.5 mT on the FORC diagram. Along the H_u axis, the FWHM is 21.5 mT on the Preisach diagram and 21 mT on the FORC diagram.

6.3 Discussion

All the Preisach diagrams except the second sample from Koko seamount are in very good agreement with the general features seen on the corresponding FORC diagrams, such as the amount of spreading along the H_u axis, or the coercivity field at which the distribution peaks. Other major features, such as lobes along H_u or H_c axes (in the case of the maghemite sample, for example) are also similarily represented on both diagrams. These results support

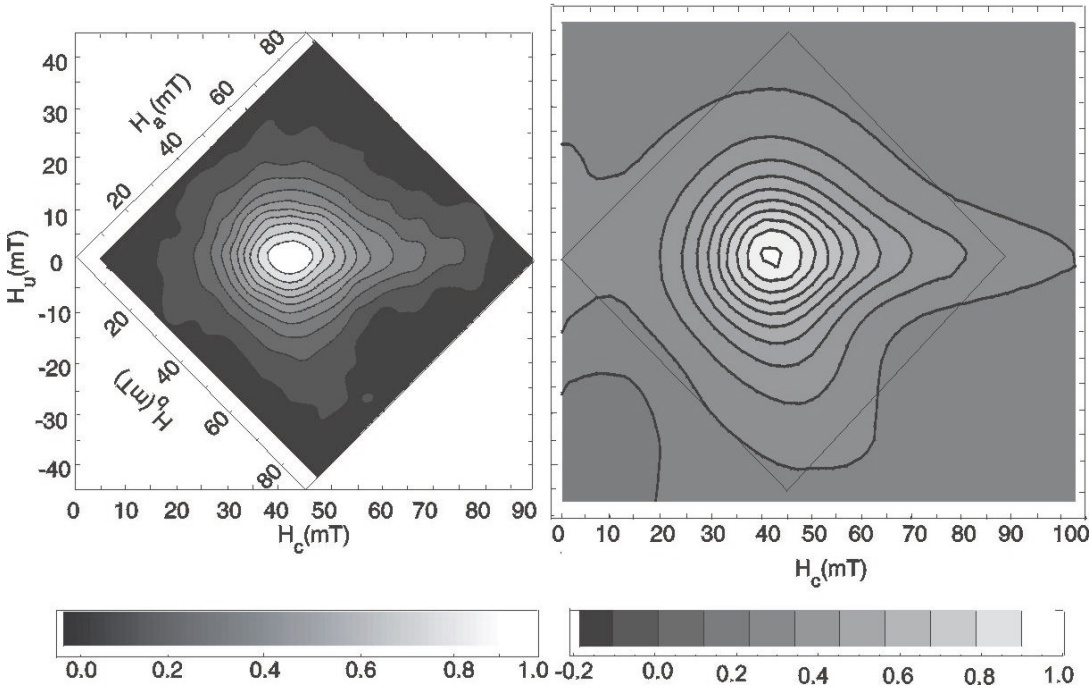

Figure 6.7: Preisach diagram (left) and FORC diagram (right) for the elongated maghemite sample of Chap. 5. Both diagrams are at the same scale.

the idea that Preisach and FORC diagrams give basically the same information.

However, in some cases FORC diagrams can give more information than Preisach diagrams. This is due to the fact that a Preisach diagram has a much lower resolution than a FORC diagram in this study. FORC diagrams contain a few thousand data points (in my case between 6000 and 8000), whereas Preisach diagrams are usually constructed with a few hundreds of points (between 200 and 900 in this study, and rarely more than 400). Therefore Preisach diagrams contain about an order of magnitude less information than a FORC diagram. This could be improved if the Preisach diagram measurement procedure were automated.

Another consequence of the poorer resolution of the Preisach diagram compared to a FORC diagram is that I could not apply as much smoothing on a Preisach diagram. Each time SF is increased by 1, two points are lost on the edges of the diagram. For example, with a resolution of 15$\times$ 15 points (225 points), 56 points are lost when SF=2, and 104 when SF=3. This also limits the interpretation of Preisach diagrams.

Features that are close to the H_u axis give some problems on a Preisach diagram, because the remanent region excludes these areas. An example can be seen in Fig. 6.2, where the spread of some of the contours almost parallel to the H_u axis when H_c is very low is only visible on the FORC diagram, and not at all on the Preisach diagram.

It should also be kept in mind that there are several ways of measuring Preisach diagrams. The method used here is close to the method described by Dunlop et al. (1990). However Zelinka et al. (1987) used a method of measuring Preisach diagram which is identical to the FORC method, but they still call it a Preisach diagram. So it could be argued that FORC diagrams are actually one way of measuring a Preisach diagram.

Considering that Preisach diagrams as measured in this chapter represent only the remanent part of the magnetization, it is a little surprising that the agreement between the FORC and Preisach diagrams is so good. The current measuring procedure used to make a FORC diagram does not allow the separation of FORC diagrams into a remanent and an induced part, because the descending major loop and each of the first-order reversal curves are not symmetrically measured. The major hysteresis loops always start from saturation, but the FORCs usually depart from a non-saturating field. The solution would be to modify the FORC measurement protocol by starting from a demagnetized state, cycling between $+H_a$, $-H_a$ and $+H_a$, step up to a larger H_a and cycle again. This protocol would give symmetric FORC distributions.

Chapter 7

Conclusion

7.1 Summary of the results

In the first part of my PhD program, I carried out paleointensity determinations by the Thellier method on a set of samples from three of the Emperor seamounts. Thermomagnetic curves and low-temperature behavior of SIRM were also measured in order to identify the carriers of the magnetization and to assess the reliability of the magnetic recording in the successful samples. A first important result is that the paleolatitudes determined from the thermal demagnetization of three lava flows carried out during the Thellier experiment are different from the present-day latitude of Hawaii and support the hypothesis of a moving hotspot. They are in agreement with the values measured by Tarduno et al. (2003). From the thermomagnetic curves, samples show a wide variety of titanium content between seamounts and between lava flows within the same seamount. Low-temperature oxidation or maghemitization is quite frequent in these submarine samples, but did not occur in a homogeneous way in the lava flows. Only four samples out of almost one hundred, all from Nintoku seamount (56 Myr), ultimately gave reliable paleointensity results. The other samples failed the experiment mostly because of mineralogical changes occuring during the heating steps, or because they were maghemitized, which would give paleointensity values that are too low. The final four VADM values are all higher than the average VADM for the period 0.3-300 Ma, but within the error range.

The second part of my program deals with FORC diagrams, a powerful new tool in rock

magnetism that could ultimately have applications in preselection of samples for paleointensity work. The theoretical aspects of FORC diagrams are not well understood, so my work on FORC diagrams was centered on testing interpretations of FORC diagrams by modelling and measurements.

First, I carried out micromagnetic modelling of FORC diagrams, in order to try to explain some of the observed features. I found that isolated elongated SD particles show a single positive peak centered at H_c, H_u=0. Isolated elongated PSD particles have complex FORC distributions with several secondary positive and negative peaks, caused by intermediate vortex structures. Arrays of interacting SD particles with uniaxial shape anisotropy and aligned axes also display several peaks in the FORC distribution caused by the several minor branches on the reversal curves. Arrays of non-interacting particles do not show these peaks but only a single peak centered at zero on the H_u axis and at the average coercive field of the assemblage on the H_c axis. Splitting of the central peak when particles begin interacting might explain the vertical spread observed on FORC diagrams of natural interacting samples as an effect of superposition of multiple peaks due to the random orientation and varying spacing of a large number of grains. I did not observe any significant changes in the hysteresis parameters $M_{\rm rs}/M_{\rm s}$ and $H_{\rm c}$ that would indicate the interaction state. In the case of arrays of SD particles with uniaxial anisotropy and aligned axes, the presence of multiple peaks on the FORC diagram is a much better indicator of interactions than variations in hysteresis parameters.

The presence of multiple peaks could be a manifestation of intermediate vortex structures in PSD grains as well as of interactions in arrays. In a real sample where anisotropy axes are different for each grain and where grains have a distribution of coercivities, the effects of PSD grains will be different from the effects of interactions. For example, the coercivity peak will be close to the origin of the FORC diagram and fewer contours will be closed. According to my model, I suggest that the spread observed on the H_u axis in natural samples with interactions is caused by the superposition of split peaks.

The next step was to measure FORC diagrams at low and high temperatures on a well-characterized sample of acicular SD maghemite in order to test some predicted properties of FORC diagrams. FORC distributions at different temperatures are quite similar except

close to T_C. A quasi-circular peak, centered on the H_c axis and well separated from the H_u axis, gradually contracts with increasing T, more or less in proportion to $M_s(T)$. Because $M_s(T)$ changes very little between 20 K and 300 K, the low-T FORC distributions are almost identical. The outer contours of the distribution are not symmetrical but form lobes extending to higher H_c and to negative H_u. These asymmetries grow at high T.

A profile f(H_c) along the H_c axis through the peak of the FORC distribution $\rho(H_a, H_b)$ has the properties of a cumulative microcoercivity distribution, e.g., an AF demagnetization curve or an IRM acquisition curve. The match is quite close between these experimental curves and f(H_c) determined from the room-temperature FORC distribution of this sample. Furthermore a stack of such f(H_c) spectra from FORC distributions at different T matches very well, in general shape and migration of the initial plateau in the spectrum, measured high-T AF demagnetization curves of saturation remanence for SD magnetites. Finally, the median and peak fields from f(H_c) have approximately the same temperature variation as the measured bulk coercive force H_C. These tests make the equivalence of H_c in the FORC diagram and microcoercivity H_c as measured in standard rock magnetic experiments almost a certainty. It is less easy to prove that g(H_u) profiled parallel to the H_u axis through the peak of $\rho(H_a, H_b)$ represents the distribution of interaction fields in the sample. Interactions on all scales (whole-sample and between-particle), like dipole interactions, are magnetostatic and the interaction field H_i should be $\propto M_s$. The observed T variation was indeed $\propto M_s(T)$ (Fig. 4.7, inset), confirming the equivalence of H_u and H_i.

I then investigated the effect of mixtures of magnetic minerals on FORC diagrams and in which cases FORC diagrams would be linearly additive, using both micromagnetic modelling and experiments.

I modelled FORC diagrams for different assemblages of SD magnetite with a bimodal distribution of coercivities, and various spacings between grains in each assemblage. When fitting FORC diagrams of mixtures to the endmember FORC diagrams, I find that linear additivity is well obeyed: predicted mixing ratios are within 7% of the actual mixing ratios. Even when the grains are interacting within the mixture, FORC diagrams are still linearly additive. Experimental measurements of FORC diagrams support this conclusion. Bimodal mixtures of magnetite (SD+PSD) have FORC diagrams that are linearly additive, regardless

of the magnetite concentration of the sample (10% or 1%). I also modelled FORC diagrams for mixtures of SD magnetite and SD hematite. Again, linear additivity of the two end-members holds, whatever the spacing between particles. However, the very small M_s of hematite compared to that of magnetite makes it difficult to detect a contribution from hematite on a FORC diagram, unless it composes at least 88% of the mixture, and unless the number of contours plotted on the FORC diagram is increased. FORC diagrams are not well suited to the detection of weakly magnetic minerals mixed with strongly magnetic minerals. SIRM warming and cooling curves are much more efficient in detecting weakly magnetic minerals.

The results for magnetite mixtures are promising for achieving a better quantitative interpretation of FORC diagrams as a tool to identify magnetic minerals in a sample. Applications are numerous and cover a wide range of disciplines, from paleomagnetism to environmental magnetism.

The last aspect of the FORC diagrams that I investigated was finding the similarities and differences between FORC and Preisach diagrams. I measured FORC and Preisach diagrams for six samples (one synthetic magnetite, one synthetic maghemite and four basalt samples from three different seamounts). Even though the resolution of a Preisach diagram is about an order of magnitude less than that of a FORC diagram, there is a good agreement in almost all cases between the two diagrams. The main results extracted from such diagrams (the coercivity of the distribution peak and the spreading of the distribution peak along the H_c and H_u axes) are very consistent. There are, however, some differences between the two diagrams. One difficulty is that the level of smoothing cannot be as high on a Preisach diagram without sacrificing a significant fraction of the data points. Contours that are very close to the H_u axis are problematic for Preisach diagrams. In two examples where some important features of the FORC distribution were close to the H_u axis, Preisach diagrams failed to image these features and showed closed contours instead.

One important difference between FORC and Preisach diagrams is that Preisach diagrams only measure the remanent part of the magnetization, whereas FORC diagrams measure both the remanent and the induced parts. One way to separate the induced from the remanent part is to use the descending part of the major hysteresis loop as a first approximation to

the upper branch of each FORC. When such a decomposition was made for the six measured samples, the FORC diagrams proved to be very similar to each other, but that might be because this method does not fully separate the induced from the remanent parts. These results suggest that, as a first approximation, FORC and Preisach diagrams give the same distributions. However, the level of detail and the shorter measurement time offered by FORC diagrams make them more attractive to use than Preisach diagrams.

7.2 Future work

Measuring the ancient intensity of the geomagnetic field is crucially important for understanding long-term evolution of the Earth's core and constraining models of the geomagnetic dynamo. Paleointensity data are needed to understand how the geomagnetic field reverses polarity, geomagnetic excursions, secular variation, and to constrain models for field generation. My paleointensity determinations using basalts from the Emperor Seamounts added one data point for the Cretaceous-Tertiary paleointensity variation, but more data are needed in this poorly studied time interval.

One reason for the small number of paleointensity data is the large failure rate inherent to the Thellier-Thellier method. My extensive study of several theoretical aspects of FORC diagrams verifies that patterns along the H_u axis are created by interaction fields and patterns along the H_c axis represent microcoercivity distributions. My study also showed that FORC diagrams give more information than Preisach diagrams. In this context, FORC diagrams could be helpful for pre-selecting successful samples. The reasons why paleointensity experiments fail, other than mineralogical alteration, are the presence of interactions and the presence of MD grains. These should both be detectable by the FORC method. Such a screening protocol based on FORC diagrams could increase the rate of success of paleointensity studies and thus the number of data. The next step should be a study measuring FORC diagrams for a wide range of samples that succeeded or failed the Thellier-Thellier experiment. Looking for evidence on the FORC diagrams of magnetic properties that caused the success or failure of the experiment would help establish quantitative limits for sample selection-rejection criteria.

Finally, my models and experimental measurements of FORC diagrams of magnetic mixtures prove the linear additivity of FORCs in the case of bimodal mixtures of magnetite and mixtures of hematite and magnetite, opening the possibility of unravelling magnetic mixtures through FORC measurements. However, more measurements are needed to thoroughly validate the linear additivity of FORC diagrams and their use in identifying magnetic minerals in an assemblage. In particular, it would be interesting to investigate the linear additivity of FORC diagrams for samples containing MD or large PSD grains, and for mixtures of different magnetic minerals having comparable M_s values. There are many possible applications for such a method of identifying magnetic minerals using FORC diagrams, paleomagnetism, rock magnetism, and environmental magnetism.

Bibliography

Antretter, M., Steinberger, B., Heider, F., & Soffel, H., 2002. Paleolatitudes of the Kerguelen hotspot: new paleomagnetic results and dynamic modeling. *Earth Planet. Sci. Lett.*, **203**, 635–650.

Atwater, T., 1989. Plate tectonic history of the northeast Pacific and western North America, in *The Geology of North America, vol N, The eastern Pacific Ocean and Hawaii, ed E.L. Winterer, D.M. Hussong and R.W. Decker*, 21–72.

Baag, C., Helsley, E., Xu, S., & Lienert, B.R., 1995. Deflection of paleomagnetic directions due to magnetization of the underlying terrain. *J. Geophy. Res.*, **100**, 10013–10027.

Banerjee, S.K., 1971. New grain size limits for palaeomagnetic stability in hematite, *Nature Phys. Sci.*, **232**, 15-16.

Barton, E., 1995. International Geomagnetic reference Field, 1995 revision presented by IAGA Reference V, working group 8. *Phys. Earth Planet. Inter.*, **14**, 904–908.

Blakemore, R.P., 1975. Magnetotactic bacteria, *Science*, **190**, 377-379.

Bloemendal, J., Barton, C.E., & Radhakrishnamurthy, C., 1985. Correlation between Rayleigh loops and frequency-dependent and quadrature susceptibility, *J. Geophys. Res.*, **90**, 8789–8792.

Brown, W.F.Jr., 1963. *Micromagnetics*. 143pp, John Wiley, New York.

Carmichael, C.M., 1977. Paleointensity studies of oceanic basalts from DSDP Leg 37 and NRM/ARM ratios of oceanic and recent lavas. *Phys. Earth Planet. Int.*, **13**, 332–338.

Carter-Stiglitz, B., Moskowitz, B., & Jackson, M., 2001. Unmixing magnetic assemblages and the magnetic behavior of bimodal mixtures. *J. Geophys. Res.*, **106**, 26397–26411.

Cisowski, C.S., 1980. Interacting vs. non-interacting single domain behavior in natural and sythetic samples. *Phys. Earth Planet. Inter.*, **26**, 56–62

Coe, R.S., 1969. Paleointensities of the Earth's magnetic field determined from Tertiary and Quaternary rocks. *J. Geophys. Res.*, **72**, 3247–3262.

Coe, R.S., 1979. The effect of shape anisotropy on TRM direction. *Geophys. J. R. astr.*

Soc., **56**, 369–383.

Cox, A., 1970. Latitude dependence of the angular dispersion of the geomagnetic field. *Geophys. J. R. Astron. Soc.*, **20**, 253–269.

Dalrymple, G.B., Lanphere, M.A., & Clague. D.A., 1980. Conventional and $^{40}Ar/^{39}Ar$ K-Ar ages of volcanic rocks from Ojin (Site 430), Nintoku (Site 432 and Suiko (Site 433) Seamounts and the chronology of volcanic propagation along the Hawaiian-Emperor chain. In *Init. Repts. DSDP, ed. E.D. Jackson and I. Koizumi, Washington (U.S. Govt. Printing Office)*, 659–676.

Davies, T.A., 1972. Koko seamount: a major guyot at the southern end of the Emperor Seamounts. *Mar. Geol.*, **13**, 311–321.

Day, R., Fuller, M., & Schmidt, V.A., 1977. Hysteresis properties of titanomagnetites: grain size and compositional dependence. *Phys. Earth Planet. Int.*, **13**, 206–267.

Dunlop, D.J., 1971. Magnetic properties of fine-particle hematite. *Ann. Géophys.*, **27**, 269–293.

Dunlop, D.J., & West, G.F., 1969. An experimental evaluation of single domain theories. *Rev. Geophys.*, **7**, 709–757.

Dunlop, D.J., & Hale, C.J., 1976.A determination of geomagnetic field intensity using submarine basalts drilled near the mid-Atlantic ridge. *J. Geophys. Res.*, **81**, 4166–4172.

Dunlop, D.J., & Bina, M-M., 1977. The coercive force spectrum of magnetite at high temperatires: Evidence for thermal activation below the blocking temperature, *Geophys.J. Roy. Astron. Soc.*, **51**, 121–147.

Dunlop, D.J., & Zinn, M.D., 1980. Archeomagnetism of a 19th century pottery kiln near Jordan, Ontario. *Can. J. Earth Sci.*, **17**, 1275–1285.

Dunlop, D.J., 1986. Coercive forces and coercivity spectra of submicron magnetites. *Earth Planet. Sci. Lett.*, **78**, 288–295.

Dunlop, D. J., Westcott-Lewis, M.F., & Bailey, M.E., 1990. Preisach diagrams and anhysteresis: Do they measure interactions? *Phys. Earth Planet. Inter.*, **65**, 62–77.

Dunlop, D.J., & Argyle, K.S., 1991. Separating multidomain and single-domain-like remanences in pseudo-single-domain magnetites (215–540 nm) by low-temperature demagnetization, *J. Geophys. Res.*, **96**, 2007–2017.

Dunlop, D. J., & Özdemir, Ö., 1997. *Rock Magnetism: Fundamentals and Frontiers*, 573 pp., Cambridge Univ. Press, Cambridge and New York.

Dunlop, D.J., 2002a. Theory and application of the Day plot (M_{rs}/M_s versus H_{cr}/H_c) 1. Theoretical curves and tests using titanomagnetite data. *J. Geophys. Res.*107 B3, 2056, doi: 10.1029/2001JB00486 EPM 4-1 to 4-22.,

Dunlop, D.J., 2002b. Theory and application of the Day plot (M_{rs}/M_s versus H_{cr}/H_c) 2. Application to data for rocks, sediments and soils. *J. Geophys. Res.* 107, B3, 2057, doi: 10.1029/2001JB00487 EPM 5-1 to 5-15.

El-Hilo, M., O'Grady, K., Mayo, P.I., Chantrell, R.W., Sanders, I.L., & Howards, J.K., 1992. The effects of different demagnetization processes on interaction effects in thin film media, *IEEE Trans. Magnetics*, **28**, 3282–3284.

Enkin, R.J., & Williams, W., 1994. Three-dimensional micromagnetic analysis of stability in fine magnetic grains. *J. Geophys. Res.*, **99**(B1), 611–618.

Evans, M. E., McElhinny, M.W., & Gifford, A.C., 1968. Single domain magnetite and high coercivities in a gabbroic intrusion, *Earth Planet. Sci. Lett.*, **4**, 142–146.

Evans, M. E., & Heller, F., 2003. Environmental magnetism: Principles and applications of enviromagnetics, Academic Press.

Feinberg, J. M., Scott, G.R, & Renne, P.R., 2003. Observations from magnetic force microscopy on crystallographically oriented magnetite inclusions in clinopyroxenes, *Eos Trans. AGU, 84(46)*, Fall Meet. Suppl., Abstract GP31B-0746.

Fernandez, A., Gibbons, M.R., Wall, M.A., & Cerjan, C.J., 1998. Magnetic domain structure and magnetization reversal in submicron-scale Co dots. *J. Magn. Magn. Mater.*, **190**, 71–80.

Fletcher, E.J., & O'Reilly, W., 1974. Contribution of Fe^{2+} ions to the magnetocrystalline anisotropy constant K_1 of $Fe_{3-x}Ti_xO_4$ ($0 < x < 0.1$). *J. Phys. C.: Solid State Phys.*, **7**, 171–178.

Goldstein, M.A., Strangway, D.W., & Larson, E.E., 1969. Paleomagnetism of a Miocene transition zone in southeastern Oregon, *Earth Planet. Sci. Lett.*, **7**, 231–239.

Grommé, S., Mankinen, E.A., Marshall, M., & Coe, R.S., 1979. Geomagnetic paleointensities by the Thellier method from submarine pillow basalts: effects of seafloor weathering. *J. Geophys. Res.*, **84**, 3553–3575.

Hargraves, R.B., & Young, W.M., 1968. Source of stable remanent magnetism in Lambertville diabase, *Am. J. Sci.*, **267**, 1161–1167.

Heider, F., & Williams, W., 1988. Note on temperature dependence of exchange constant in magnetite. *Geophys. Res. Lett.*, **15**, 184–187.

Hejda, P., & Zelinka, T., 1990. Modeling of hysteresis processes in magnetic rock samples using the Preisach diagram. *Phys. Earth Planet. Int.*, **63**, 32–40.

Henkel, O., 1964. Remanenzverhalten und Wechselwirkungen in hartmagnetischen Teilchenkollectiven, *Phys. Stat. Sol.*, **7**, 919–924.

Hunt, C.P., Moskowitz, B.M., & Banerjee, S.K., 1995. Magnetic properties of rocks and minerals. In *Rock physics and phase relations: a handbook of physical constants, ed. T.J. Ahrens, American Geophysical Union, Washington, DC*, 189–204.

Jackson, M., Worm, H.U., & Banerjee, S.K., 1990. Fourier-analysis of digital hysteresis data- rock magnetic applications, *Phys. Earth Planet. Int.*, **65**, 78–87.

Keller, R.A., Duncan, R.A., & Fisk, M.R., 1995. Geochemistry and $^{40}Ar/^{39}Ar$ geochronology of basalts from ODP Leg 145 (North Pacific Transect). In Rea, D.K., Basov, I.A., Scholl, D.W., and Allan, J.A. (Eds), *Proc. ODP, Sci. Results*, **145**, College Startion, TX, 334–344. Kirschvink, J.L, 1980. The least square line and plane and the analysis of paleomagnetic data. *Geophys. J. R. Astron. Soc.*, **62**, 699–718.

Kono, M., 1980a. Paleomagnetism of DSDP Leg 55 basalts and implications for the tectonics of the Pacific Plate. In *Init. Repts. DSDP, ed. E.D. Jackson and I. Koizumi, Washington (U.S. Govt. Printing Office)*, 737–752.

Kono, M., 1980b. Magnetic properties of DSDP Leg 55 basalts. In *Init. Repts. DSDP, ed. E.D. Jackson and I. Koizumi, Washington (U.S. Govt. Printing Office)*, 753–758.

Kono, M., 1980c. Geomagnetic paleointensity measurements on Leg 55 basalts. In *Init. Repts. DSDP, ed. E.D. Jackson and I. Koizumi, Washington (U.S. Govt. Printing Office)*, 723–736.

Landau, L.D., & Lifschitz, E.M., 1935. On the theory of the dispersion of magnetic permeability in ferromagnetic bodies (transl. from Russian), *Phys. Z. Sowjetunion*, **8**, 153-169.

Lees, J.A., 1997. Mineral magnetic properties of mixtures of environmental and synthetic materials: linear additivity and interaction effects. *Geophys. J. Int.*, **131**, 335–346.

Levi, S., & Merrill, R.T., 1978. Properties of single-domain, pseudo-single domain and multidomain magnetite. *J. Geophys. Res.*, **83**, 309–323.

Lowrie, W., & Fuller, M., 1971. On the alternating field demagnetisation characteristics of multidomain thermoremanent magnetisation in magnetite. *J. Geophys. Res.*, **76**, 6339–6349.

Mankinen, E.A., Larson, E.E., Grommé, C.S., Prévot, M., & Coe, R., 1987. The Steens Mountain (Oregon) geomagnetic polarity transition; 3, Its regional significance. *J. Geophys. Res.*, **92**, 8057–8076.

Matzka, J., Krása, D., Kunzmann, T., Schult, A., & Petersen, N., 2003. Magnetic state of 10-40 Ma old ocean basalts and its implications for natural remanent magnetization, *Earth Planet. Sci. Lett.*, **206**, 541–553.

McFadden, P.L., & Reid, A.B., 1982. Analysis of paleomagnetic inclination data. *Geophys. J. R. Astr. Soc.*, **69**, 307–319.

McFadden, P.L., Merrill, R.T., McElhinny, M.W., & Lee, S., 1991. Reversals of the Earth's magnetic field and temporal variations of the dynamo families. *J. Geophys. Res.*, **96**, 3923–3933.

Molnar, P., & Stock, J., 1987. Relative motions of hotspots in the Pacific, Atlantic and

Indian Oceans since Late Cretaceous time. *Nature*, **327**, 587–591.

Morgan, W.J., 1971. Convection plumes in the lower mantle, *Nature*, **230**, 42–43.

Morin, J., 1950. Magnetic susceptibility of αFe_2O_3 and Fe_2O_3 added titanium, *Phys. Rev*, **78**, 819–820.

Moskowitz, B.M., Frankel, R.B., Flanders, P.J., Blakemore, R.P., & Schwatrz, B.B., 1988. Magnetic properties of magnetotactic bacteria. *J. Magn Mag. Mag*, **73**, 273-288.

Moskowitz, B.M., Jackson, M., & Kissel, C., 1998. Low-temperature magnetic behavior of titanomagnetites. *Earth Planet. Sci. Lett.*, **157**, 141–149.

Murthy, G.S., Evans, M.E., & Gough D.I., 1971. Evidence of single-domain magnetite in the Michikamau anorthosite, *Can. J. Earth Sci.*, **8**, 361–370.

Muxworthy, A.R., & Williams, W., 1998. Micromagnetic models of pseudo-single domain grains of magnetite near the Verwey transition. *J. Geophys. Res*, **104**, 29203–29218.

Muxworthy, A.R., 2001. Effect of grain interactions on the frequency dependence of magnetic susceptibility. *Geophys. J. Int.*, **144**, 441–447.

Muxworthy, A.R., & Dunlop, D.J., 2002. First-order reversal curve (FORC) diagrams for pseudo-single-domain magnetites at high temperature, *Earth Planet. Sci. Lett.*, **203**, 369–382.

Muxworthy, A.R., Williams, W., Virdee, D., and Carvallo, C., 2003a. Micromagnetic modelling of magnetostatic interactions: hysteresis and FORC diagrams, First International Workshop on Magnetism, Hysteresis and the FORC Method, University of California, Davis, April 25-27, 2003.

Muxworthy, A.R., Williams, W., & Virdee, D., 2003b. The effect of magnetostatic interactions on the hysteresis parameters of single-domain and pseudo-single domain grains, *J. Geophys. Res.*, **108, B11**, 2517, doi:10.1029/2003JB002588

Muxworthy, A.R., King, J.G., Heslop, D., & Williams, W., 2003c. Unravelling magnetic mixtures using first-order reversal curve (FORC) diagrams: linear additivity and interaction effects, *Eos Trans. AGU*, **84**(46), Fall. Meet. Suppl., Abstract GP31B-0749.

Nagata, T., Arai, Y., & Momose, K., 1961. Secular variation of the geomagnetic total force during the last 5000 years. *J. Geophys. Res*, **68**, 5277–5281.

Néel, L., 1949. Théorie du traînage magnétique des ferromagnétique en grains fins avec applications aux terres cuites, *Ann. Géophys.*, **5**, 99–136.

Néel, L., 1954. Remarques sur la théorie des propriétés magnétiques des substances dures. *Appl. Sci. Res.*, {**B4**, 13–24.

Newell, A.J., & Merrill, R.T., 1999. Single-domain critical sizes for coercivity and remanence. *J. Geophys. Res.*, **104**, 617–628.

Newell, A.J., & Merrill, R.T., 2000. Size dependence of hysteresis properties of small pseudo-single-domain grains. *J. Geophys. Res.*, **105**, 19393–19403.

Norton, I.O., 1995. Plate motions in the North Pacific: the 43 Ma Nonevent, *Tectonics*, **14**, 1080–1084.

O'Reilly, W., 1984. Rock and Mineral Magnetism, Blackie, Glasgow and London, & Chapman and Hall, New York, 220 pp.

Özdemir, Ö., 1987. Inversion of titanomaghemites, *Phys. Earth Planet. Int.*, **57**, 184–196.

Özdemir, Ö., & O'Reilly, W., 1982. Magnetic hysteresis properties of synthetic monodomain titanomagnetites. *Earth Planet. Sci. Lett.*, **57**, 437–447.

Özdemir, Ö., & Banerjee, S.K., 1984. High temperature stability of maghemite. *Geophys. Res. Lett.*, **11**, 161–164.

Özdemir, Ö., 1990. High-temperature hysteresis and thermoremanence of single-domain maghemite, *Phys. Earth Planet. Inter.*, **65**, 125–136.

Özdemir, Ö., Dunlop, D.J., & Moskowitz, B.M., 1993. The effect of oxidation on the Verwey transition in magnetite, *Geophys. Res. Lett.*, **20**, 1671–1674.

Özdemir, Ö., Dunlop, D.J., & Moskowitz, B.M., 2002. Changes in remanence, coercivity and domain state at low temperature in magnetite. *Earth Planet. Sci. Lett.*, **194**, 343–358.

Pauthenet, R., & Bochirol, L., 1951. Aimantation spontanée des ferrites. *J. Phys. Rad*, **12**, 249–251.

Pike, C.R., & Fernandez, A., 1999. An investigation of magnetic reversal in submicron-scale Co dots using first order reversal curve diagrams. *J. App. Phys.*, **85**, 6668–6676.

Pike, C.P., Roberts, A.P., & Verosub, K.L., 1999. Characterizing interactions in fine magnetic particle systems using first order reversal curves. *J. App. Phys.*, **85**, 6660–6667.

Pike, C.P., Roberts, A.P., & Verosub, K.L., 2001a. FORC diagrams and thermal relaxation effects in magnetic particles. *Geophys. J. Int.*, **145**, 721–730.

Pike, C.P., Roberts, A.P., Dekkers, M.J., & Verosub, K.L., 2001b. An investigation of multi-domain hysteresis mechanisms using FORC diagrams. *Phys. Earth Planet. Int.*, **126**, 11-25.

Preisach, F., 1935. Über die magnetische Nachwirkung, *Z. Phys.*, **94**, 277–302.

Press, W.H., Teukolsky, S.A., Vetterling, W.T., & Flannery, B.P., 1994. *Numerical Recipes in C*, Cambridge University Press.

Proksch, R.B., & Moskowitz, B.M., 1994. Interactions between single domain particles,

J. Appl. Phys., **75**, 5894–5896.

Rave, W., Fabian, K., & Hubert, A., 1998. The magnetic states of small cubic magnetic particles with uniaxial anisotropy. *J. Magn. Magn. Mater.*, **190**, 332–348.

Renne, P. R., Scott, G.R., Glen, J.M.G, & Feinberg, J.M., 2002. Oriented inclusions of magnetite in clinopyroxene: Source of stable remanent magnetization in gabbros of the Messum Complex, Namibia, *Geochem. Geophys. Geosyst.*, **3 (12)**, 1079, doi:10.1029/2002GC000319.

Riisager, J., & Perrin, M., 2000. Paleomagnetism, paleointensity and geochronology of Miocene basalts and baked sediments from Velay Oriental, French Massif Central. *J. Geophys. Res.*, **105**, 883–896.

Riisager, P., Hall, S., Antretter, M., & Zhao, X., 2003. Paleomagnetic paleolatitude of Early Cretaceous Ontong Java Plateau basalts: implications for Pacific apparent and true polar wander, *Earth Planet. Sci. Lett.*, **208**, 235–252.

Roberts, A.P., Cui, Y.P. & Verosub, K.L., 1995. Wasp-waisted hysteresis loops: mineral magnetic characteristics and discrimination of components in mixed magnetic systems, *J. Geophys. Res.*, **100**, 17909–17924.

Roberts, A.P., Pike, C.P., & Verosub, K.L., 2000. First-order reversal curve diagrams: A new tool for characterizing the magnetic properties of natural samples. *J. Geophys. Res.*, **105**, 28461–28475.

Roth, A., Verosub, K., Pike, C.R., & Acton, G., 2003. FORC diagrams of synthetic magnetic minerals at ambient and high temperatures, Eos Trans AGU, 84(46), Fall Meet. Supppl., Abstract GP31B-0751.

Selkin, P.A., & Tauxe, L., 2000. Long-term variations in paleointensity. *Phil. Trans. R. Soc. Lond.*, **358**, 1065–1088.

Selkin, P.A., Gee, J.S., Tauxe, L., Meurer, W.P., & Newell, A.J., 2000. The effect of remanence anisotropy on paleointensity estimates: a case study form the Archean Stillwater Complex. *Earth Planet. Sci. Lett.*, **183**, 401–416.

Shaw, J., 1974. A new method for determining the magnitude of the paleomagnetic field. *Geophys. J. Roy. Astron. Soc.*, **39**, 133-141.

Smith, G.M., & Banerjee, S.K., 1986. Magnetic structure of the upper kilometer of the marine crust at Deep Sea Drilling Project Hole 504B, Eastern Pacific Ocean. *J. Geophys. Res*, **91**, 10337–10354.

Stacey, F.D., & Banerjee, S.K., 1974. *The Physical Principles of Rock Magnetism*, 195 pp. Elsevier, Amsterdam.

Steinberger, B., & O'Connell, R.J., 1998. Advection of plumes in mantle flow: Implications for hotspot motion, mantle viscosity and plume distribution. *Geophys. J. Int*, **132**, 412–434.

Stoner, E.C., & Wolfarth, E.P., 1948. A mechanism of magnetic hysteresis in heterogeneous alloys. *Phil. Trans. R. Soc. Lond*, **240**, 599–642.

Strangway, D.W., Larson, E.E., & Goldstein, M., 1968. A possible cause of high magnetic stability in volcanic rocks, *J. Geophys. Res.*, **73**, 3787–3795.

Tarduno, J.A., & Gee, J., 1995. Large-scale motion between Pacific and Atlantic hotspots. *Nature*, **378**, 477–480.

Tarduno, J.A., & Cottrell, R.D., 1997. Paleomagnetic evidence for motion of the Hawaiian hotspot. *Earth Planet. Sci. Lett.*, **153**, 171–180.

Tarduno, J.A., Duncan, R.A., Scholl, D.W., Bonaccorsi, R., Buysch, A., Carvallo, C., Cottrell, R.D., Einaudi, F., Frey, F.A., Haggas, S., Huang, S., Keller, R.A., Kerr, B.C., Lindblom, S., Neal, C.R., Regelous, M., Siesser, W., Steiberger, B., Stoll, J., Thompson, P.M.E., THordarson, T., Torii, M., Tremolada, F., and Gudding, J.A., 2002. Proc. ODP, Init. Repts., 197 [CD-ROM], available from: Ocean Drilling Program, Texas A&M University, College Station TX 77845-9547, USA.

Tarduno, J.A., Duncan, R.A., Scholl, D.W., Cottrell, R.D., Steinberger, B., Thordarson, T., Kerr, B.C., Neal, C.R., Frey, F.A., Torii, M., & Carvallo, C., 2003. The Emperor Seamounts: Southward motion of the Hawaiian hotspot plume in Earth's mantle, *Science*, **301**, 1064–1069.

Tauxe, L., Mullender, T.A.T., & Pick, T., 1996. Potbellies, wasp-waists, and superparamagnetism in magnetic hysteresis. *J. Geophys. Res.*, **101**, 571–593.

Thellier, E., & Thellier, O., 1959. Sur l'intensité du champ magnétique terrestre dans le passé historique et géologique. *Ann. Geophys.*, **15**, 285–376.

Thompson, R., & Oldfield, F., 1986. *Environmental Magnetism*, Allen and Unwin Publishers, London.

Thomson, L.C., 1993. A three-dimensional micromagnetic investigation of the magnetic properties and structures of magnetite, PhD thesis, Univ. of Edinburgh, Edinburgh, UK.

Thomson, L.C., Enkin, R.J., & Williams, W., 1994. Simulated annealing of three dimensional micromagnetic structures and simulated thermoremanent magnetization. *J. Geophys. Res.*, **99**, 603–606.

Virdee, D., 1999. The influence of magnetostatic interactions on the magnetic properties of magnetite, PhD thesis, University of Edinburgh, Edinburgh, UK.

Williams, W., 1995. A micromagnetic calculation of interaction effects in assemblies of single-domain hematite-magnetite mixtures, IUGG XXI General Assembly.

Williams, W. & Dunlop, D.J., 1989. Three-dimensional micromagnetic modelling of ferromagnetic domain structure.*Nature*, **337**, 634–637.

Williams, W., & Dunlop, D.J., 1995. Simulation of magnetic hysteresis in pseudo-single-

domain grains of magnetite. *J. Geophys. Res.*, **100**(B3), 3859–3871.

Williams, W., & Wright, T.M., 1997. High resolution micromagnetic models of fine grains of magnetite. *J. Geophys. Res.*, **99**(B1), 30537–30550.

Wilson, J.T., 1963. A possible origin of the Hawaiian Islands. *Can. J. Phys.*, **41**, 863–868.

Wohlfarth, E. P., 1958. Relations between different modes of acquisition of the remanent magnetization of ferromagnetic particles, *J. Appl. Phys.*, **29**, 595–596.

Wright, T.M., Williams, W., & Dunlop, D.J., 1997. An improved algorithm for micromagnetics. *J. Geophys. Res.*, **102**(B6), 12085–12094.

Xu, S., & Merrill, R.T., 1989. Microstress and microcoercivity in multidomain grains. *J. Geophys. Res.*, **94**(B6), 10627–10636.

York, D., 1969. Least-squares fitting of a straight line with correlated errors. *Earth Planet Sci. Lett.*, **5**, 320–324.

Yu, Y., Dunlop, D.J., Pavlish, L, & Cooper, M., 2000. Archeomagnetism of Ontario potsherds from the last 2000 years. *J. Geophys. Res.*, **105**, 19419–19433.

Yu, Y., Dunlop, D.J., & Özdemir, Ö., 2002. Partial anhysteretic remanent magnetization in magnetite. 1. Additivity, *J. Geophys. Res.*, **107 (B10)**, 2244, doi: 10.1029/2001JB001249.

Zelinka, T., Hejda, P. & Kropacek, V., 1987. The vibrating sample magnetometer and Preisach diagram. *Phys. Earth Planet. Inter.*, **46**, 241–246.